1-2022

An Analysis of Associations Between Polarimetric Supercell Signatures

Erik Green
University of Nebraska-Lincoln, erik.green@huskers.unl.edu

AN ANALYSIS OF ASSOCIATIONS BETWEEN POLARIMETRIC SUPERCELL SIGNATURES

By

Erik R. Green

A THESIS

Presented to the Faculty of

The Graduate College at the University of Nebraska

In Partial Fulfillment of Requirements

For the Degree of Master of Science

Major: Earth and Atmospheric Sciences

Under the Supervision of Professor Matthew S. Van Den Broeke

Lincoln, Nebraska

January, 2022

AN ANALYSIS OF ASSOCIATIONS BETWEEN POLARIMETRIC SUPERCELL SIGNATURES

Erik Green, M.S.

University of Nebraska, 2022

Advisor: Matthew Van Den Broeke

Supercell thunderstorms produce unique polarimetric radar signatures that are not often observed in unorganized deep convection. Repetitive signatures include deep and persistent differential reflectivity (Z_{DR}) columns and the Z_{DR} arc signature, which are both indicative of thermodynamic and microphysical processes intrinsic to supercells. Prior investigations of supercell polarimetric signatures, both those observed by operational and research radars, and those simulated numerically, reveal positive correlations between the Z_{DR} column depth and cross-sectional area and quantitative characteristics of the radar reflectivity field. This study expands upon prior work by incorporating a dataset of discrete, right moving supercells from across the continental United States, as observed by the operational, Weather Surveillance Radar 1988-Doppler (WSR-88D) network. Several quantitative metrics from Z_{DR} and Z_{HH} signatures are compared against characteristics of Z_{DR} columns, including the depth of the column, and the cross-sectional area of the column within ~1 km of the environmental freezing level. Sample statistics including median, mean, and maximum metric values were compared and tested using non-parametric similarity tests, including a Mann Whitney U-test and the two-sample Kolmogorov–Smirnov test. Cross-correlation coefficients were calculated between Z_{DR} column metrics and the remaining polarimetric signature metrics with increasing positive

and negative lag of up to 45 minutes, for both individual storm observation periods, and as whole tornadic and nontornadic samples. A bootstrapping method (i = 5000) was conducted on the observed data, where bootstrapped distributions of metric median, mean, and maximum values were obtained, and the tornadic – nontornadic difference in the 95th percentile median values were compared against the respective observed statistic value differences. Paired metric comparison datapoints were also bootstrapped over all offset values, and the cross-correlation coefficients were compared against the observed values. After completing the analysis, the results reveal: 1) Significant (95% confidence level) differences exist between most of the tornadic and nontornadic sample metrics including larger max Z_{HH} storm-core and mean Z_{DR} arc values and larger inferred hail areal extent among the nontornadic sample, and deeper and broader Z_{DR} columns within the tornadic sample; 2) Significant correlation values between metric comparisons from the tornadic sample involving Z_{DR} arc characteristics indicative of polarimetric associations unique to pretornadic and tornadic supercells; 3) Significant correlation values between Z_{DR} column metrics and inferred hail radar metrics supportive of prior observations indicative of cyclical processes in both tornadic and nontornadic supercells.

ACKNOWLEDGEMENTS

First and foremost, I would like to thank my advisor, Dr. Matthew Van Den Broeke for providing me with the opportunity to conduct this research and diversify my educational experience by attending a new and unique institution at the University of Nebraska. My time in Lincoln was very helpful in my development as a scientist, having learned from a new group of faculty members and student body. Dr. Van Den Broeke has been a wonderful advisor, and his methodology fit very well into my learning style and work ethic. I am so incredibly grateful to have met him, worked under his supervision, and learned from him, and future students will be fortunate to have him as a mentor and advisor.

I would like to thank both Dr. Clinton Rowe, and Dr. Adam Houston for serving on my committee and providing me with additional guidance for my research, classwork, and teaching abilities. This gratitude is not lost on the remainder of the Earth and Atmospheric Sciences faculty though, as each member brought a different perspective of the science into my line of sight.

Additionally, I would like to extend a big thanks to Ms. Sayli Pokal, a consultant from the Statistics Cross-disciplinary Collaboration and Consulting Lab at UNL, as her efforts in developing statistical testing methods were crucial to the completion of this research, and greatly appreciated.

Last, but certainly not least, I would like to thank my loving family, for their unwavering support in my educational endeavors and chosen career path.

TABLE OF CONTENTS

LIST OF TABLES

LIST OF FIGURES (updated – 11/5/21)

Chapter 1: Introduction

Supercells are associated with high-impact weather hazards including significant tornadoes (Doswell 2001), large and damaging hail (Thompson et al. 2003), and damaging winds and flooding rains (e.g., Doswell 1994; Smith et al. 2001). Due to the diversity of hazardous weather associated with these storms, numerous studies have investigated the unique aspects of supercell thermodynamics, dynamics, and microphysics. Thermodynamic studies include analyses of temperature and buoyancy characteristics of the rear-flank downdraft (RFD) (e.g., Markowski 2002, Markowski et al. 2002; Shabbott and Markowski 2006, Skinner et al. 2011, 2014). Several studies have investigated supercell dynamics (e.g., Klemp and Wilhelmson 1978; Rotunno and Klemp 1982, 1985; Davies-Jones 1984), including the role of vertical wind shear interacting with supercell updrafts to induce vertical perturbation pressure gradients and enhance the stretching of low-level vertical vorticity. The complexities of a supercell are also inclusive of microphysical interactions. Supercell microphysics have been modeled in numerous studies (e.g., Johnson et al. 1993; Jung et al. 2010; Youngsun et al. 2010; Morrison and Millbrandt 2011; Kumjian et al. 2014; and many others). In fact, the choice of microphysics scheme is crucial to realistic representation of storm structure and dynamics, as well as the inclusion (or exclusion) of hail and graupel species to hydrometeor budgets (Johnson et al. 1993; Lim et al. 2011). Spectral bin microphysics (SBM) schemes have been shown to properly simulate splitting supercell characteristics for a veering vertical wind profile (Khain and Lynn 2009), where from the work of Klemp and Wilhelmson (1978) and Cotton and Anthes (1989), in the northern hemisphere, a dominant, right-moving cyclonic supercell is favored. While the ability to

simulate supercell storm characteristics at much finer resolutions (e.g., grid point spacing < 3 km) has improved with greater knowledge and computing ability, successful microphysical parameterization still remains a challenge. However, the capability to infer storm microphysics from radar observations has become much more readily available.

Dual-polarized radar provides a significant improvement in the study of supercell microphysics over that of conventional radar. Dual-polarized, or polarimetric radars transmit and receive radiation with both horizontal and vertical polarizations, which provides information about target size and shape allowing for inferences to be made about hydrometeor phase and species. Several polarimetric variables can be determined from the information provided by the horizontally and vertically polarized beams including Z_{DR}, the ratio of radar reflectivity factors at horizontal and vertical polarizations (e.g., Seliga and Bringi 1976). Z_{DR} is useful for distinguishing between regions of hail and rain and is substantially enhanced (positive) for drop-size distributions of large, oblate drops. Operationally, it can be a good measure of the median size of raindrops in a volume (Kumjian and Ryzhkov 2008, hereafter KR08).

Polarimetric radar is not a new technology, and the study of supercells with it extends back a few decades (e.g., Conway and Zrnić 1993; Hubbert et al. 1998). Additionally, there has been an increase in the use of mobile polarimetric radar systems (e.g., Bluestein et al. 2007; Tanamachi et al. 2012; Pazmany et al. 2013; Snyder et al. 2013; French et al. 2015; Griffin et al. 2018; Wakimoto et al. 2015, 2018). Mobile radar exhibits obvious advantages over that of the operational WSR-88D, currently employed by the National Weather Service, including its maneuverability relative to the storm, flexibility of scanning strategies, and spatial and temporal resolution. However, there are

a very limited number of available mobile radars which are not always collecting data, unlike the operational WSR-88D. Thus, storm case sample sizes in observational studies are often limited to smaller and at times insufficient numbers. With the recent dual-polarization upgrade to the Next-Generation Radar Network, comprised of 160 high-resolution S-band WSR-88Ds across the United States and territories, the operational capability of diagnosing supercell microphysics was significantly improved.

The investigation of polarimetric radar signatures in supercells utilizing S-band radar observations has been the focus of numerous studies. This includes analyses of numerous polarimetric radar signatures unique to supercell thunderstorms (e.g., Loney et al. 2002; Ryzhkov et al. 2005; KR08; Romine et al. 2008; Homeyer and Kumjian 2015), characteristics of polarimetric signatures relative to tornadogenesis (Van Den Broeke et al. 2008), and the evolution of a cyclic low-level mesocyclone with a rapid, high-resolution scanning strategy (Kumjian et al. 2010). Additionally, Van Den Broeke (2016), hereafter VDB16, investigated relationships between supercell polarimetric radar signatures, and near-storm environmental parameters including vertical wind shear and instability.

Numerous studies exist on the individual polarimetric features intrinsic to supercells and their associated environmental dependencies; however, research on associations that may exist temporally and spatially between polarimetric radar metrics is limited and confined to more recent years. Picca et al. (2010), conducted correlation testing between the 1-dB Z_{DR} column volume (updraft proxy) and hail core intensity (defined as the ratio of the 60-dBZ volume to the 40-dBZ volume) in four different storm cases, revealing strong lag-correlation coefficient values (R ~ 0.80) after an average of

20-30 minutes of lag. Similarly, Kumjian et al. (2014) demonstrated that the evolution of Z_{DR} column depth is correlated to increases in radar reflectivity and hail mass at the ground after a lag-time of 10-15 minutes, but noted that in real storms, this delay is likely upwards of 20-30 min, with the underestimation attributable to the two-dimensional cloud model utilized.

Kuster et al. (2019) performed an analysis of Z_{DR} column depth and well-known severe storm signatures such as -20°C reflectivity cores and mid-level mesocyclones. It was determined that peaks in the temporal trend of Z_{DR} column depth provide greater lead times in advance of severe hail than has been demonstrated by peaks in -20°C reflectivity cores. Prior work has been limited by small sample sizes and numerical simulations, but the work done by Kuster et al. (2019) has a significant advantage with the utilization of rapid-update radar data with return intervals of ~2 minutes. The data in this study had full volume scan times of four to five minutes and the greater time between new base scans (e.g., the lowest elevation-angle scan) likely affected the temporal resolution of polarimetric signatures. This is important to consider because following the time-period of data within this study, new scanning strategies have been deployed on the WSR-88D. This includes the intra-volume scanning technique known as Supplemental Adaptive Intra-Volume Low-Level Scans, or SAILS (Chrisman 2013) which was later adapted into the Multiple Elevation Scan Option for SAILS, or MESO-SAILS (Chrisman 2014), allowing for up to three additional 0.5˚ elevation-angle scans within a full volume scan, increasing the frequency of low-level scans, and effectively increasing the temporal resolution of base-scan polarimetric supercell signatures.

Most recently, Van Den Broeke (2020), hereafter VDB20, conducted a preliminary comparison of polarimetric supercell signatures between pretornadic (25-30 minutes prior to initial tornadogenesis) and nontornadic storms. Results from this study demonstrated greater (smaller) polarimetrically inferred hail areal extent for nontornadic (pretornadic) storms and greater and less variable Z_{DR} column sizes within pretornadic storms.

This study aims to improve upon past work by incorporating a much larger dataset of discrete supercell storm cases as observed by the WSR-88D between 2012-2014, to quantify statistical relationships of well-known polarimetric radar signatures and to develop physical reasons for statistical relationships that are found. The goals of this study include:

1) Quantify the differences in the mean and maximum values of radar metrics in tornadic and nontornadic storms.
2) Quantify correlations between temporal and spatial variations in Z_{DR} column depth and Z_{DR} column cross-sectional areal extent and:
    i) Polarimetrically-inferred hail areal extent (HAE)
    ii) Maximum storm-core Z_{HH} value (mean value of 10 largest Z_{HH} values)
    iii) Z_{DR} arc area, mean arc width, and mean arc value
3) Develop a conceptual model of the physical associations of polarimetric supercell signatures.

Chapter 2 will provide background information on the radar variables utilized and explanations for the repetitive Z_{DR} signatures found in supercells that are the focus of this study. Chapter 3 will discuss the methodology for metric retrieval and the reasoning behind statistical testing methods. Chapter 4 includes an in-depth analysis of the results and hypothesizes physical relationships between the radar metrics. Chapter 5 is comprised of a brief summary, conclusions, and future work recommendations.

Chapter 2: Background

Prior to the polarimetric upgrade to the NEXRAD network, the WSR-88D measured three variables including radar reflectivity factor, radial velocity, and spectrum width. Currently, the WSR-88D offers four additional variables utilizing dual-polarization including differential reflectivity, co-polar correlation coefficient, differential phase shift, and specific differential phase, all of which provide information about the size, shape, and orientation of targets within the sample volume. The metrics utilized in this study rely on radar reflectivity and differential reflectivity, so the reader is referred to Doviak and Zrnić (1993) and Rinehart (2004) for an in-depth discussion of the single-polarization radar products. Additionally, the reader is referred to Kumjian (2013a,b,c) for descriptions of the polarimetric variables and their applications over a spectrum of meteorological phenomena.

2a. Reflectivity Z_{HH}

Reflectivity (Z_{HH}) is the component of radar energy that is transmitted and received in the horizontal polarization and represents scatter of a radar signal from both hydrometeors and non-meteorological targets. The logarithmic reflectivity Z_{HH} is defined as 10 times the base-10 logarithm of the linear reflectivity factor z_{hh}, where z_{hh} represents the horizontal energy that has been scattered back to the radar:

$$Z_{HH} = 10 * \log_{10} (z_{hh} / 1 \text{ mm}^6 \text{ m}^{-3}) \quad (2.1)$$

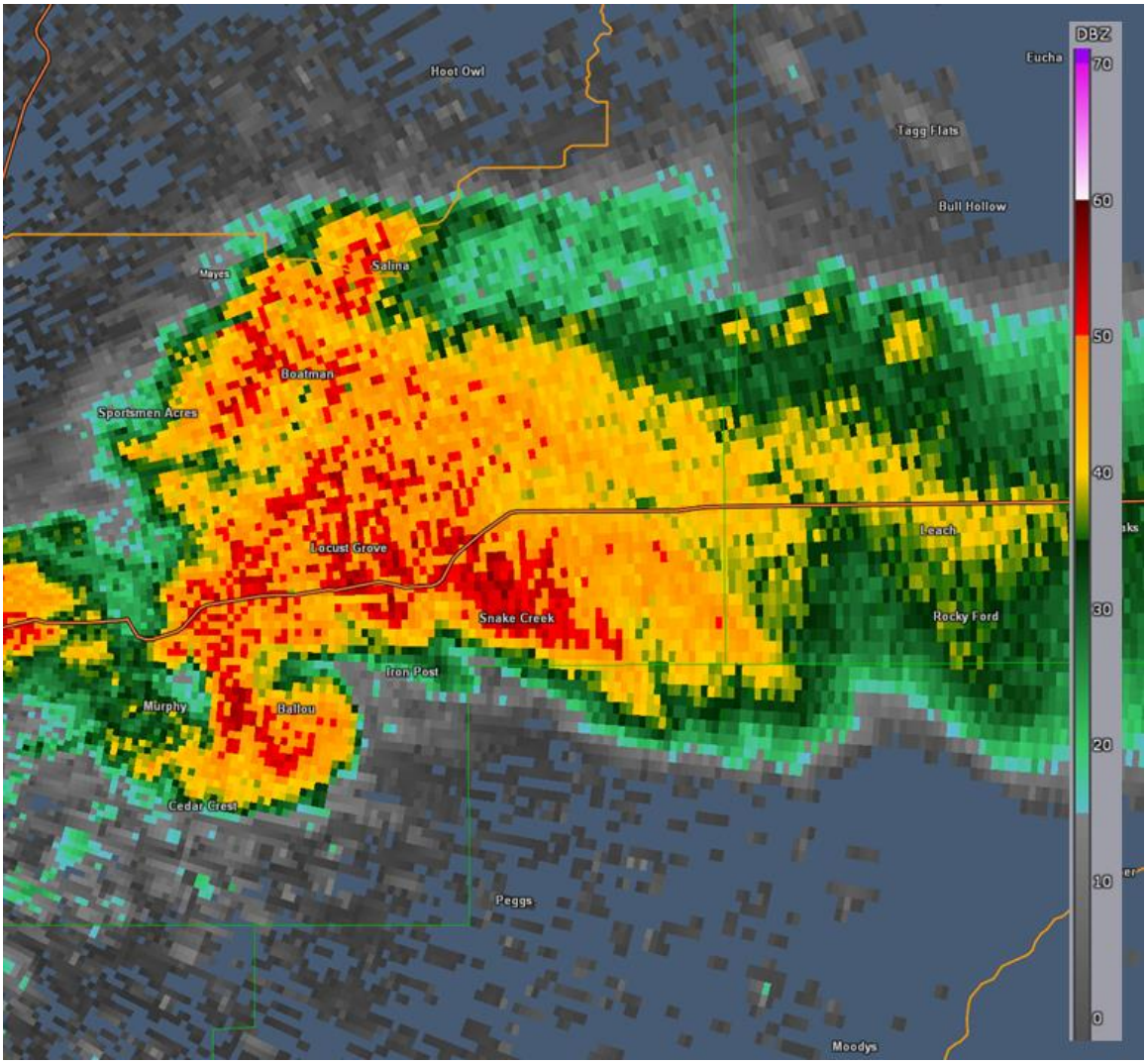

Figure 2.1: An example 0.5˚ elevation-angle scan of the Z_{HH} field, as observed from the KINX WSR-88D at 0032 UTC on 31 May 2013, displaying the classic radar-based supercell storm structure sought in this study.

The linear reflectivity factor can have values that span several orders of magnitude and overall is not useful in an operational setting. However, the logarithmic reflectivity factor acquires a more useful range of values for operational analysis. An example of the Z_{HH} field illustrating the classic supercell storm classification, is provided in Fig. 2.1. Classic supercells are characterized by their radar presentation including a well-defined hook echo reflectivity appendage, a weak-echo region and bounded weak-echo region, all of

which exhibit vertical and temporal continuity implying the presence of an updraft that is relatively precipitation free (Fig. 2.1, 2.2; Moller et al. 1994).

2b. Differential Reflectivity Z_{DR}

Differential reflectivity (Z_{DR}) is representative of how much horizontally polarized energy is scattered back to the radar relative to the scattering of vertically polarized energy. Thus, Z_{DR} is a measure of the reflectivity-weighted axis ratio of targets (Kumjian 2013a), and can provide a reasonable estimate of the oblateness or prolateness of hydrometeors within a sample volume. Mathematically, Z_{DR} is defined as 10 times the base-10 logarithm of the ratio of the horizontal and vertical polarizations of the linear reflectivity factor, and can be simplified as the difference of the horizontal and vertical polarizations of the logarithmic reflectivity:

$$Z_{DR} = Z_{HH} - Z_{VV} \tag{2.2}$$

Spherical (e.g. small raindrops) or spherically appearing targets (e.g., dry, tumbling hail) (Lesins and List 1986), will tend to scatter equal power in both polarizations, yielding Z_{DR} values ~ 0 dB. Thus, for more oblate targets (e.g., where the primary axis of the target is parallel to the horizontal polarization of the beam such as that of large oblate raindrops), more power is scattered in the horizontal polarization relative to the vertical, yielding a greater Z_{DR} value. As target size and number concentration increases, Z_{HH} will increase and generally so will Z_{DR}, suggesting a direct relationship between the two variables. However, exceptions to this have been noted in supercells (e.g. Kumjian and Ryzhkov 2009; 2012) where certain parts of a storm have observed high Z_{DR} values, indicative of large, oblate drops, collocated with moderate Z_{HH} values, suggesting lower

number concentrations of larger drops. This drop size distribution typically requires size sorting processes, which often manifests as unique Z_{DR} signatures found predominately in supercells, such as those discussed by KR08. A few examples of these polarimetric signatures include the Z_{DR} column and Z_{DR} arc. These are a primary focus of this study, and a discussion of the characteristics and formation of each signature will follow.

i. The Z_{DR} Column Signature

Z_{DR} columns are well documented in the literature (e.g., Illingworth et al. 1987; Wakimoto and Bringi 1988; Shupyatsky et al. 1990; Balakrishnan and Zrnić 1990; Vivekanandan et al. 1990; Bringi et al. 1991; Meischner et al. 1991; Herzegh and Jameson 1992; Conway and Zrnić 1993; Ryzhkov et al. 1994; Raghavan and Chandrasekar 1994; Brandes et al. 1995; KR08; Picca et al. 2010, 2015). Z_{DR} columns were first noted by Hall et al. (1984), where a column of high Z_{DR} extending 1.5 km above the ambient freezing level was observed, suggesting the presence of supercooled liquid water droplets lofted by an updraft.

Kumjian et al. (2014) used numerical modeling with a polarimetric radar operator and two-dimensional cloud model in order to determine the life-cycle and origins of column formation. Results revealed small raindrops from the primary updraft begin to fall out into weaker updrafts at the cloud edge, and are transported downward in compensating downdrafts. A portion of these raindrops are then recirculated into the main updraft at lower levels. If the positive vertical velocities are equivalent to the fall speeds of the drops, they become suspended and may experience rapid growth via collection of cloud droplets and smaller raindrops ascending from below. Large raindrops

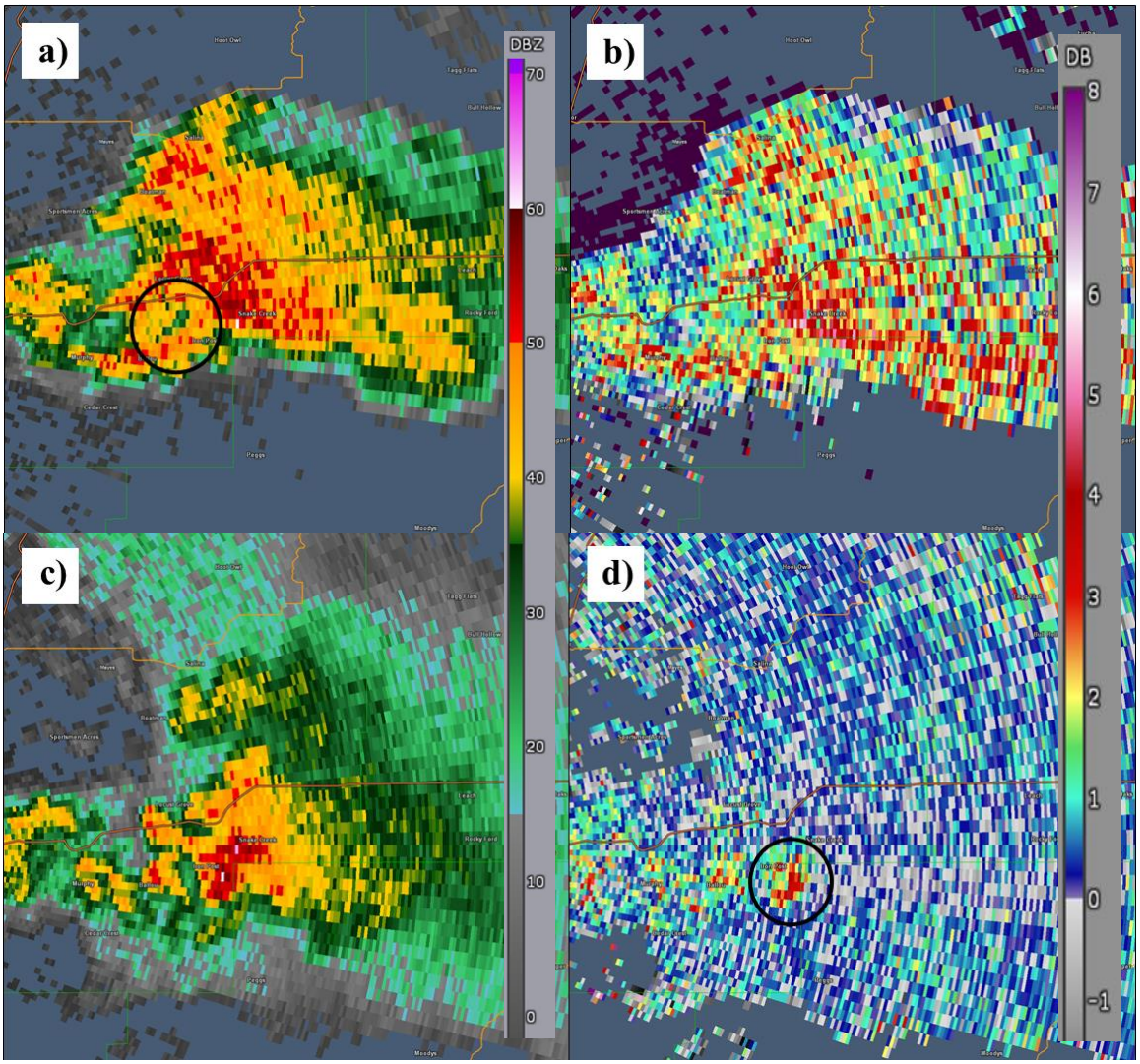

Figure 2.2: As in Fig. 2.1 for (a) the 2.4˚ elevation-angle of the Z_{HH} field, with a bounded weak echo region annotated with a black circle (~1.58 km above radar level at center of annotation), (b) as in (a), for the Z_{DR} field, (c) the 8.0˚ elevation-angle of the Z_{HH} field, (d) as in (c) for the Z_{DR} field, with the horizontal cross-sectional area of a Z_{DR} column annotated with a black circle (~5.66 km above radar level at center of annotation).

(> 4-5 mm) can quickly result from such conditions, eventually falling out against the updraft and causing an expansion in the Z_{DR} column downward from above. Smaller raindrops, particularly those in a stronger updraft are lofted farther upward, typically growing via coalescence, and forming the subfreezing layer of the column. Once these drops reach sufficiently cold temperatures, nucleation occurs and the drops begin to

freeze, however since this process is not instantaneous, the supercooled droplets may exist for a few minutes. If in-situ conditions are sufficient, complete freezing and continuous growth of these lofted particles often leads to the production of hail and/or graupel particles. Kumjian et al. (2014) created a general schematic for the particle mass distributions within Z_{DR} columns. At lower levels, the column is typically dominated by large raindrops below the ambient freezing level. Farther aloft in the column, freezing drops become more prevalent and, with increasing height, the particle distribution trends toward hailstones.

Z_{DR} columns within supercells (e.g., KR08; Kumjian et al. 2010) are generally narrow, usually 4-8 km wide, and may extend several kilometers above the environmental freezing level due to positive temperature perturbations associated with the updraft. A Z_{DR} column typically manifests as a localized, enhanced region of Z_{DR} (often > 3 dB), representative of large, oblate hydrometeors, consisting of large raindrops and water-coated hailstones. The column is consistently observed on the inflow side of a storm within or on the fringe of the updraft. From a radar imagery perspective, Z_{DR} columns are often within or on the periphery of a bounded weak echo region in the Z_{HH} field if the storm is strong enough. An example of this configuration can be seen in Fig. 2.2.

The correlation between Z_{DR} column characteristics and updraft tendencies is well documented. Tuttle et al. (1989) observed updraft speeds of 25–30 m s^{-1} associated with a mature column extending 3 km above the ambient freezing level, and later saw updraft weakening coinciding with the column depth decreasing. Brandes et al. (1995) and Bringi

et al. (1996, 1997) utilized polarimetric radar observations and aircraft transects, and observed very large raindrops (up to 8 mm in diameter) within Z_{DR} columns.

Z_{DR} columns have been identified as a suitable proxy for updraft *location* (e.g., Hall et al. 1984; Illingworth et al. 1987; Tuttle et al. 1989; Ryzhkov et al. 1994; Hubbert et al. 1998) and updraft *intensity* (e.g., Scharfenburg et al. 2005; KR08, Kumjian et al. 2012, 2014; Snyder 2013; Snyder et al. 2015). In a numerical study, Kumjian et al. (2014) found the maximum height of the 2-dB Z_{DR} contour to be positively correlated (R = 0.93) to the vertical velocity (w) at that corresponding altitude. It is important to consider that the maximum updraft speed (w_{max}) was located above the simulated Z_{DR} columns, so w_{max} and the height of the maximum 2-dB Z_{DR} contour were not as strongly correlated (R = 0.52). Snyder et al. (2015) also demonstrated numerically and through observations that the depth of Z_{DR} columns are positively correlated to the intensity of convective storm updrafts, and determined that changes in the depth of a Z_{DR} column tend to precede changes in w_{max}. Additionally, Z_{DR} columns that are taller (Scharfenberg et al. 2005) and broader (Kumjian et al. 2010) are often indicative of stronger updrafts, and tend to be more conducive for large hail growth (e.g., Nelson 1983; Picca and Ryzhkov 2012; Kumjian 2013b). Thus, metrics derived from the Z_{DR} column such as temporal trends of the depth of the column (distance between the altitude of the environmental 0˚C level and the maximum altitude of the 1-dB Z_{DR} column) and the horizontal cross-sectional area of a column (calculated within 1 km of the environmental 0˚C level), can offer insight into inferring updraft intensity and areal extent. The scanning strategy utilized by the operational WSR-88D captures useful horizontal cross sections through Z_{DR} columns, shown in Fig. 2.2, allowing operational forecasters to infer updraft

properties, e.g., the horizontal cross section of Z_{DR} columns appearing as curved or ring-like shapes can be indicative of cyclonic vertical vorticity within a convective updraft (KR08). Thus, real-time diagnostic tools for monitoring Z_{DR} column metric tendencies may help operational forecasters discern useful information on the potential severity of deep convective storms.

ii. The Z_{DR} Arc Signature

Ryzhkov et al. (2005) examined three tornadic supercells, which impacted Oklahoma City, OK and interrogated polarimetric radar data as a method of tornado detection. Anomalously large values of Z_{DR} (often exceeding 4 dB) were regularly observed on the periphery of high-reflectivity regions associated with the forward flank downdraft (FFD) and in the inflow region of the tornadic supercell thunderstorms. KR08 termed this region the Z_{DR} arc, once again noting an elongated region along the maximum gradient of the southern edge of the FFD (in right-moving supercells) with large Z_{DR} values as shown in Fig. 2.3. Unlike the Z_{DR} column, the arc signature is relatively shallow, typically no greater than 1-2 km deep.

Z_{DR} arcs (e.g., Ryzhkov et al. 2005; KR08; Kumjian and Ryzhkov 2009; 2012; Dawson et al. 2014; 2015) are a polarimetric manifestation of a lack of smaller raindrops, and a small number concentration of large, oblate raindrops, resulting in a Z_{DR} maximum not necessarily co-located with a Z_{HH} maximum. The arc signature forms as a result of hydrometeor size sorting, however the cause of this process is dependent upon the precipitation source movement (e.g. on-hodograph vs. off-hodograph). It is generally understood that precipitation particles (e.g., liquid drops, graupel, hail) originating from

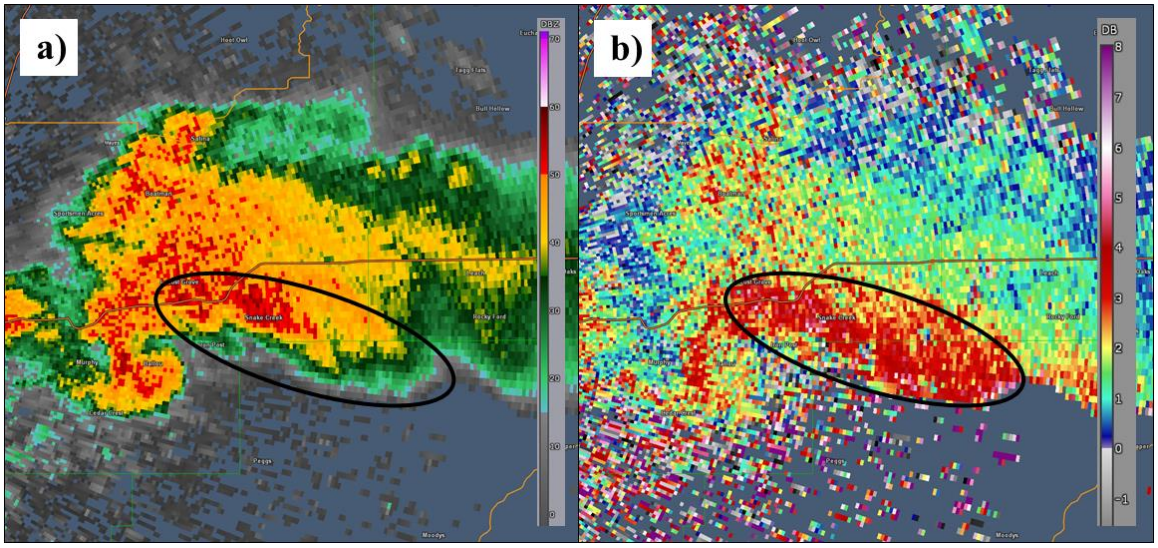

Figure 2.3: As in Fig. 2.1 for (a) the 0.5˚ elevation-angle of the Z_{HH} field, with the relative location of the Z_{DR} arc along the maximum Z_{HH} gradient of the inflow side of the forward flank downdraft annotated by a black oval, (b) the 0.5˚ elevation-angle of the Z_{DR} field, with the Z_{DR} arc signature annotated by a black oval. The center of the annotation is ~0.46 km above radar level.

enhanced Z_{HH} regions aloft fall towards the surface with varying trajectories depending on their size as a result of differential fall velocities (Browning 1965). For example, in an environment characterized by strong vertical wind shear (directional and/or speed shear), smaller particles tend to follow the background airflow well, while larger particles are not as likely to move with the background flow due to larger terminal velocities, even in the presence of a strong updraft, shown in Fig. 2.4.

Dawson et al. (2015) explored the role of vertical wind shear on hydrometeor size sorting and its relationship to signatures in the Z_{DR} field. Strong vertical wind shear was shown to be responsible for size sorting where the precipitation source motion lies on the hodograph (e.g., moving with the mean wind at the source level). However, in the case of an off-hodograph motion of the precipitation source (e.g., a right-moving supercell thunderstorm), vertical wind shear is not enough to support size sorting processes. The presence of a non-zero storm relative mean wind over the depth of a sorting layer was

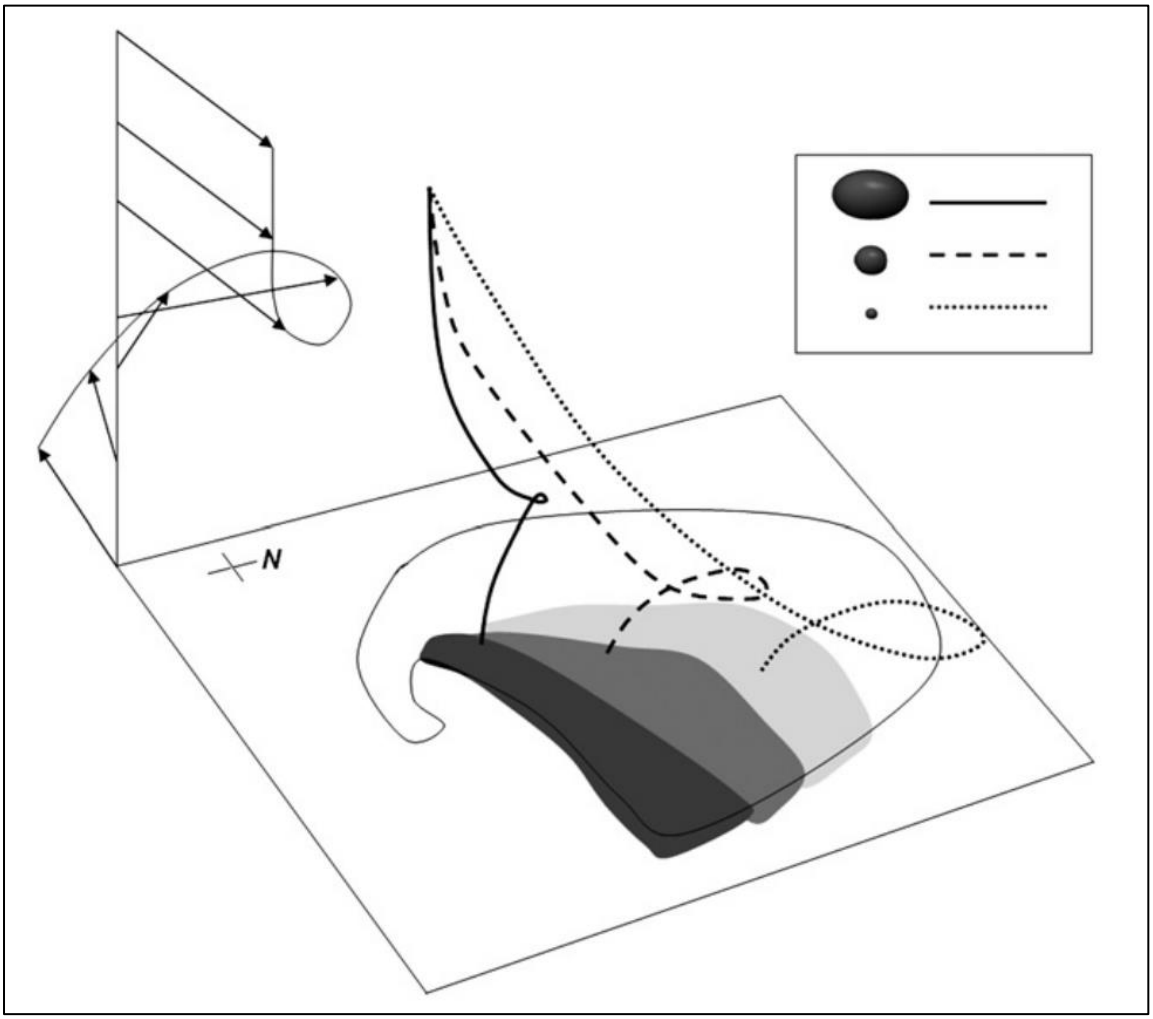

Figure 2.4: Fig. 2 from Kumjian and Ryzhkov (2009), depicting the trajectories of rain drops falling from a point source for a low-level veering wind profile in a supercell storm-relative frame, where if the line connecting the wind vectors was projected onto a two-dimensional plane, it would represent the hodograph. Trajectories are shown for large drops (solid black line), medium drops (dashed line), and small drops (dotted line). Shading within the supercell schematic FFD denotes typical Z_{DR} values found along the enhanced southern Z_{HH} gradient in a right-moving supercell, where the darkest shading represents the largest Z_{DR} values and the lightest shading represents smaller Z_{DR} values.

determined to be the kinematic driver for size sorting processes, regardless of the presence of vertical shear, and that a positive correlation exists between the magnitude of the storm-relative mean wind and hydrometeor size sorting. Physically, the Z_{DR} arc will develop in supercells perpendicular to the storm-relative mean wind vector given that it is non-zero, which acts to sort raindrops and melting hail. Thus, hydrometeor size sorting is

directly related to both the properties of a storm and the near-storm environment. The formation, presence, and dissipation of this polarimetric signature has been theorized to provide utility in diagnosing dynamical processes in supercells such as indicating tornado potential (Palmer et al. 2011; Crowe et al. 2012), and mesocyclogenesis in cyclic supercells (Kumjian et al. 2010).

Chapter 3: Methods

A dataset of polarimetric supercell storm cases which occurred between 2012-2014 was identified. Observation periods of individual storms range from 24 – 95 minutes, with an average time slightly less than five minutes required to complete a volume coverage pattern (VCP) scan. VCP scan times within this study exhibit variances due to the use of the Automated Volume Scan Evaluation and Termination algorithm, which allows for a VCP to be aborted before completing higher elevation angles, if certain criteria are met. These criteria depend upon both aerial coverage and the maximum reflectivity of any echoes in a volume (Chrisman 2009).

Storm cases were identified from across the continental U.S., with no specific geographic constraints. Most of the selected storms originated in the Great Plains and south-central U.S. (Fig. 3.1). Storms which were included were identified based on VDB16 methodology, e.g. discrete, cyclonically rotating (right-moving) classic supercells (Moller et al. 1994), which exhibit common supercell structures including a Z_{DR} arc and column, and consistent mid-level rotation. Additionally, to ensure high-quality resolution of storms and their unique polarimetric signatures, storms were included if their base-scan altitude was below 1 km for multiple consecutive volume scans, however base-scans where data was impeded by the cone of silence (e.g., the storm moved over the radar) were marked as missing. The minimum number of consecutive scans included was 6, and the most included was 21 volume scans.

The dataset consists of 52 cases which were divided into tornadic and nontornadic storms. Storms were deemed tornadic if there was an associated tornado local storm report per the National Center for Environmental Information (NCEI) storm report

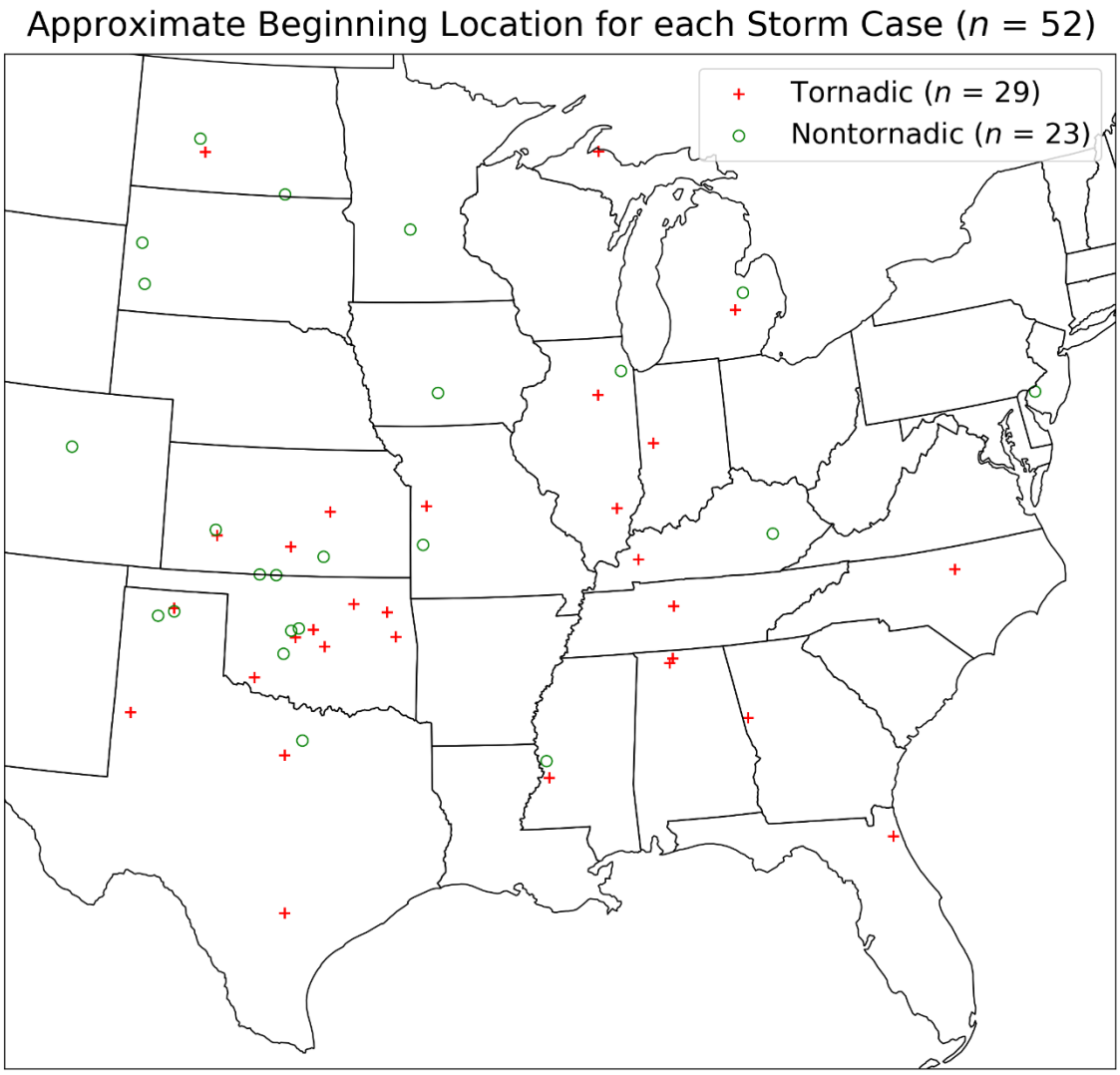

Figure 3.1: A map of the United States with the approximate starting location of the observation period for each storm in this study.

database, and the remainder were nontornadic storms. Within the dataset, 29 storms were tornadic and 23 were nontornadic. Several quantitative metrics have been obtained from level-II radar products including reflectivity and differential reflectivity. These metrics include maximum Z_{DR} column height above the ambient 0°C level, Z_{DR} column areal extent, Z_{DR} arc area, mean arc width and arc value, polarimetrically inferred hail areal extent (HAE), and maximum storm core reflectivity value. Radar data and the associated

metrics were analyzed and obtained as outlined in VDB16, and a brief description of each metric will follow.

3a. Radar Metrics

i. Z_{DR} Column Depth

The maximum vertical extent of a Z_{DR} column above the ambient freezing level, hereafter Z_{DR} column depth, has applications in quantifying updraft intensity (e.g., Scharfenburg et al. 2005; KR08; Kumjian et al. 2010, 2012, 2014; Snyder 2013; Snyder et al. 2015; VDB16). Z_{DR} column depth is defined as the maximum altitude of the 1-dB Z_{DR} contour associated with the column above the ambient 0°C level. This threshold was chosen based on consistency with the Z_{DR} column detection algorithm of Snyder et al. (2015). In order to determine the column depth, a representative model-derived proximity sounding was obtained from the Rapid Refresh (RAP) (VDB16). Soundings were spatially chosen to best represent the undisturbed regional supercell environment when possible (within 40 km of a storm, as in Thompson et al. 2003, 2007), and the closest model initialization was selected relative to the middle of the analysis period for each storm. If an analysis period lasted longer than one hour, values from two model-derived soundings (both based on model initialization) were averaged to obtain a representative average environment. Accuracy of sampled values tended to decrease for increasing storm-radar distance since beam centerlines of successively higher elevation angles spread out vertically with distance, and of the 633 total scans available, this metric could not be calculated for 31 scans (5%) due to an inability to clearly identify the top of the 1-dB Z_{DR} column.

ii. Z_{DR} Column Areal Extent

The Z_{DR} column areal extent as illustrated by VDB16 is defined as the 0.5-dB Z_{DR} contour at an altitude between approximately 0.7–1.3 km above the ambient 0°C level. This threshold was chosen so a greater number of data points could be included. Model-derived soundings, as described above, were used in quantifying the ambient 0°C altitude for the calculation of this metric. The 0.5-dB contour was chosen since it effectively reduced the influence of noise in the Z_{DR} field. Additionally, this metric was normalized by storm areal extent, defined as the area of the 35-dB*Z* storm echo, where the normalized value represents the proportion of the storm dominated by the updraft region aloft. The metric was quantified for each volume scan time step in the analysis period that had an elevation angle with data in the accepted altitude range, but otherwise were given a missing value. Sample data could not be determined for one storm of the 52 included, and of the 623 remaining scans, this metric was not calculated for 58 scans (9%) due to an inability to demarcate the area of the 0.5-dB column.

iii. Z_{DR} Arc Area and Mean Arc Width

The area of the Z_{DR} arc core was defined as the region enclosed by the 3.5-dB Z_{DR} contour (VDB16). The 3.5-dB contour was chosen since it represented the area of the arc dominated by large values, captured temporal changes well within each storm, and remains consistent with prior work (e.g., KR08; VDB16; VDB20). Due to the shallow nature of the arc signature, the arc was required to be fully located at a beam height < 1 km in altitude. This metric was also normalized by storm areal extent, where the normalized value represents the proportion of the storm dominated by the low-level Z_{DR}

arc area. Of the 633 total scans available, this metric could not be calculated for 14 scans (2%) due to the forward flank moving over the radar site, or because it moved farther away from the radar site.

The mean Z_{DR} arc width was determined by identifying the 2-dB Z_{DR} contour associated with the arc, and determining an average value of multiple transects of the arc approximately perpendicular to the maximum Z_{HH} gradient along the supercell forward flank. A single mean arc width was recorded for each volume scan at the lowest elevation angle, given that the altitude of the arc was entirely < 1 km. This altitude requirement was established so comparisons between storms are more representative. Of the 633 total scans available, this metric was not calculated for 13 scans (2%) because the 2-dB Z_{DR} arc was not completely < 1 km in altitude. Metrics pertaining to the Z_{DR} arc are of interest due to the potential for inferring low-level wind shear magnitude, e.g., Z_{DR} arc–storm core distance may be directly related to vertical wind shear magnitude in the storm inflow layer (Ganson and Kumjian 2015).

iv. Mean Z_{DR} Arc Value

As shown by VDB16, a mean value of Z_{DR} was calculated for all pixels > 0 dB within the Z_{DR} arc, where the arc region was defined by the 2-dB contour. Within the size sorting region, Z_{DR} values should be consistently large, so pixels with Z_{DR} < 0 dB should not be included. Metric values were obtained for every scan in an observation period where requirements were satisfied regarding the arc location relative to the radar described previously. Of the 633 total available scans, this metric was not calculated for 12 scans (2%) because the Z_{DR} arc was not well defined.

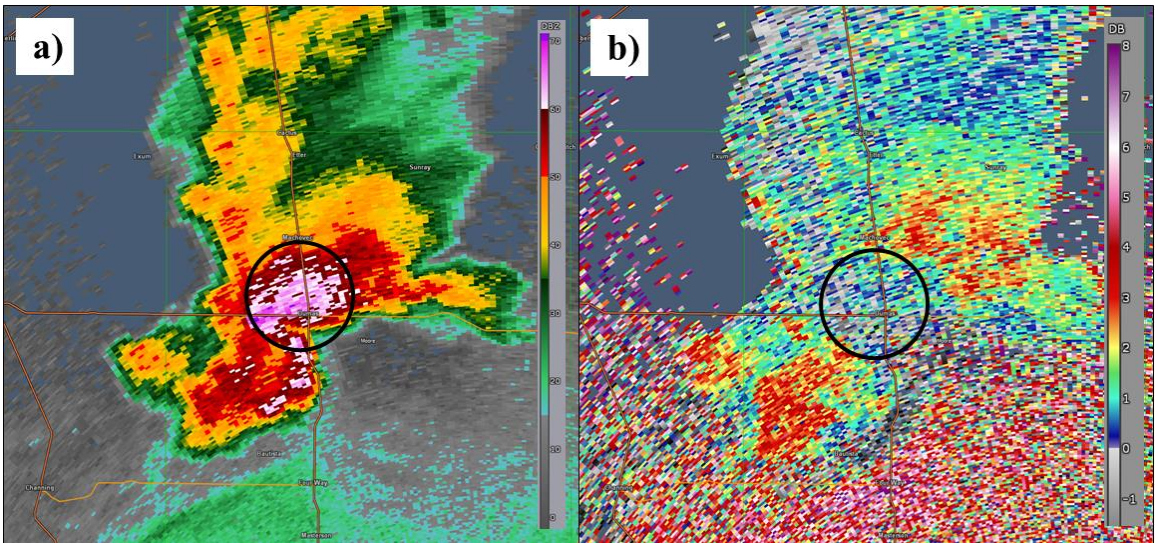

Figure 3.2: (a) The 0.5˚ elevation-angle scan of the Z_{HH} field, as observed from the KAMA WSR-88D at 0428 UTC 30 April 2012, exhibiting a nontornadic supercell with polarimetrically inferred hail annotated by the black circle. (b) The 0.5˚ elevation-angle scan of the Z_{DR} field with depressed Z_{DR} values collocated with enhanced Z_{HH} values, indicating potential hail fallout in the low-levels. The center of the annotation is ~1.04 km above radar level.

v. Polarimetrically Inferred Hail Areal Extent

Supercell storms often contain regions of hailfall, which may be determinable by analysis of both Z_{HH} and Z_{DR}. The signature is generally characterized by high Z_{HH} and near-zero Z_{DR} values (e.g., Balakrishnan and Zrnić 1990; KR08; Fig. 3.2), with regions of hail often most pronounced downshear from the mesocyclone. The low-level hail extent metric, as illustrated by VDB16, was polarimetrically inferred by calculating the area of the storm core associated with collocated high Z_{HH} (> 55 dBZ) and depressed Z_{DR} values (0-1 dB) (Fig. 3.2). Data at base-scan elevation were required to be < 1 km in altitude to avoid sampling mid-level hail cores, and to yield more comparable observations between storms. Additionally, this metric was normalized by storm areal extent, where the normalized value represents the proportion of the storm dominated by polarimetrically inferred hail. Of the 633 total scans available, this metric was not calculated for 7 scans (1%) due to the fact that beam altitude in the inferred hail region was > 1 km.

vi. Maximum Storm Core Reflectivity Value

While a simple metric, the maximum Z_{HH} value may provide information on the intensity of precipitation, including hail, within the storm core. Within intense convective storms, raindrop sizes are typically larger and can lead to an enhancement of 1-2 dB in Z_{HH}, and hail can contribute up to a 10 dB enhancement in Z_{HH} (Austin 1987). As shown in VDB20, the average of the 10 largest Z_{HH} values within the storm core were recorded if the altitude was < 1 km. It is noted that this variable may be prone to error due to noise and uncertainty in what scatterers contribute to the ten maximum values, however for tornadic storms, values from tornado debris signature bins were not included in the calculation. Of the 633 total scans available, this metric was not calculated for 12 scans (2%) because the radar beam was > 1 km in altitude.

3b. Methods

The 52 storms chosen for this study were divided into tornadic and nontornadic populations. The total distributions of each metric (both tornadic and nontornadic for every volume scan available) were tested for normality utilizing a Shapiro-Wilk test (Shapiro and Wilk 1965), with a majority of the distributions found to be non-Gaussian in shape at the 95% confidence level. An exception is noted for the mean Z_{DR} arc pixel value within nontornadic storms, which failed to reject the null hypothesis ($p > 0.05$). Due to an overwhelming majority of distributions being non-Gaussian, non-parametric tests were chosen in order to compare similarity of distributions, including the two-sample independent Mann Whitney U-test (MWU) (Rosner and Grove 1999) and the two-sample Kolmogorov-Smirnov (KS) test (Goodman 1954). The MWU and KS tests

were chosen for their non-parametric advantages, and were both used to ensure a thorough comparison between samples. The MWU test compares the mean ranks of two groups and is sensitive to differences in their median values, whereas the KS test is a comparison of the cumulative distribution functions of two groups and is sensitive to the shape and spread of sample distributions as well as their median values and may provide more information than employing only an MWU test.

Sample statistics including storm-mean, -median, and -maximum values were determined for each metric. The sample statistics were then separated into tornadic and nontornadic distributions, and both MWU and KS tests were conducted to determine if statistically significant differences existed between the two distributions for each sample statistic of the metrics. The median value for each sample statistic distribution was determined, and a difference value (tornadic-nontornadic, hereafter T-NT) was calculated. Additionally, a bootstrapping method was applied where all available sample scans for each metric (separated between tornadic and nontornadic storms) were sampled with replacement (i = 5000), following Kuster et al. (2019). Non-parametric distributions of sample statistics including mean, median, and maximum were created, and the median values of the 95th percentile range of the distributions were determined. T-NT differences in the bootstrapped distribution median values were calculated for comparison against the observed sample statistic T-NT median difference values.

Pearson cross-correlation values were calculated using the Z_{DR} column depth, Z_{DR} column areal extent, and the normalized Z_{DR} column areal extent (e.g., the independent variables) and the remaining radar metrics (e.g., the dependent variables). For the purposes of this study, a lag of up to nine volume scans (~ 45 minutes) was applied to the

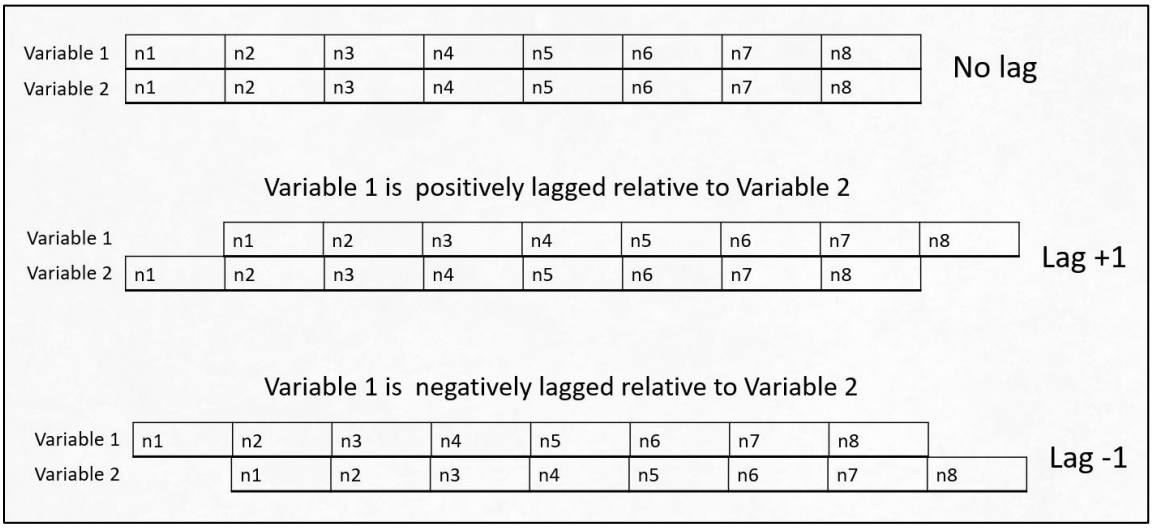

Figure 3.3: A schematic demonstrating how lag was applied to two given metrics being compared, for both a positive lag and negative lag.

metric comparisons in both directions of the zero offset, e.g., Fig. 3.3. Lag was introduced to further test the results of prior studies (e.g., Picca et al. 2010; Kumjian et al. 2014; Kuster et al. 2019) which demonstrated a physical relationship between updraft tendencies and precipitation fallout and intensity at a temporal offset of 15-30 minutes. In order to ensure a sufficient number of scans were included in each cross-correlation test, a minimum of six volume scans were required to be remaining after the metrics were lagged for each successive lag interval (Fig. 3.3). Correlation values were calculated for each metric comparison within each storm, and for each metric comparison in both tornadic and nontornadic samples (e.g., a cross-correlation coefficient was calculated for the Z_{DR} column depth vs. Z_{DR} arc area metric comparison using all available sample scans from tornadic storms at any given lag). However, due to the variation in the length of observation periods, the number of total sample scans included in the cross-correlation calculation decreased for each successive lag interval. Among the storm-based

correlation testing, a small number of storms had observation periods long enough to determine correlation values over the full amount of lag applied. For metric comparisons using the Z_{DR} column depth as the updraft proxy, a total of 14 storms (9 tornadic and 5 nontornadic) had an observation period long enough. Similarly, for comparisons using the Z_{DR} column area and the normalized column area as the updraft proxy, 13 storms (8 tornadic and 4 nontornadic) had observation periods that were long enough. From these storms, a median correlogram was created for both tornadic and nontornadic samples, and the maximum correlation value (*in magnitude*) was determined along with the corresponding lag interval. For the total sample correlation testing, the maximum correlation value (*in magnitude*) was also determined, along with the corresponding lag interval and *p*-value.

Additionally, a bootstrapping method was applied to the total sample cross-correlation testing, where the paired metric values in a comparison (e.g., for all tornadic samples, Z_{DR} column depth vs. mean Z_{DR} arc width at a given lag interval) were sampled with replacement (i = 5000) and cross-correlation values were calculated, resulting in a non-parametric distribution of cross-correlation values. This process was repeated for all comparisons discussed above over all consecutive offsets. The mean and median values of the bootstrapped distributions of cross-correlations were calculated and compared against the observed data. The 90th percentile of the distributions were also determined to demonstrate the "most reasonable" high magnitude cross-correlation coefficient possible. The 90th percentile was chosen to remain consistent with methods utilized in probabilistic guidance products disseminated by national forecast centers including the National Hurricane Center (National Hurricane Center 2020) and the Weather Prediction Center

(Burke et al. 2017). It is noted that some distributions of bootstrapped cross-correlation values were either completely less than zero, or had a median value close to zero, resulting in nearly equivalent 10^{th} and 90^{th} percentile values. In order to account for these scenarios, the 10^{th} percentile value was factored into the comparison and was chosen over the 90^{th} percentile if it was larger in magnitude, as this represents the legitimate most likely extreme value within the distribution.

Chapter 4: Results and Discussion

4a. Typical Values of Radar Signature Metrics

The first step of the analysis involved determining the typical range of values for each metric, whether tornadic or nontornadic. Certain metrics exhibited a large range of values, so sample statistics including median and mean were calculated within the 10^{th} – 90^{th} percentiles of total available sample scans for each metric. In doing so, a more reasonable range of metric values and sample statistics were created for interpretation and analysis. The data included are limited to radar scans of semi-discrete, right-moving (cyclonic) supercells from varying regions across the U.S. over a broad range of months and seasons (February – December). However, a majority (38 of 52 storms) were sampled during the climatological peak (March – May) in warm season supercell activity in the central and southern Great Plains (Brooks et al. 2003). It should be noted that a variable number of scans exist for each metric due to a lack of quality data for subjective analysis in varying storms.

The 35-dB*Z* storm area (Fig. 4.1) exhibited a broad range of values, with a 10^{th} – 90^{th} percentile range between 221.8 km^2 and 1264.7 km^2. The broad range of values from this metric demonstrates that there is not a textbook definition on the size of a supercell as they can be quite large (e.g., sample scans > 1000 km^2), or more moderately sized with ~ 50% of sample scans between 250 – 750 km^2, and median and mean values of 529.6 km^2 and 588.45 km^2, respectively. For inferred HAE (Fig. 4.1), the 10^{th} – 90^{th} percentile ranged from 3.53 km^2 to 63.62 km^2, with median and mean values of 21.74 km^2 and 25.83 km^2, respectively. Normalized inferred HAE (Fig. 4.1) had a 10^{th} – 90^{th} percentile range between 0.008 and 0.116, with median and mean values of

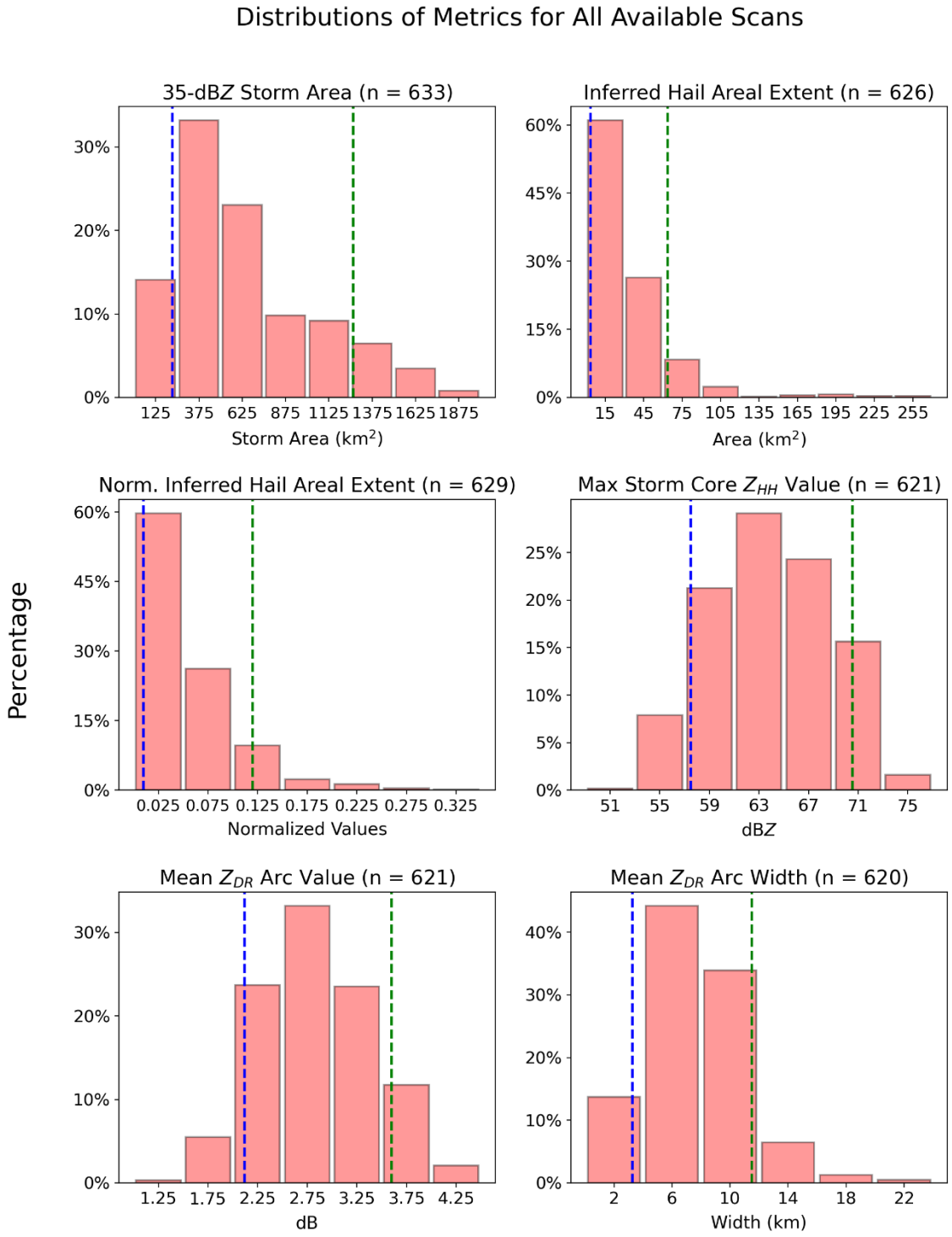

Figure 4.1: The distributions of all available sample scans for 35-dBZ storm area (top left), inferred hail areal extent (top right), normalized inferred hail areal extent (middle left), maximum storm core Z_{HH} value (middle right), mean Z_{DR} arc value (bottom left), and mean Z_{DR} arc width (bottom right). The 10th (blue dashed line) and 90th percentiles (green dashed line) are annotated, and bin midpoints are plotted on the x-axis.

0.037 and 0.045, respectively, indicating that for most sample scans, typically only 4 – 5% of the storm area consisted of inferred HAE. The 10th percentile of maximum storm core Z_{HH} values (Fig. 4.1) was 57.48 dB*Z* and the 90th percentile was 70.53 dB*Z*, with mean and median values of 63.87 dB*Z* and 63.83 dB*Z*, respectively.

The mean Z_{DR} arc value (Fig. 4.1) 10th – 90th percentile range fell between 2.12 dB and 3.6 dB, with a median value of 2.74 dB and mean value of 2.81 dB. The mean Z_{DR} arc width metric (Fig. 4.1) had a 10th – 90th percentile range between 3.28 km and 11.5 km, with median and mean values that were equivalent at 7.38 km. The Z_{DR} arc area (Fig. 4.2) metric exhibited a wide range where the 10th – 90th percentile fell between 2.74 km^2 and 163.03 km^2, and had median and mean values of 70.64 and 70.59 km^2. The normalized Z_{DR} arc area (Fig. 4.2) exhibited a 10th – 90th percentile range between 0.007 and 0.312, with median and mean values of 0.112 and 0.1205, respectively. The sample statistics for the normalized Z_{DR} arc area indicate that the arc area or arc core tended to occupy just over 10% of the storm area in most sample scans. It is noted that for this metric, bin differences were not all equal, with metric values > 0.50 grouped into two bins of unequal sizes (0.50 – 1.0 and 1.0 – 2.2). This was done in order to group anomalous normalized values > 1.0 from a storm where overall reflectivity values were low resulting in a low 35- dB*Z* storm area while the Z_{DR} arc remained well pronounced.

Z_{DR} column areal extent (Fig. 4.2) had a large range of values with a 10th – 90th percentile range between 9.26 km^2 to 97.95 km^2, a median value of 38.48 km^2, and a mean value of 42.25 km^2. The normalized Z_{DR} column areal extent (Fig. 4.2) also exhibited a large range of observed values where the 10th – 90th percentile range fell between 0.019 to 0.203, had a median value of 0.077, and a mean value of 0.083. The

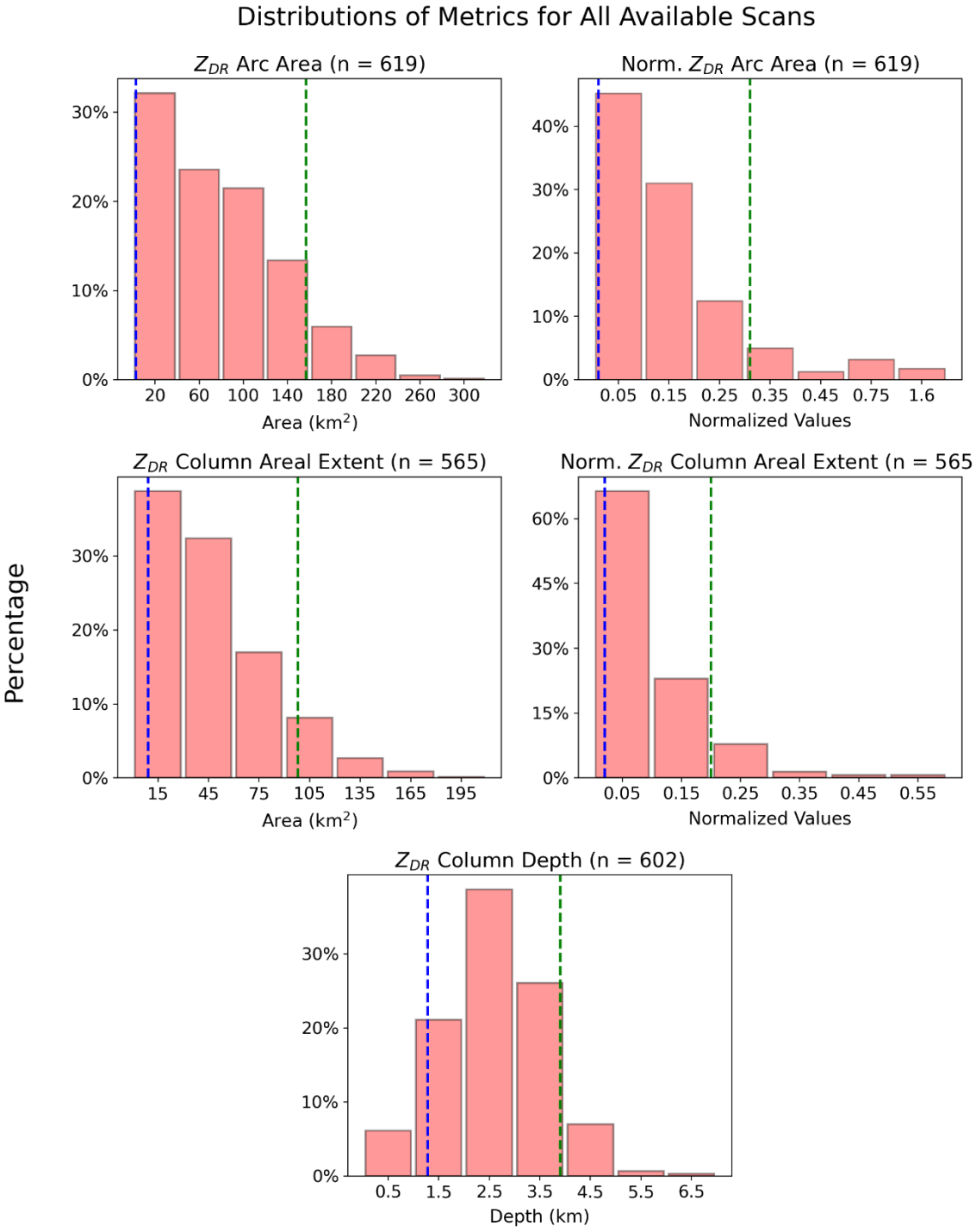

Figure 4.2: As in Fig. 4.1, for Z_{DR} arc area (top left), normalized Z_{DR} arc area (top right), Z_{DR} column areal extent (middle left), normalized Z_{DR} column areal extent (middle right), and Z_{DR} column depth (bottom). Note that for normalized Z_{DR} arc area, all bins were not uniform in size due to a few storms with normalized values greater than one.

sample statistics for the normalized Z_{DR} column cross sectional area indicate that the polarimetrically inferred updraft region aloft occupied < 10% of the storm area in most sample scans. Lastly, the Z_{DR} column depth (Fig. 4.2) exhibited a 10^{th} – 90^{th} percentile range of values from 1.28 km to 3.9 km, with a median value of 2.57 km, and mean value of 2.59 km. This analysis demonstrates that certain metrics tend to be more variable and may not be best represented by a typical value or sample statistic, e.g., storm area, Z_{DR} arc area, and Z_{DR} column area.

4b. Tornadic vs. Nontornadic Samples

The next question is whether tornadic and nontornadic supercells can be differentiated based on the quantitative radar metrics, similar to work done by VDB20 where the possibility was demonstrated for select radar metrics. The first test involved comparing the distributions of total sample scans for each metric among tornadic and nontornadic samples by utilizing both KS and MWU tests to identify statistically significant differences. The non-parametric tests were chosen due to all but one metric distribution differing from a Gaussian shape at the 95% confidence level, per Shapiro-Wilk test results described above. KS and MWU testing on samples of total scans of tornadic and nontornadic radar metrics yielded statistically significant results at the 95% confidence level ($p < 0.05$) for several sample distribution comparisons except for mean Z_{DR} arc width and storm areal extent. These results are constrained by unequal sample sizes for each metric, and unequal sample sizes for both categories of storms. However, it is a promising signal as it displays the possibility of differentiating tornadic and nontornadic storms based on certain polarimetric signatures.

Qualitative and quantitative characteristics can be inferred from the total sample scan comparisons. Statistically significant differences were not found between tornadic and nontornadic sample scans per the KS and MWU tests for the storm area metric (Fig. 4.3). This implies that among the samples collected, reflectivity echo size differences between supercells are likely not a suitable factor for differentiating tornadic potential, and the divided samples are consistent with the prior notion that supercells can take on a wide range of sizes. For the inferred HAE metric (Fig. 4.3), statistically significant results were found based on the *p*-values of both the KS and MWU tests. A similar variability of inferred HAE was observed between nontornadic and tornadic samples with a few outlier sample scans in excess of 100 km^2 among the nontornadic samples. These results are weakly reflected in the mean values, e.g., 24.24 km^2 and 41.37 km^2, however the median values exhibit a weaker difference, e.g., 17.63 km^2 and 22.16 km^2 (both pairs of sample statistics are tornadic and nontornadic respectively). It is worth noting that ~ 70% of sample scans from tornadic storms exhibited an inferred HAE between 0 – 30 km^2 whereas only ~ 45% of nontornadic samples fell into the same bin. This results of the normalized inferred HAE metric are similar to the raw metric comparison, with ~ 70% of tornadic sample scans falling within the 0 – 5% bin, indicating that generally the inferred HAE occupied < 5% of the total storm area for a majority of tornadic samples.

The max storm core Z_{HH} value comparison (Fig. 4.3) exhibits statistically significant results based on the KS and MWU test *p*-values, and physical separation can be seen between the two sample distributions. For both categories of storms, sample mean values were 62.4 dB*Z* and 66.15 dB*Z* (tornadic and nontornadic respectively) and

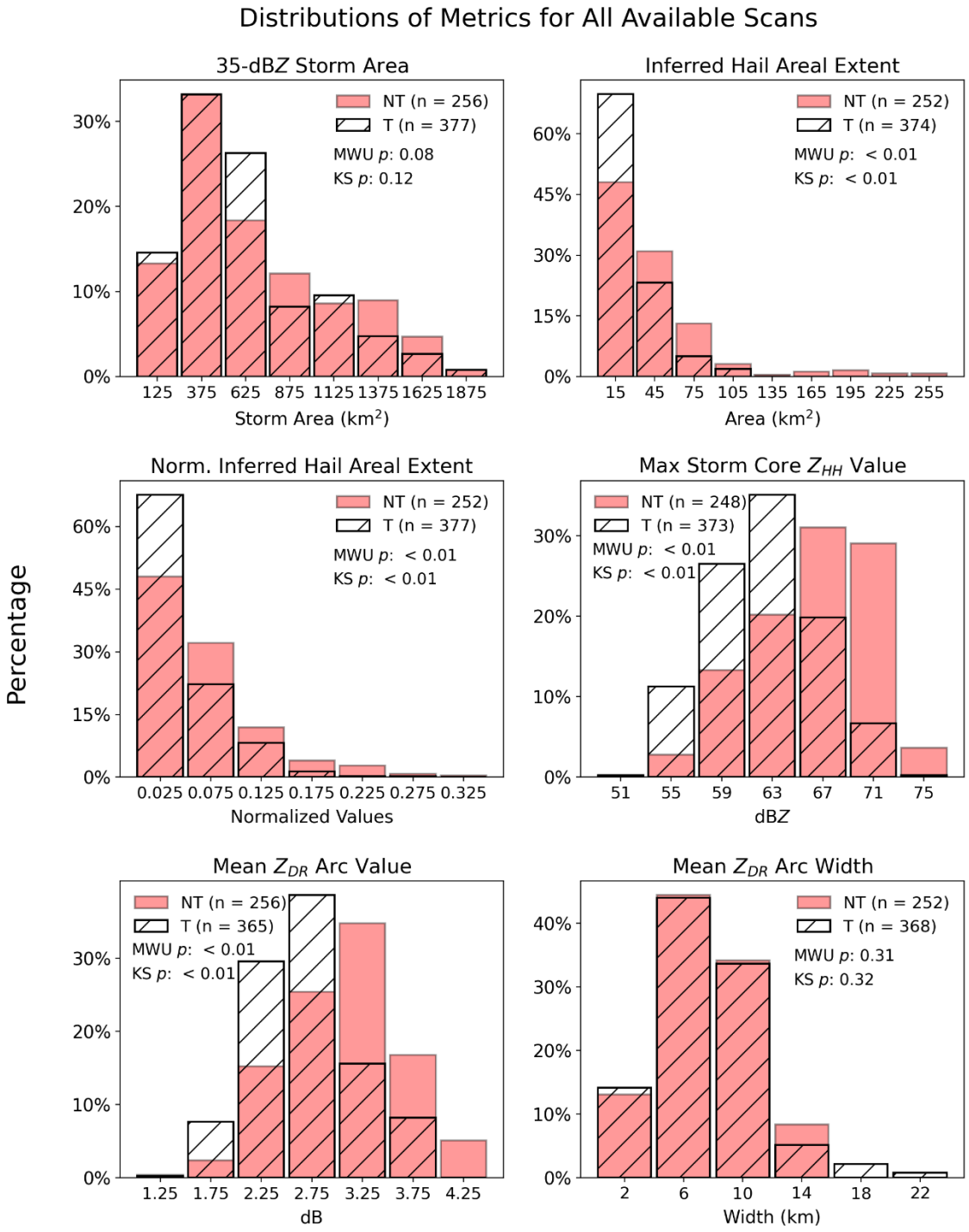

Figure 4.3: Tornadic (hashed bars) and nontornadic (red bars) distributions of all available sample scans for 35-dBZ storm area (top left), inferred hail areal extent (top right), normalized inferred hail areal extent (middle left), maximum storm core Z_{HH} value (middle right), mean Z_{DR} arc value (bottom left), and mean Z_{DR} arc width (bottom right). The *p*-values from the KS and MWU tests are annotated, and bin midpoints are plotted on the x-axis.

the medians were 62.56 and 66.62 dBZ. However, the scale of this metric must be considered when evaluating the meaning of the statistical results. Differences in the sample statistics between the tornadic and nontornadic categories were ~ 4 dBZ with nontornadic storms tending to have a greater max core Z_{HH} value. In terms of operational value, the magnitude of separation between the samples would not prove useful to a warning forecaster for differentiating between supercells.

A similar conclusion can be made for the mean Z_{DR} arc value comparison (Fig. 4.3). Sample statistics of these distributions include mean values of 2.67 dB and 3.05 dB (tornadic and nontornadic respectively) and median values of 2.61 dB and 3.08 dB, yielding a typical difference of ~ 0.5 dB between the samples. Microphysically this does imply differences such as the median hydrometeor diameter within the arc region, e.g., generally nontornadic sample scans exhibited a larger mean Z_{DR} arc value within the arc region. However, similar to the max Z_{HH} value metric, the magnitude of the difference in sample statistics is not useful in an operational setting despite statistically significant results.

The mean Z_{DR} arc width metric comparison (Fig. 4.3) did not yield statistically significant results and this can be inferred qualitatively based on the physicality of the two sample distributions, e.g., minimal separation between both samples. This conclusion can also be drawn from nearly equal sample statistics e.g., mean values of 7.59 km and 7.52 km and medians of 7.25 km and 7.52 km (both tornadic and nontornadic respectively) . It is apparent that no meaningful differences exist between tornadic and nontornadic sample scans of mean Z_{DR} arc width.

The Z_{DR} arc area comparison (Fig. 4.4) yielded statistically significant results, and

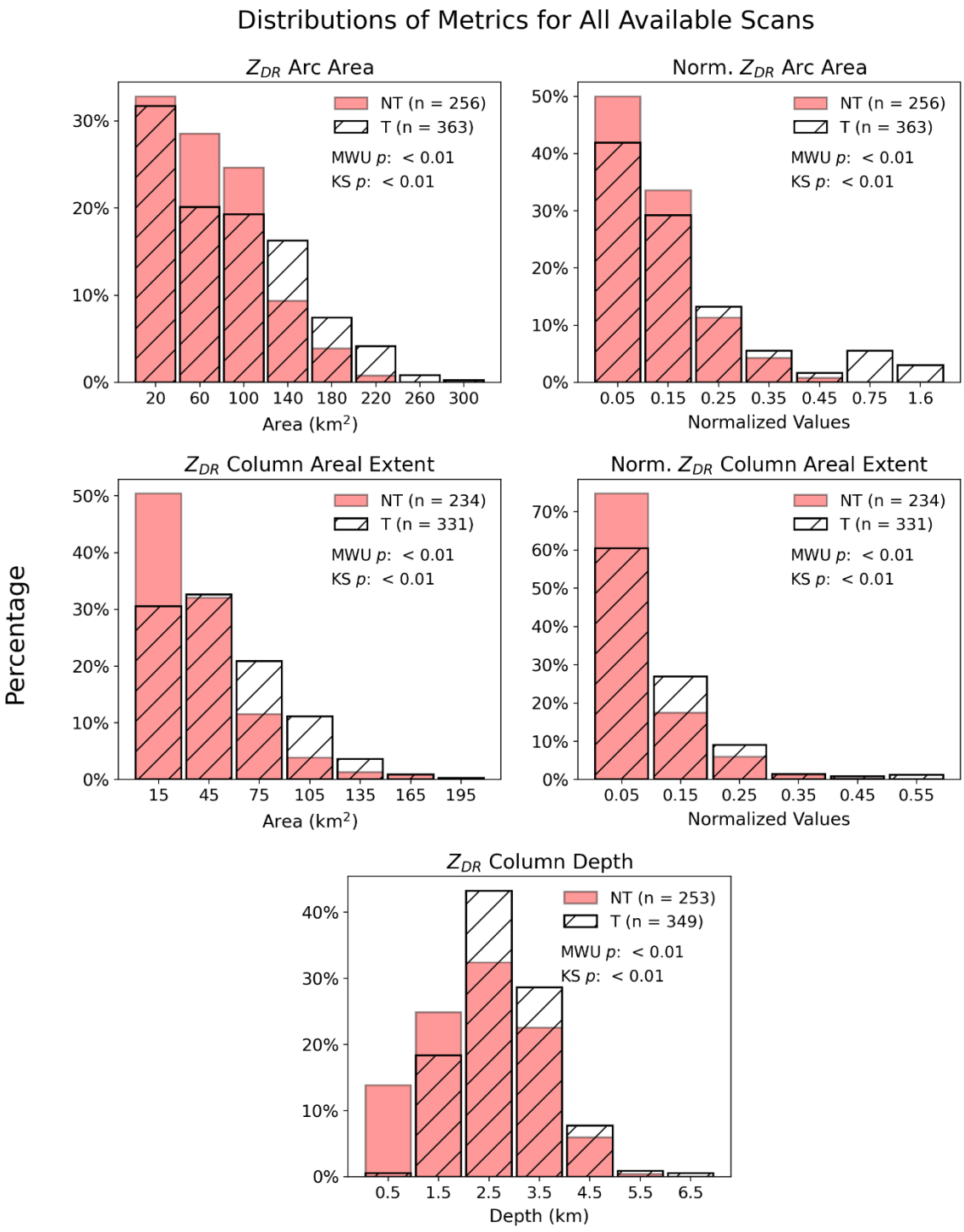

Figure 4.4: As in Fig. 4.3, for Z_{DR} arc area (top left), normalized Z_{DR} arc area (top right), Z_{DR} column areal extent (middle left), normalized Z_{DR} column areal extent (middle right), and Z_{DR} column depth (bottom). Note that for normalized Z_{DR} arc area, all bins were not uniform in size due to a few storms with normalized values greater than one.

based on the sample distributions, sample scans from tornadic storms tended to be skewed towards larger arc areas than that of nontornadic samples for arc areas above the 120 km^2 threshold. However, ~ 70% of tornadic samples and ~ 85% of nontornadic samples were below this threshold and medians of 77.4 km^2 and 60.93 km^2 and mean values of 84.88 km^2 and 66.83 km^2 (tornadic and nontornadic, respectively) demonstrate that there is typically not much difference in the size of the Z_{DR} arc area between tornadic and nontornadic samples despite statistically significant results. Variability is still evident in the metric between both storm categories, and similar to the inferred HAE metric, the arc area is dependent upon the overall size of a storm. The normalized Z_{DR} arc area metric comparison (Fig. 4.4) also yielded statistically significant results with a similar sample distribution spread as the raw metric comparison with ~ 70% of tornadic samples and ~ 85% of nontornadic samples below the 0.20 normalized value threshold, e.g., the Z_{DR} arc area occupied < 20% of the storm area in most samples. As previously discussed, bin differences were not all equal for this metric, with bin values in Fig. 4.4 matching those used in Fig. 4.2. Despite statistically significant results from the KS and MWU tests, it is not apparent that differences among the raw Z_{DR} arc area and normalized values would be meaningful to a forecaster for differentiating between tornadic and nontornadic supercells.

Regarding the metrics obtained from characteristics of the Z_{DR} column, statistically significant results were obtained for all three metrics. The Z_{DR} column areal extent metric comparison (Fig 4.4) exhibits results also supports the inference that Z_{DR} columns tend to be larger in tornadic sample scans. For tornadic samples, ~ 70% of scans were > 30 km^2 and ~ 40% of scans were > 60 km^2, while for nontornadic samples, ~ 50%

of scans were between 0 – 30 km^2 with ~20% of scans exceeding 60 km^2. Sample statistics also help support this inference, e.g., mean values of 53.23 km^2 and 36.22 km^2 and medians of 44.72 km^2 and 36.22 km^2 (tornadic and nontornadic respectively). The normalized Z_{DR} column areal extent comparisons (Fig 4.4) help illustrate how persistent the storm-size relative column area is through all sample scans, with ~ 60% tornadic samples and > 70% of nontornadic samples exhibiting a normalized value between 0.0 – 0.10 and just under 30% of tornadic and 20% of nontornadic samples falling within the 0.10 – 0.20 bin.

For Z_{DR} column depth, (Fig 4.4), statistically significant results were determined from the KS and MWU tests. Qualitatively, it can be inferred that tornadic sample scans tend to have larger column depths than that of nontornadic sample scans. Among the tornadic samples, ~ 80% of samples have a Z_{DR} column depth > 2 km while ~ 50% of nontornadic samples are < 2 km. Based on the results, it could be inferred that Z_{DR} column depth tends to be greater in magnitude more frequently among sample scans from tornadic storms, however the sample statistics depict a smaller separation between typical values for tornadic and nontornadic samples, e.g., mean values of 2.80 km and 2.26 km and medians of 2.69 km and 2.34 km (tornadic and nontornadic respectively).

In order to further test the comparison of metrics between tornadic and nontornadic samples, sample statistics of each metric from each storm including storm-mean, -median, and -maximum values were computed, and the resulting tornadic and nontornadic distributions were again subjected to a KS and MWU test. The resulting box and violin plots below display these distributions, along with annotations for the results of the statistical tests and the sample sizes. In Fig. 4.5, the sample statistics of the

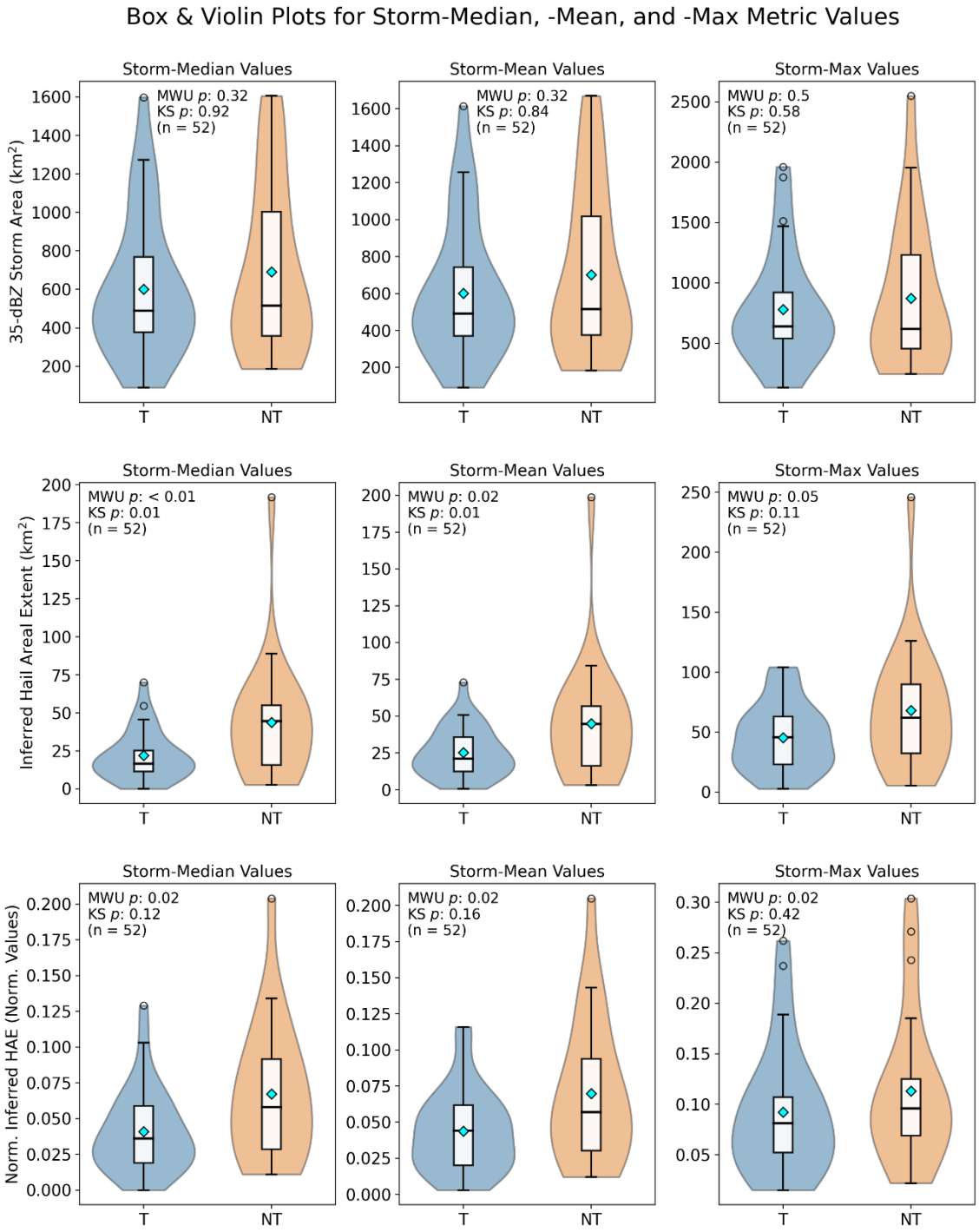

Figure 4.5: Box & violin plots of storm-median, mean, and -max metric values calculated over the duration of a storm's observation period for (top row) 35-dBZ storm area, (middle row) inferred hail areal extent, and (bottom row) normalized inferred hail areal extent. Annotations are provided for the sample distribution means (cyan diamond), KS and MWU test *p*-values, and the sum of both the tornadic and nontornadic sample statistic distributions.

35-dB*Z* storm area, the inferred HAE, and the normalized values of inferred HAE are shown.

All three sample statistic comparisons of the 35-dB*Z* storm area (Fig. 4.5) did not yield statistically significant results, and examination of the box and violin plots shows similar kernel densities and distributions of the sample statistics among both tornadic and nontornadic samples where the storm-median distributions had mean values of 600.47 km^2 and 691.23 km^2 and median values of 489.8 km^2 and 514.0 km^2 and the storm-max distributions had mean values of 641.0 km^2 and 617.4 km^2 and medians of 778.59 km^2 and 872.42 km^2 (all tornadic and nontornadic respectively). This is consistent with the prior results involving all available sample scans, and further confirms the inference that the areal coverage of the storm echo is not an effective measure of characterizing between tornadic and nontornadic samples.

For the inferred HAE metric (Fig. 4.5), two of the three sample statistic comparisons yielded statistically significant results including storm-median and -mean inferred HAE. Generally, for all three sample statistics, inferred HAE had a smaller range of values in tornadic storms than nontornadic storms. The mean value of the storm-mean distributions of inferred HAE was ~ 20 km^2 less in tornadic storms (25.34 km^2 and 45.0 km^2 comparatively). The mean values of the storm-max distributions also differed by ~ 23 km^2, with nontornadic storms tending to have a greater storm-maximum value of inferred HAE (68.14 km^2 compared to 45.63 km^2). This remains consistent with observations of the polarimetrically inferred hail signature by KR08 and VDB20.

While the raw inferred HAE metric sample statistics depicted a strong statistical signal, the sample statistics of the normalized inferred HAE (Fig. 4.5) depict a weaker

difference among tornadic and nontornadic samples. For all three sample statistics, the normalized inferred HAE failed to reject the null hypothesis of the KS test, but did yield statistically significant results for the MWU tests. Based on the characteristics of the two non-parametric tests, this implies significant differences in the median values of the sample distributions but not in their shapes or sizes. The median values of the distributions of sample statistics included 0.036 and 0.048 for storm-median values, 0.044 and 0.057 for storm-mean values, and 0.081 and 0.096 for storm-maximum values (all tornadic and nontornadic respectively). The normalized comparison also further enhances the importance of examining the storm-relative size of the polarimetric signature, e.g., comparing the raw metric values of larger signatures within larger storms to smaller signatures among smaller storms may not yield meaningful results.

Sample statistics of the maximum storm core Z_{HH} values (Fig. 4.6) exhibited a strong statistical signal in the differences between tornadic and nontornadic storms, where storm-median, -mean, -maximum values were deemed significantly different by both tests, with the exception being the KS test among the storm-max sample statistic comparison. For this metric, the mean values of the storm-maximum and storm-mean distributions were less in tornadic storms by 4 dB*Z* and 3 dB*Z* respectively, e.g., 65.26 dB*Z* and 68.5 dB*Z* for the storm-maximum distributions, and 62.19 dB*Z* and 66.1 dB*Z* for the storm-mean distributions (all tornadic and nontornadic respectively). Although the statistical signal is strong, a typical difference in reflectivity values of 3 – 4 dB*Z* would likely not be useful to a warning forecaster. This metric could be more useful in conjunction with the inferred HAE metric. For example, larger hail signatures with enhanced dB*Z* values as demonstrated by the nontornadic storms in this study could

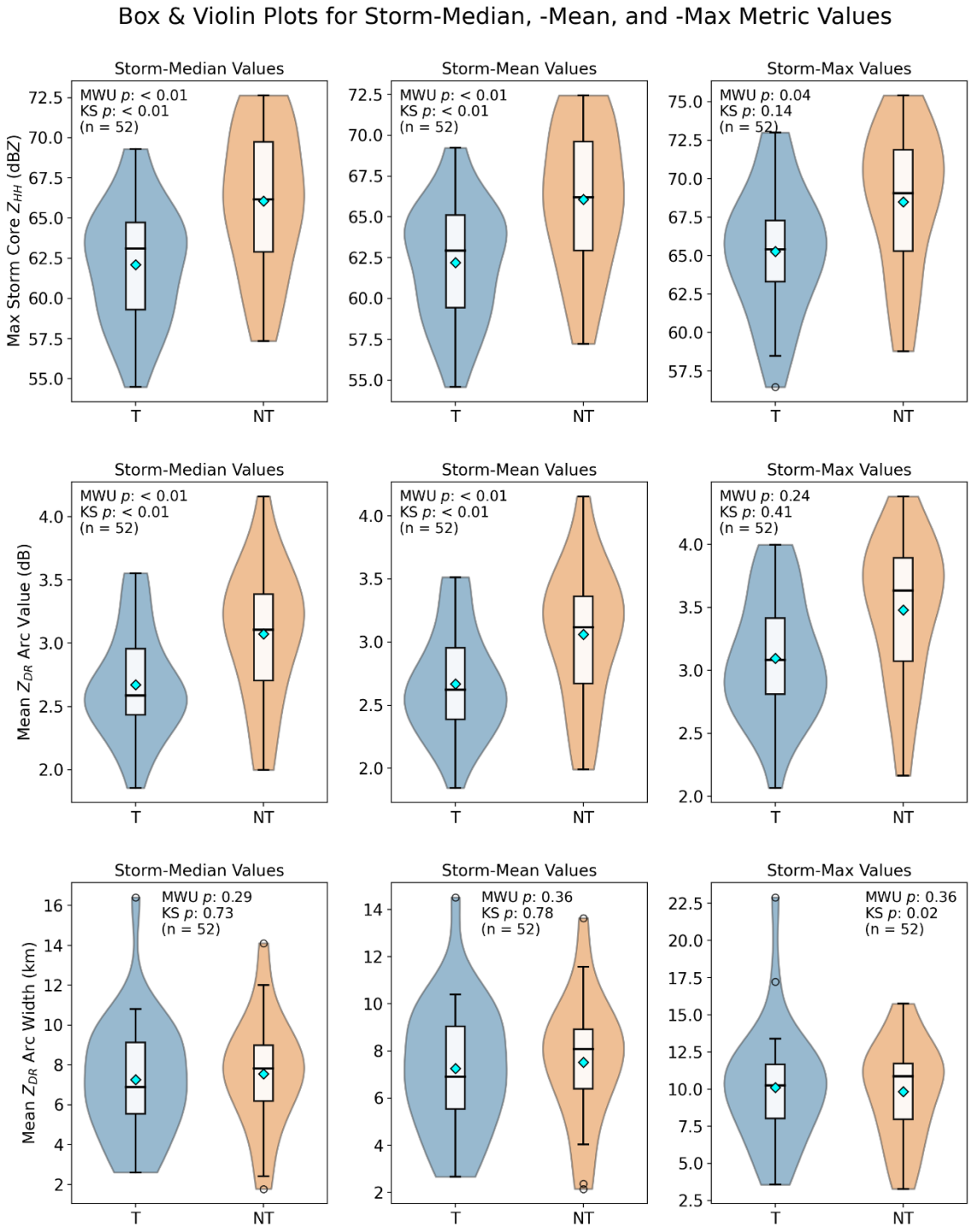

Figure 4.6: As in Fig. 4.5, for (top row) max storm core Z_{HH} value, (middle row) mean Z_{DR} arc value, and (bottom row) mean Z_{DR} arc width.

be used to identify the microphysical processes dominating a storm, and potentially infer near-storm environmental conditions.

In Fig. 4.6, the distributions of storm-median, -mean, and -maximum metric values are shown for the mean Z_{DR} arc value metric. The distributions of sample statistics were deemed significantly different for the storm-median and -mean samples, however the storm-max samples failed to reject the null hypotheses of the KS and MWU tests. The storm-maximum values for the mean Z_{DR} arc value were on average 0.5 dB larger in nontornadic storms than tornadic storms, e.g., 3.5 dB compared to 3 dB respectively. The range of the three sample statistic distributions for this metric did not vary greatly, and generally speaking the only difference in ranges was on the top end of the distributions where the nontornadic samples were larger by ~ 0.5 dB. Despite being significantly different, and physically, a 0.5 dB difference in a Z_{DR} value implying different shaped hydrometeors, the results of this comparison lack in nowcasting and warning decision value and are presented as an observation of storm microphysical differences between tornadic and nontornadic storms, this being that within the sample of storms, nontornadic sample statistics of the mean Z_{DR} arc value metric yielded a drop size distribution skewed towards more oblate rain drops within the Z_{DR} arc region.

Overall, the mean Z_{DR} arc width metric (Fig. 4.6) was not shown to be significantly different for storm-median and -mean values, but did exhibit a significant *p*-value for the storm-maximum values KS test. Distributions of sample statistics between tornadic and nontornadic storms were similar in range and exhibited insignificant differences, and therefore the metric would likely not be a useful factor for distinguishing between tornadic and nontornadic storms.

For the Z_{DR} arc area comparison (Fig. 4.7), neither the storm-median or -mean value comparisons yielded a significant difference between the distributions. This can be seen in the differences of the sample statistic distribution median values, e.g., for the storm-median distributions, the median values only differed by ~ 6 km^2 (69.32 km^2 compared to 63.42 km^2) and for the storm-mean distributions, the median values differed by ~ 7 km^2 (70.4 km^2 and 63.6 km^2) between tornadic and nontornadic samples respectively. However, the distributions of storm-maximum values were deemed significantly different by both the KS and MWU tests with the mean values of the tornadic storm-maximum distribution exceeding the nontornadic values by ~ 18 km^2 (129.9 km^2 compared to 111.3 km^2) while the median values only differed by ~ 7 km^2 (125.1 km^2 compared to 118.16 km^2). It is worth noting that for tornadic storms, a much wider range of values for Z_{DR} arc area were observed and exceeded the top end of the nontornadic distributions by over 40 km^2 for storm-mean and -maximum values, and over 50 km^2 for the storm-median values. Based on the limited significant differences for this metric among tornadic and nontornadic samples, it is likely not a useful factor for differentiating between tornadic and nontornadic supercells due to its dependence on the size of a storm, similar to the inferred HAE metric.

The normalized Z_{DR} arc area metric aids in creating a uniform comparison between tornadic and nontornadic samples, however a similar result is inferred from the sample statistic distribution comparisons shown in Fig. 4.7. It is noted that despite unique shape differences in the kernel densities, this was due to an outlier sample statistic for reasons previously discussed. The normalized metric values also fail to present a strong statistical signal with all three sample statistic distribution comparisons exhibiting KS

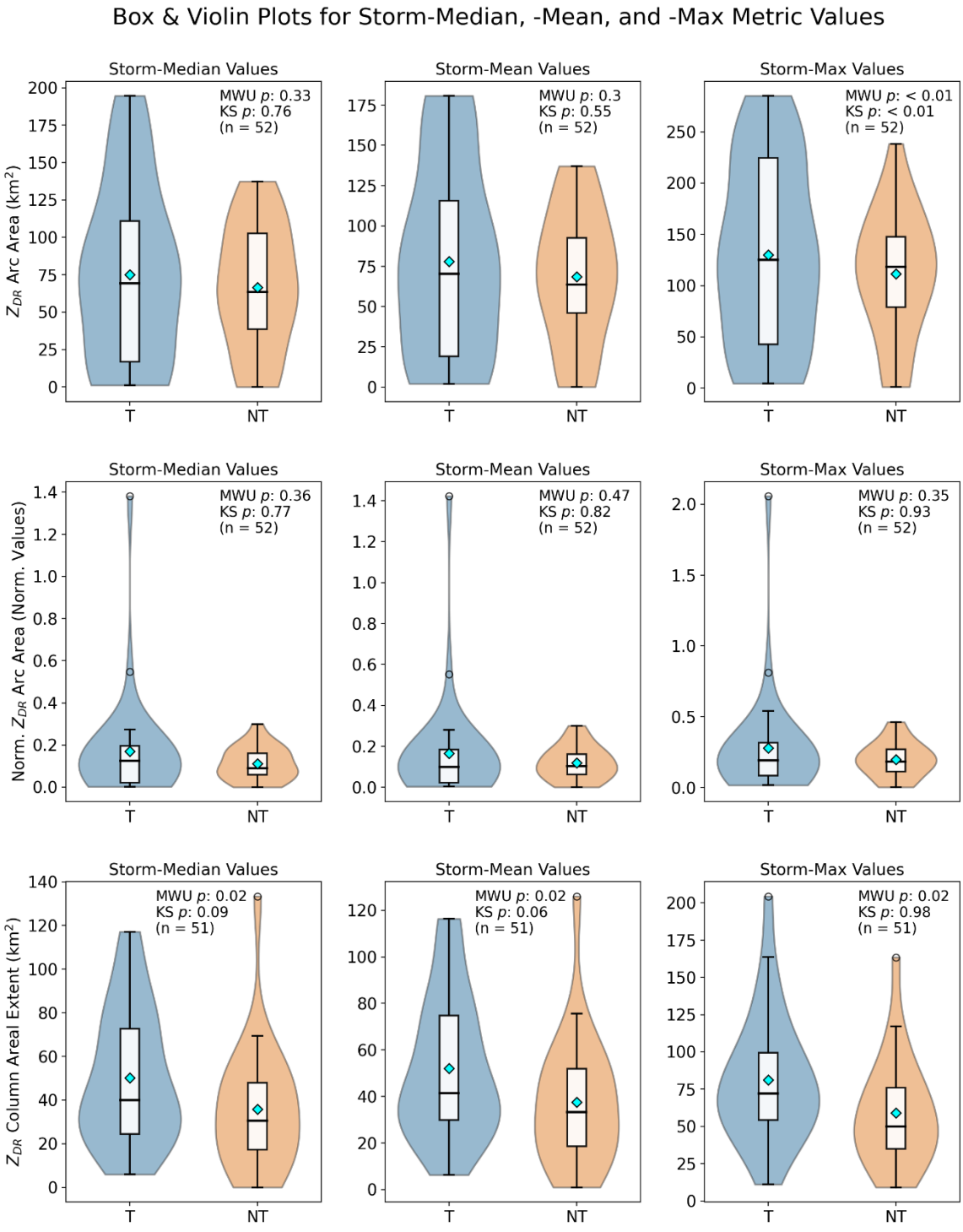

Figure 4.7: As in Fig. 4.5, for (top row) Z_{DR} arc area, (middle row) normalized Z_{DR} arc area, and (bottom row) Z_{DR} column areal extent. Note that the Z_{DR} column areal extent metric only includes 51 storms due to one storm lacking quality data through the observation period.

and MWU test p-values > 0.05. With a lack of significant results, the Z_{DR} arc area metric (raw and normalized) does not distinguish tornadic and nontornadic samples with skill, however the normalized comparison is preferred as it provides more context than comparing the raw metric values.

For Z_{DR} column areal extent (Fig. 4.7), all three sample statistic comparisons were shown to be significantly different by the MWU test, but not by the KS test, implying significantly different distribution median values. Z_{DR} column area spanned a larger range of values for all three sample statistics among tornadic samples compared to nontornadic samples. Tornadic samples fell between 6 km^2 – 117 km^2 (storm-median samples), 6 km^2 – 116 km^2 (storm-mean samples), and 10 km^2 – 170 km^2 (storm-max samples), while nontornadic samples were between 0 km^2 – 133 km^2, 1 km^2 – 80 km^2, and 10 km^2 – 120 km^2, respectively. The mean values of the tornadic sample distributions were larger than those of the nontornadic samples by at least 15 km^2 and as much as 20 km^2, while the sample distribution median values were larger by at least 10 km^2 than those of nontornadic samples.

Similar to the prior normalized metric comparisons, the normalized Z_{DR} column areal extent metric provides a uniform comparison of the ratio of storm area occupied by the polarimetrically inferred updraft region (Fig. 4.7). For all three sample statistic comparisons, significant results were found from the KS and MWU tests. Similar ranges of values were noted for each sample statistic, e.g., median value ranges of 0.027 – 0.27 and 0.0 – 0.276, mean value ranges of 0.032 – 0.31 and 0.002 – 0.284, and maximum value ranges of 0.044 – 0.564 and 0.018 – 0.451, all of which are listed tornadic and nontornadic respectively. Despite significant results from the KS and MWU tests, sample

distribution median values do not exhibit differences that could be useful in an operational setting, e.g., for the median sample statistic distributions, median values were 0.085 and 0.05, for the mean sample statistic distributions, median values were 0.09 and 0.054, and for the maximum sample statistic distributions, median values were 0.16 and 0.087 (all of which are listed tornadic and nontornadic respectively).

From Fig. 4.8, the Z_{DR} column depth comparison was not shown to be significantly different for the storm-median and -mean sample statistic distributions, however significant results ($p < 0.05$) were found for the storm-max sample distributions. Among tornadic samples, both the storm-median and -mean sample distributions exhibited a smaller range of values than that of the nontornadic sample distributions, e.g., for storm-median, metric values were between 1.43 km – 4.3 km and 0 km – 4.17 km (tornadic and nontornadic respectively), and storm-mean values were between 1.74 km – 4.6 km and 0.33 km – 3.94 km (tornadic and nontornadic respectively). For both sample statistic distributions, the distribution median and mean values differed by < 0.50 km. For the storm-max sample distributions, the median and mean values also only differed by < 0.50 km despite significant *p*-values for both the KS and MWU tests. The values ranged between 2.65 km – 6.15 km for tornadic samples, and 1.59 km – 5.15 km for nontornadic samples. Statistical results for this metric comparison are not supportive of a meaningful difference between tornadic and nontornadic samples, however a few patterns are noted among all three sample statistic distributions: 1) Z_{DR} column depth in tornadic samples exhibited a greater maximum value and a greater minimum value than nontornadic samples, 2) a smaller range of values was observed among tornadic samples than that of nontornadic samples, of which both patterns may be

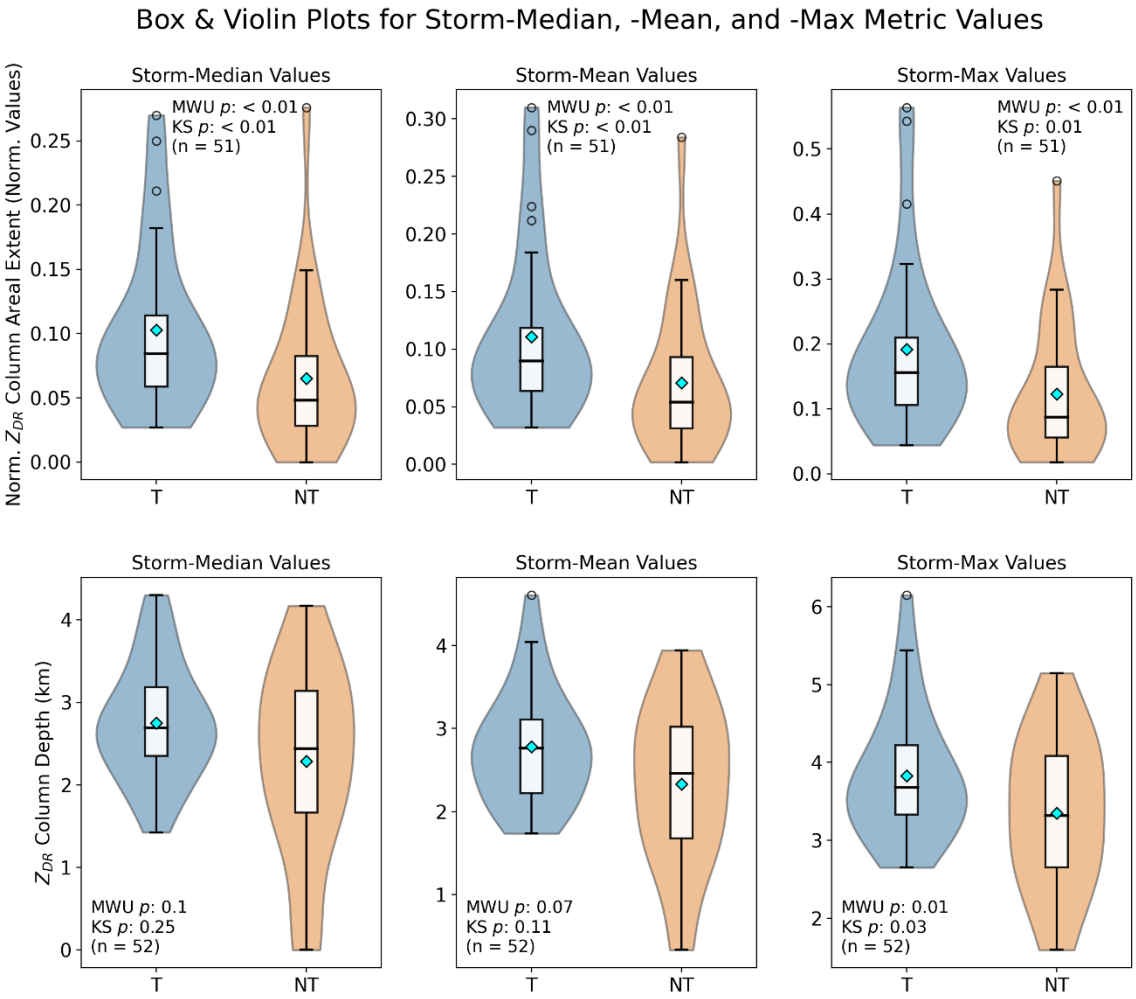

Figure 4.8: As in Fig. 4.5, for (top row) normalized Z_{DR} column areal extent and (bottom row) Z_{DR} column depth. Note that the normalized Z_{DR} column areal extent metric only includes 51 storms due to one storm lacking quality data through the observation period.

indicative of deeper and more steady-state Z_{DR} columns from tornadic samples.

Based on the observations presented, discrete right-moving supercells which become tornadic tend to have taller and broader updrafts as inferred by the characteristics of the Z_{DR} column, which is consistent with previous findings (e.g., Scharfenberg et al. 2005; Kumjian et al. 2010; VDB20). Additionally, Coffer and Parker (2016, 2018) examined simulations of supercells from VORTEX2 composite environments, observing that tornadic supercells exhibited more robust and organized low-level updrafts, co-located

with an intensifying near-surface circulation. In the presence of a stronger updraft within the low-levels, dynamical effects can be further amplified such as the stretching of vertical vorticity, which can aid tornadogenesis, despite often similar near-storm thermodynamic profiles for both tornadic and nontornadic storms.

Lastly, following Kuster et al. (2019), a bootstrapping method with replacement (i = 5000) was applied to the individual radar metrics (including every available sample scan) in order to create non-parametric distributions that could be compared. Non-parametric distributions of sample statistics including median, mean, and maximum were created, and the median values of the 95th percentile range of the distributions were determined. T-NT differences values of the bootstrapped distribution median values were calculated for comparison against the observed sample statistic T-NT median difference values.

In Table 4.1, comparison metrics computed from the storm-median values are presented including: 1) the computed T-NT difference in the median values of the observed sample statistic distributions, 2) the computed T-NT difference of the median values from the 95th percentile bootstrapped sample statistic distributions, and 3) the KS and MWU test p-values from Fig. 4.5 – 4.8 are included. For the storm-median comparison, 6 out of 11 metrics were determined to be significantly different among tornadic and nontornadic samples, however only 2 of these metrics (HAE and mean Z_{DR} arc value) exhibited an observed median difference greater in magnitude than the bootstrapped median difference, where the observed difference for HAE was two times that of the bootstrapping method (e.g., –28.3 km^2 and –14.19 km^2 respectively). The negative values indicate that the median values of tornadic samples were smaller (*in*

Table 4.1: The T – NT difference in median values of sample distributions comprised of observed metric storm-medians, and the T – NT difference in median values of the 95th percentile bootstrapped (i = 5000) distributions. The p-values from the KS and MWU tests for storm-medians shown in Fig. 4.5 through 4.8 are displayed too. Distributions were considered significantly different if one or both of the statistical tests yielded a p-value < 0.05 and are denoted by **. Observed differences greater (*in magnitude*) than the bootstrapping method differences are considered noteworthy.

Median Values

Radar Signature Metric	Observed difference in radar metric median values	95th percentile bootstrapping median differences	KS test results	MWU test results
Storm Area	–24.2 km^2	–10.50 km^2	0.92	0.32
Hail Areal Extent**	–28.03 km^2	–14.19 km^2	0.01	< 0.01
Norm. Hail Areal Extent**	–0.02	–0.02	0.12	0.02
Max Storm Core Z_{HH}**	–3.06 dBZ	–4.06 dBZ	< 0.01	< 0.01
Z_{DR} Arc Area	5.90 km^2	16.29 km^2	0.76	0.33
Norm. Z_{DR} Arc Area	0.04	0.03	0.77	0.36
Mean Z_{DR} Arc Value**	–0.52 dB	–0.48 dB	< 0.01	< 0.01
Mean Z_{DR} Arc Width	–0.95 km	–0.27 km	0.73	0.29
Z_{DR} Column Area**	9.47 km^2	15.04 km^2	0.09	0.02
Norm. Z_{DR} Column Area**	0.04	0.04	< 0.01	< 0.01
Z_{DR} Column Depth	0.25 km	0.35 km	0.25	0.10

magnitude) than nontornadic samples, and stands out as one of the most prominent metrics for differentiating tornadic and nontornadic samples among the storm-median sample statistic. Regarding the updraft proxy metrics, the Z_{DR} column area exhibited promising results, with significance in the MWU test, implying a significant difference in the observed sample medians (e.g., tornadic and nontornadic). Additionally, the observed and bootstrapped median difference values indicate that generally the inferred tornadic updraft area is larger than that within nontornadic storms. This is also reflected in the normalized Z_{DR} column area comparisons with significant results from both the KS and MWU tests, and a T-NT median difference value of ~ 4% in the inferred percentage of the updraft area within the storm area. A similar conclusion can be made for Z_{DR} column

Table 4.2: As in Table 4.1 for the observed metric storm-means with the *p*-values of the KS and MWU tests for storm-means from Fig. 4.5 through 4.8 shown.

Mean Values

Radar Signature Metric	Observed difference in radar metric median values	95th percentile bootstrapping median differences	KS test results	MWU test results
Storm Area	–24.68 km^2	–68.94 km^2	0.84	0.32
Hail Areal Extent**	–23.35 km^2	–17.13 km^2	0.01	0.02
Norm. Hail Areal Extent**	–0.01	–0.02	0.16	0.02
Max Storm Core Z_{HH}**	–3.27 dBZ	–3.74 dBZ	< 0.01	< 0.01
Z_{DR} Arc Area	6.74 km^2	15.69 km^2	0.55	0.30
Norm. Z_{DR} Arc Area	0.00	0.08	0.82	0.47
Mean Z_{DR} Arc Value**	–0.50 dB	–0.38 dB	< 0.01	< 0.01
Mean Z_{DR} Arc Width	–1.17 km	0.06 km	0.78	0.36
Z_{DR} Column Area**	8.10 km^2	16.99 km^2	0.06	0.02
Norm. Z_{DR} Column Area**	0.04	0.03	< 0.01	< 0.01
Z_{DR} Column Depth	0.30 km	0.54 km	0.11	0.07

depth however the signal is not as strong, with a T-NT observed median difference value of 0.25 km and no significant results found from the testing methods.

Of the five remaining metrics which were not deemed significantly different, two metrics (storm area and mean Z_{DR} arc width) also exhibited an observed median difference value greater in magnitude than the bootstrapping method. Similar to the previous comparison methods, the magnitude of difference is important to consider for certain metrics (e.g., max storm core Z_{HH} value, mean Z_{DR} arc value, mean Z_{DR} arc width, and all of the normalized metrics) as they tend not to exhibit differences that are large enough in magnitude to be useful for disseminating tornadic and nontornadic samples.

In Table 4.2, comparison metrics computed from the storm-mean sample statistics are presented as in Table 4.1. Similarly, for the storm-mean values, the same six metrics as in the storm-median comparison were deemed significantly different per the KS and MWU test results. The HAE metric differences are not as large in magnitude for this

Table 4.3: As in Table 4.1 for the observed metric storm-maxes with the *p*-values of the KS and MWU tests for storm-maxes from Fig. 4.5 through 4.8 shown.

Max Values

Radar Signature Metric	Observed difference in radar metric median values	95th percentile bootstrapping median differences	KS test results	MWU test results
Storm Area	23.60 km^2	8.50 km^2	0.58	0.50
Hail Areal Extent	–16.07 km^2	–141.80 km^2	0.11	0.05
Norm. Hail Areal Extent	–0.02	–0.04	0.42	0.17
Max Storm Core Z_{HH}	–3.67 dBZ	–2.42 dBZ	0.14	0.04
Z_{DR} Arc Area**	6.93 km^2	46.77 km^2	< 0.01	< 0.01
Norm. Z_{DR} Arc Area	0.01	1.59	0.93	0.35
Mean Z_{DR} Arc Value	–0.55 dB	–0.38 dB	0.41	0.24
Mean Z_{DR} Arc Width**	–0.60 km	7.16 km	0.02	< 0.01
Z_{DR} Column Area	22.10 km^2	40.87 km^2	0.98	0.46
Norm. Z_{DR} Column Area**	0.07	0.11	0.01	< 0.01
Z_{DR} Column Depth**	0.36 km	1.01 km	0.03	0.01

comparison (e.g., –23.35 km^2 vs. –17.13 km^2) and this also reflects in the normalized inferred HAE comparison, e.g., only a 1% – 2% difference in the percentage of storm area occupied by inferred hail fallout, with nontornadic storms tending to exhibit slightly larger metric values. For the max storm core Z_{HH} value and mean Z_{DR} arc value, a similar conclusion can be drawn, despite significant results, the magnitude at which samples differ between tornadic and nontornadic cases is not great enough to provide value in differentiating between the two categories. The updraft proxy metrics are also comparable to the storm-median results, with agreement between the Z_{DR} column area and the normalized version on larger column areas among tornadic samples, and generally deeper columns as well, but not by a large or significant margin.

Lastly, in Table 4.3, comparison metrics computed from the storm-max sample statistics are presented as in the prior two tables. Some differences are noted with the results of this comparison, including different metrics exhibiting significant differences

among tornadic and nontornadic samples than was observed in Tables 4.1 and 4.2. These metrics included Z_{DR} arc area, mean Z_{DR} arc width, and Z_{DR} column depth. It should be noted that since this comparison was comprised of storm-max samples, the sample statistics generated are likely not the most representative T-NT median difference values, and are presented as observations. Among the metrics which were deemed significant, a few patterns are evident. First, normalized Z_{DR} arc area is skewed towards a significant result due to a select number of sample scans > 1.0 for reasons previously discussed. Generally, the arc area only occupies a small portion of the FFD in a supercell and normalized values exceeding 1.0 are typically not expected. The updraft proxy comparisons revealed strong results with the Z_{DR} column area exhibiting a difference of 22.10 km^2, and the normalized comparison having a difference of 7%, further solidifying the trend of broader Z_{DR} columns among tornadic samples. The Z_{DR} column depth comparison was also shown to be significant among both tests, and had an observed T-NT difference of 0.36 km, also supporting prior notions of deeper Z_{DR} columns among tornadic samples.

Analysis of the tornadic and nontornadic sample comparisons across all three methods employed reveal patterns and differences in several of the metrics. This includes smaller inferred HAE among tornadic samples with less variability than in nontornadic samples, larger magnitude of maximum storm core Z_{HH} values and mean Z_{DR} arc values among nontornadic samples, and generally broader and deeper Z_{DR} columns among tornadic samples. Of the patterns discussed, a few stand out with potential for use in differentiating between tornadic and nontornadic samples, including the significant

results among the inferred HAE metric, and the characteristic differences noted among Z_{DR} columns.

4c. Storm-Based Lag Correlation Testing

Cross-correlation values were computed on an individual storm basis for the radar metric comparisons previously described, with positive and negative lag introduced up to a max of nine volume scans, or approximately 45 minutes in both directions of the zero offset. Of the 52 storm samples in this study, only 13 were included in this calculation, e.g., 9 tornadic storms and 4 tornadic storms, however only 8 tornadic storms were used for comparisons including the Z_{DR} column area and normalized Z_{DR} column area due to poor Z_{DR} column area data quality in one of the storms. Along with individual correlograms for the metric comparisons in each sample, a median correlogram was calculated, and was used as the representative trend.

In the following figures featuring correlograms, a maximum correlation value > 0 that occurs at a negative lag represents an increase in the independent variable (the updraft proxy e.g., Z_{DR} column area) tending to precede an increase in the dependent variable. The opposite is true for maximum correlation values > 0 which occur at a positive lag, e.g., an increase in the Z_{DR} column area would tend to follow an increase in the dependent variable. For a maximum correlation value < 0, this would indicate an inverse relationship, e.g., an increase in the Z_{DR} column area preceding a decrease in the dependent variable (negatively lagged), and an increase in the Z_{DR} column area following a decrease in the dependent variable (positively lagged).

i. Z_{DR} Column Area Metric Comparisons

The results of the storm-based correlation testing are shown for the comparisons utilizing the Z_{DR} column area as the updraft proxy in Fig. 4.9 and 4.10, and a summary of the results is shown in Table 4.4. For tornadic storms, five of seven of the comparisons exhibited a maximum median correlation value at a negative lag, indicating that variability in the Z_{DR} column area tended to precede variability in the corresponding metric. The inferred HAE and normalized inferred HAE comparisons produced peak median correlation values of R~0.46 and 0.41 at lags of –5 minutes and –45 minutes, respectively. These results indicate an increase in the magnitude of the Z_{DR} column area tended to precede an increase in the low-level inferred HAE metrics, where a greater lead time was demonstrated for the normalized inferred HAE comparison. Conversely, the max storm core Z_{HH} value metric comparison exhibited a negative maximum correlation value (R~ –0.37) after 45 minutes of positive lag, indicating that an increase in the magnitude of the Z_{DR} column area tended to follow a decrease in the max storm core Z_{HH} value.

The Z_{DR} arc-based metric comparisons yielded results similar to each other, including the Z_{DR} arc area, normalized arc area, and the mean Z_{DR} arc width. These three metric comparisons had peak median correlation values of R~0.39, 0.43, and 0.33 at –30 minutes, –35 minutes, and –25 minutes of lag, respectively. These results indicated an increase in the magnitude of the Z_{DR} column tended to precede increases in the magnitude of the corresponding metric values. Lastly, the mean Z_{DR} arc value metric comparison exhibited a peak median correlation value (R~0.38) after 20 minutes of positive lag, indicating an increase in the Z_{DR} column area tended to follow an increase in the mean

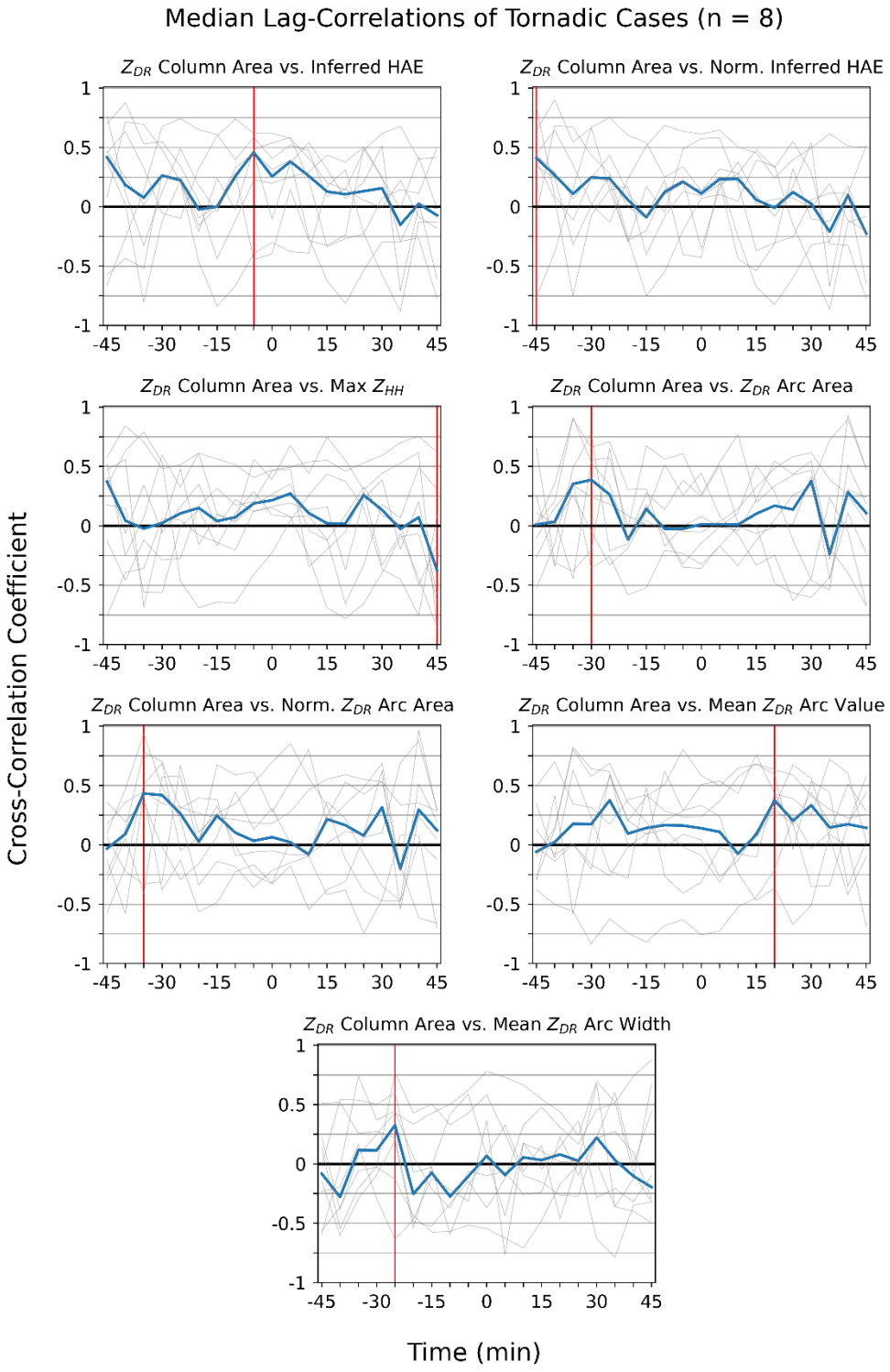

Figure 4.9: Correlograms for the Z_{DR} column area metric comparisons of eight individual tornadic storms which exhibited enough paired metric data points to institute up to 45 minutes of lag in the positive and negative directions. The blue line is the median of all samples, and the red vertical line is the time at which the maximum correlation value (*in magnitude*) is achieved.

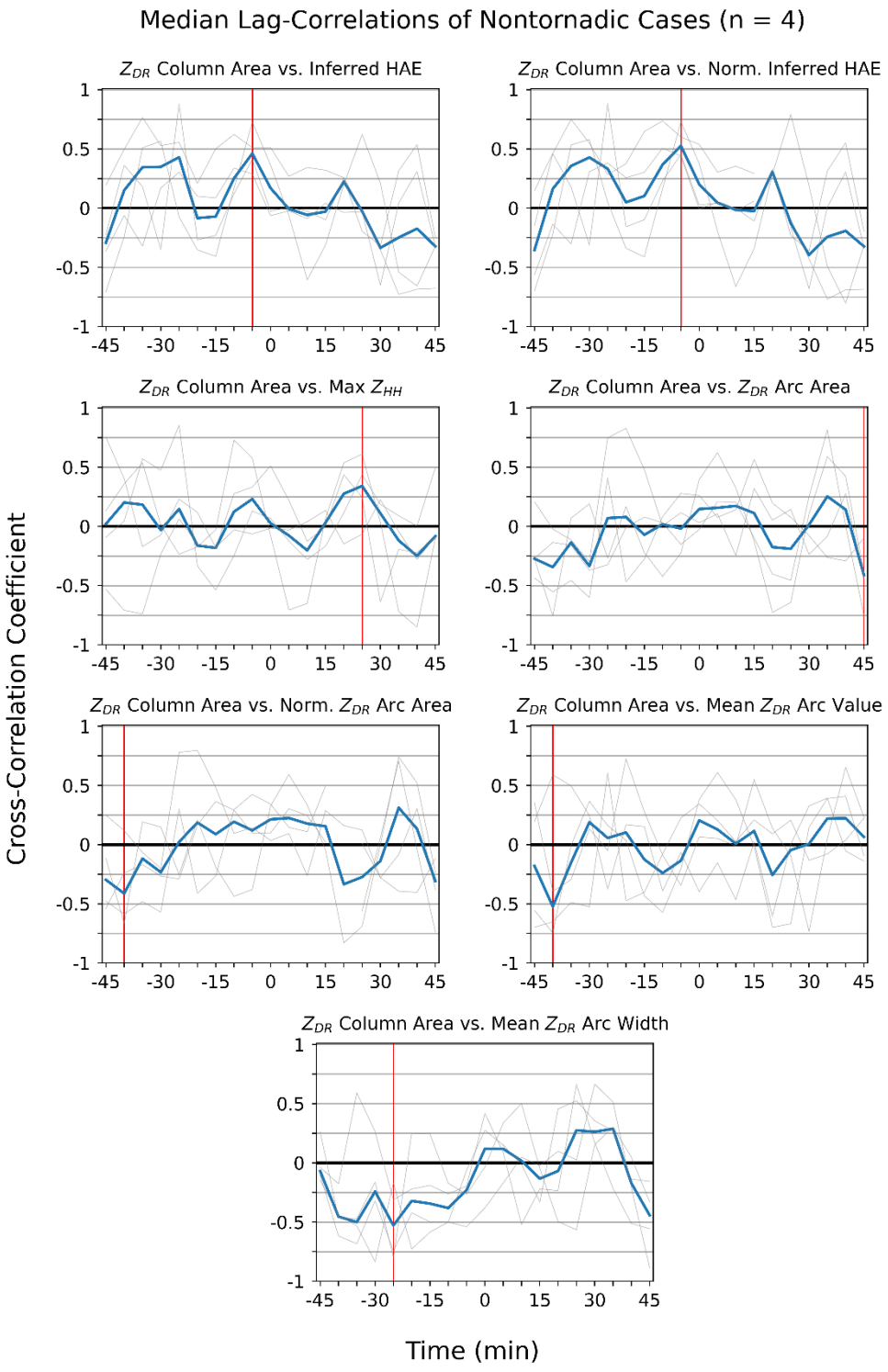

Figure 4.10: As in Fig. 4.9 for four individual nontornadic storms.

Table 4.4: A summary of Fig. 4.9 and 4.10 including the maximum cross-correlation values (*in magnitude*) from the median correlogram for the Z_{DR} column area metric comparisons among the individually tested sample cases, with the corresponding lag at which it occurred.

Z_{DR} Column Area

Tornadic			Nontornadic		
Metric Comparison	Max R-Value	Corresponding Lag (min)	Metric Comparison	Max R-Value	Corresponding Lag (min)
Inferred HAE	0.46	–5	Inferred HAE	0.46	–5
Norm. Inferred HAE	0.41	–45	Norm. Inferred HAE	0.53	–5
Max Storm Core Z_{HH}	–0.37	45	Max Storm Core Z_{HH}	0.34	25
Z_{DR} Arc Area	0.39	–30	Z_{DR} Arc Area	–0.41	45
Norm. Z_{DR} Arc Area	0.43	–35	Norm. Z_{DR} Arc Area	–0.41	–40
Mean Z_{DR} Arc Value	0.38	20	Mean Z_{DR} Arc Value	–0.52	–40
Mean Z_{DR} Arc Width	0.33	–25	Mean Z_{DR} Arc Width	–0.53	–25

Z_{DR} arc value.

For nontornadic storms, a similar pattern was observed among the inferred HAE metric comparisons. Both the inferred HAE and normalized inferred HAE comparisons yielded peak median correlation values (R~0.46 and 0.53) at 5 minutes of negative lag. This was indicative of increases in the Z_{DR} column area preceding increases in the low-level inferred hail fallout metrics, however only by a small margin, e.g., about one volumetric scan or five minutes. Regarding maximum storm core Z_{HH} value, a peak median correlation value of R~0.34) was observed at 25 minutes of positive lag, indicating that an increase in the magnitude of the Z_{DR} column area tended to follow an increase in the max Z_{HH} value.

Among the Z_{DR} arc-based metrics, three of the four metric comparisons yielded a negative peak median correlation value and were negatively lagged. The normalized Z_{DR} arc area (R~ –0.41), mean Z_{DR} arc value (R~ –0.52), and mean Z_{DR} arc width (R~ –0.53) metric comparisons were all shown to decrease in magnitude following an increase in the

Z_{DR} column area by 40 minutes, 40 minutes, and 25 minutes, respectively. Conversely, the Z_{DR} arc area metric comparison (R~ –0.41), was maximized at 45 minutes of positive lag, indicating that an increase in the Z_{DR} column area tended to follow a decrease in the magnitude of the Z_{DR} arc area by 45 minutes.

ii. Normalized Z_{DR} Column Area Metric Comparisons

The same methods were applied using the normalized Z_{DR} column area as the updraft proxy and the results of the corresponding storm-based correlation testing are shown in Fig. 4.11 and 4.12, and a summary of the results is shown in Table 4.5. Among tornadic storms (Fig. 4.11), six of seven metric comparisons exhibited a peak median correlation value at a negative lag, indicating the variability of the normalized Z_{DR} column area tended to precede variability among most of the metrics. The inferred HAE, normalized inferred HAE, and max Z_{HH} value metric comparisons displayed similar correlograms with nearly equivalent peak median correlation values of R~0.44, 0.46, and 0.41 respectively, all of which occurred at 45 minutes of negative lag. Based on the strong similarities observed among the low-level inferred hail fallout metrics, increases in the normalized Z_{DR} column area tended to precede increases among the corresponding metrics by 45 minutes.

The Z_{DR} arc area and normalized Z_{DR} arc area metric comparisons also revealed similar median value correlograms with positive peak median correlation values (R~0.43 and 0.52) at 35 minutes of negative lag, indicating that an increase in the normalized Z_{DR} column area tended to precede an increase in the Z_{DR} arc area and normalized Z_{DR} arc area. The mean Z_{DR} arc width metric comparison yielded the only negative peak median

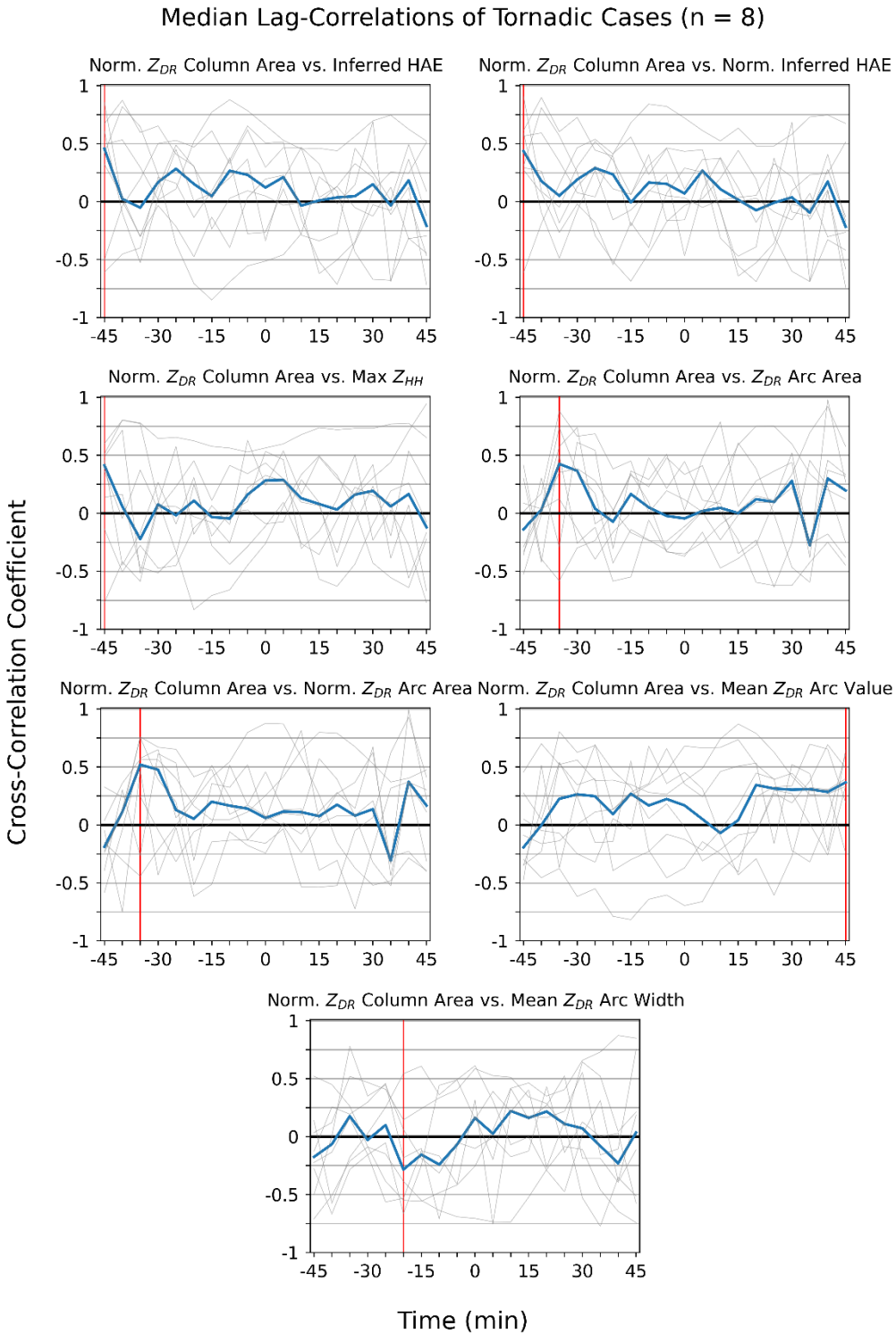

Figure 4.11: Correlograms for the normalized Z_{DR} column area metric comparisons of eight individual tornadic storms which exhibited enough paired metric data points to institute up to 45 minutes of lag in the positive and negative directions. The blue line is the median of all samples, and the red vertical line is the time at which the maximum correlation value (*in magnitude*) is achieved.

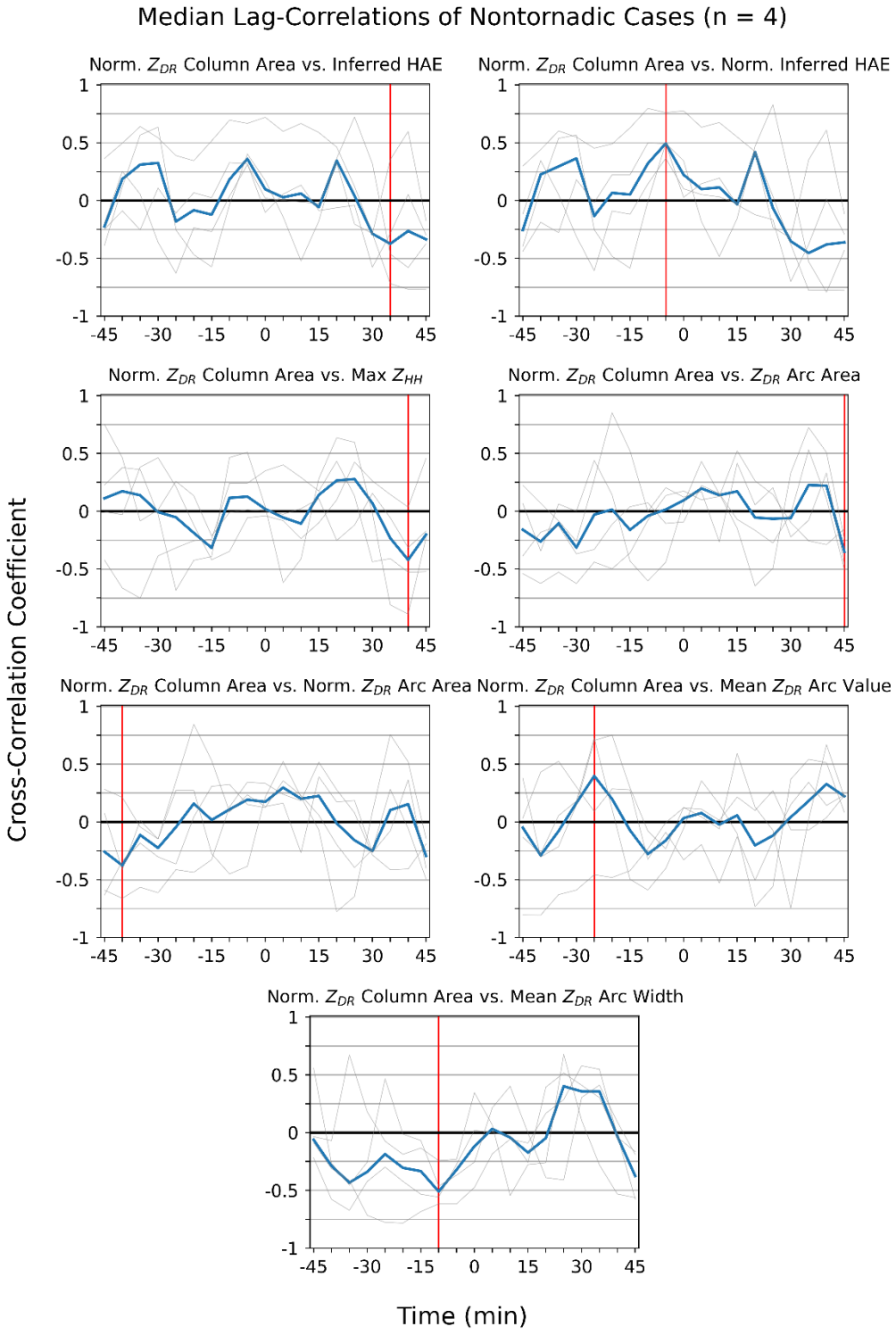

Figure 4.12: As in Fig. 4.11 for four individual nontornadic storms.

Table 4.5: A summary of Fig. 4.11 and 4.12 including the maximum cross-correlation values (*in magnitude*) from the median correlogram for the normalized Z_{DR} column area metric comparisons among the individually tested sample cases, with the corresponding lag at which it occurred.

Norm. Z_{DR} Column Area

Tornadic			Nontornadic		
Metric Comparison	Max R-Value	Corresponding Lag (min)	Metric Comparison	Max R-Value	Corresponding Lag (min)
Inferred HAE	0.46	–45	Inferred HAE	–0.37	35
Norm. Inferred HAE	0.44	–45	Norm. Inferred HAE	0.49	–5
Max Storm Core Z_{HH}	0.41	–45	Max Storm Core Z_{HH}	–0.42	40
Z_{DR} Arc Area	0.43	–35	Z_{DR} Arc Area	–0.35	45
Norm. Z_{DR} Arc Area	0.52	–35	Norm. Z_{DR} Arc Area	–0.38	–40
Mean Z_{DR} Arc Value	0.37	45	Mean Z_{DR} Arc Value	0.40	–25
Mean Z_{DR} Arc Width	–0.28	–20	Mean Z_{DR} Arc Width	–0.51	–10

correlation value among this subset of comparisons, suggesting that an increase in the Z_{DR} column area tended to precede a decrease in the mean Z_{DR} arc width by 20 minutes. Lastly, the mean Z_{DR} arc value metric comparison yielded the only positively lagged result among the seven comparisons, with a peak median correlation value of R~0.37 at 45 minutes of positive lag, indicating an increase in the normalized Z_{DR} column area followed an increase in the mean Z_{DR} arc value by 45 minutes.

Among the low-level hail fallout metric comparisons for nontornadic storms (Fig. 4.12) similar median value correlograms were noted for the inferred HAE and normalized inferred HAE, however due to differences in the amplitudes of the correlograms, contrasting results were observed between the two metric comparisons. For the inferred HAE metric comparison, a peak median correlation value of R~ –0.37 was observed at 35 minutes of positive lag, while the normalized inferred HAE comparison was maximized at 5 minutes of negative lag with a peak median correlation value of R~0.49. This implies two physical conclusions, e.g., a decrease in the inferred HAE would tend to be followed

by an increase in the normalized Z_{DR} column area by 35 minutes, whereas an increase in the normalized Z_{DR} column area tended to precede an increase in the normalized inferred HAE by 5 minutes. Regarding the max Z_{HH} value metric comparison, a decrease in the max Z_{HH} value tended to follow an increase in the normalized column area by 40 minutes (R~ –0.42), and is opposite from the corresponding nontornadic comparison using the raw Z_{DR} column area.

Similar to the low-level inferred hail fallout metrics, the arc area metrics also exhibited similar correlograms, and due to varying amplitudes, differing results were found again between the Z_{DR} arc area and normalized arc area metric comparisons. Both of the comparisons were maximized at a negative median correlation value, indicating an inverse relationship between the variables. An increase in the normalized Z_{DR} column area tended to follow a decrease in the Z_{DR} arc area by 45 minutes (R~ –0.35), and also precede a decrease in the normalized Z_{DR} arc area by 45 minutes (R~ –0.38). For the remaining metric comparisons, an increase in the normalized Z_{DR} column area tended to precede an increase in the mean Z_{DR} arc value by 25 minutes (R~0.40), and tended to follow a decrease in the mean Z_{DR} arc width by 10 minutes (R~ –0.51).

iii. Z_{DR} Column Depth Comparisons

Lastly, the results of storm-based lag correlation testing utilizing the Z_{DR} column depth as the updraft proxy are shown in Fig. 4.13 and 4.14, and a summary of the results is shown in Table 4.6. Among tornadic storms, the metric comparisons of inferred low-level hail fallout exhibited similar results, where an increase in Z_{DR} column depth did not

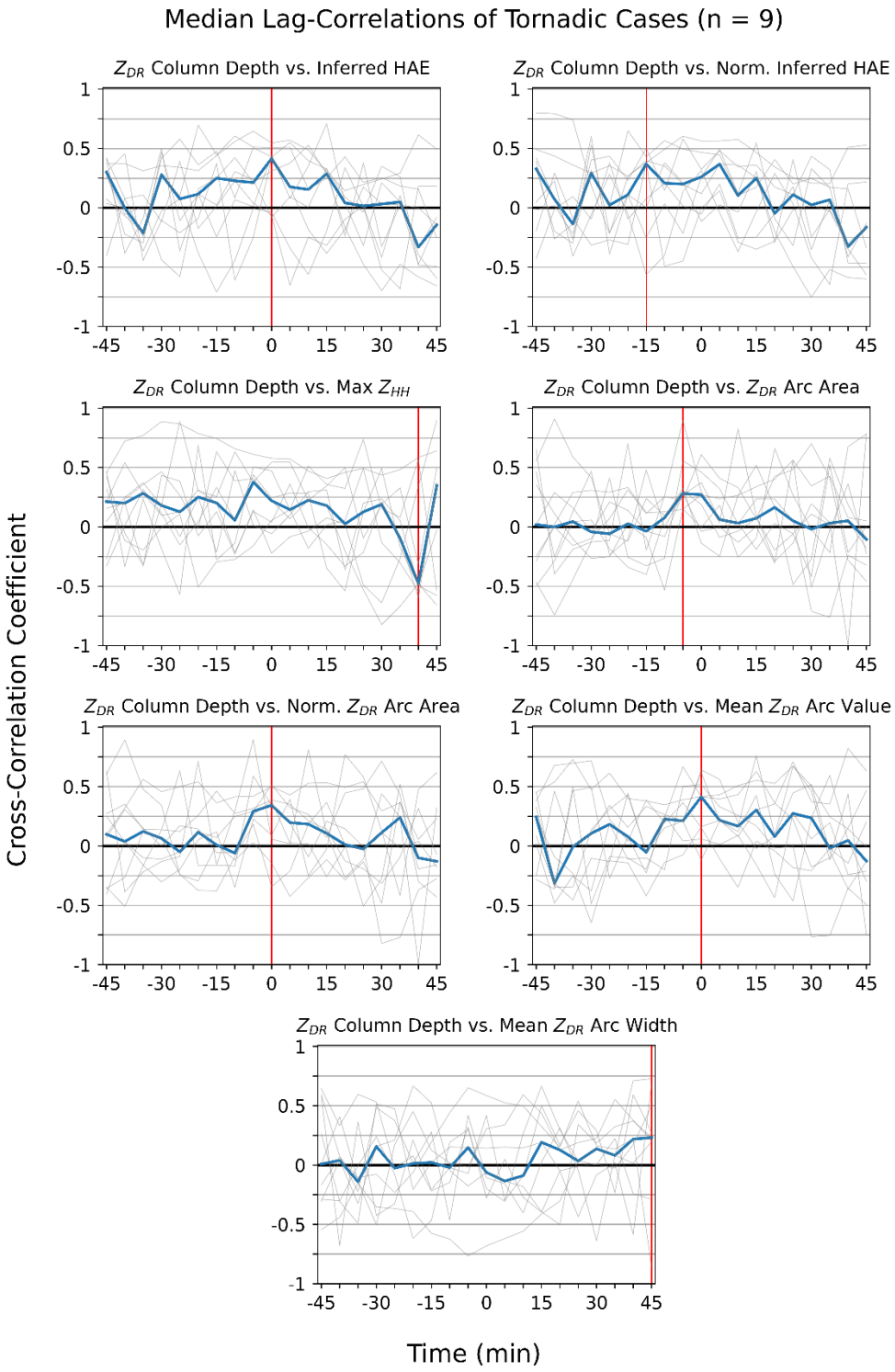

Figure 4.13: Correlograms for the Z_{DR} column depth metric comparisons of nine individual tornadic storms which exhibited enough paired metric data points to institute up to 45 minutes of lag in the positive and negative directions. The blue line is the median of all samples, and the red vertical line is the time at which the maximum correlation value (in magnitude) is achieved.

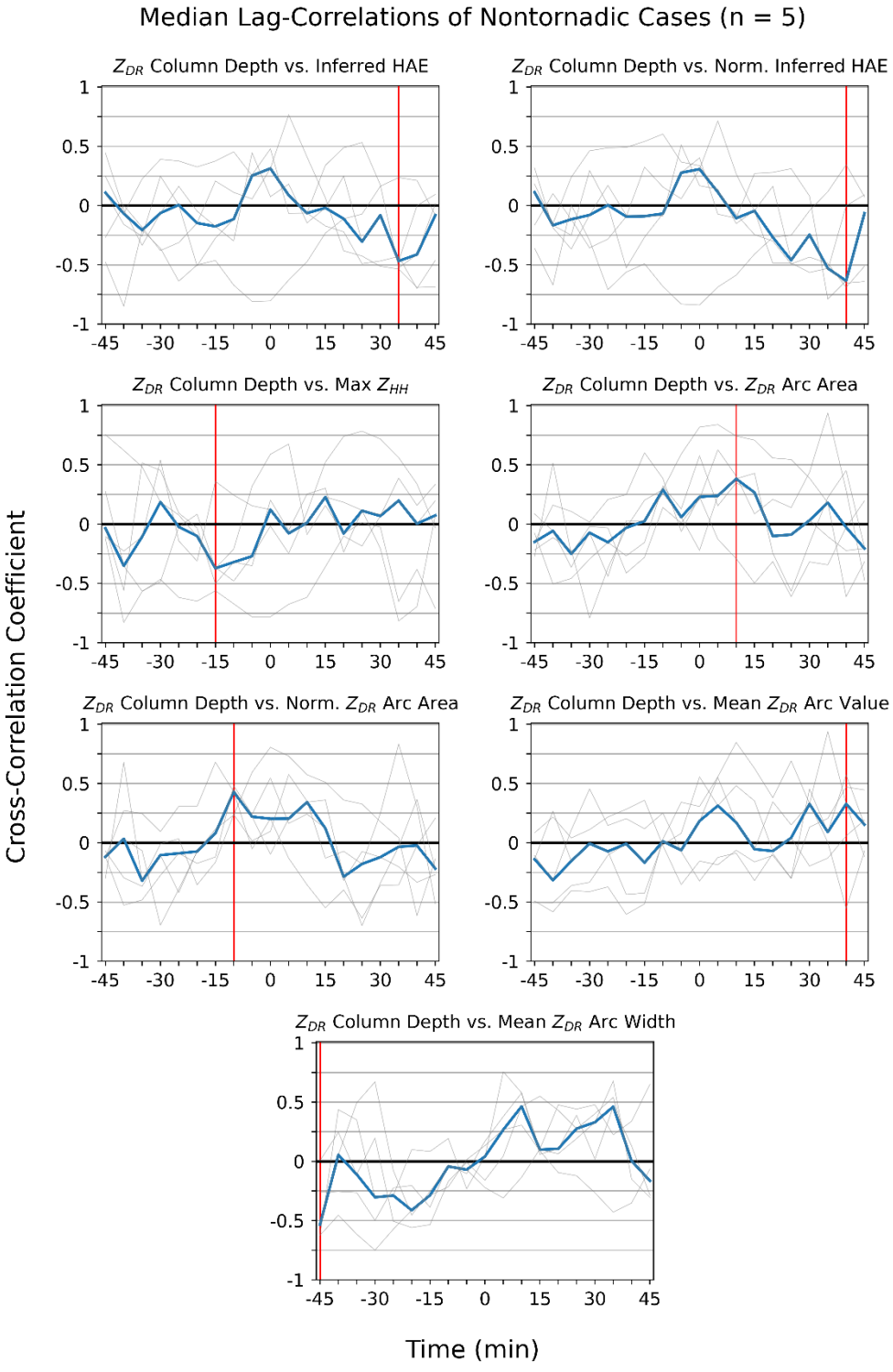

Figure 4.14: As in Fig. 4.13 for five individual nontornadic storms.

Table 4.6: A summary of Fig. 4.13 and 4.14 including the maximum cross-correlation values (*in magnitude*) from the median correlogram for the Z_{DR} column depth metric comparisons among the individually tested sample cases, with the corresponding lag at which it occurred.

Z_{DR} Column Depth

Tornadic			Nontornadic		
Metric Comparison	Max R-Value	Corresponding Lag (min)	Metric Comparison	Max R-Value	Corresponding Lag (min)
Inferred HAE	0.41	0	Inferred HAE	–0.47	35
Norm. Inferred HAE	0.37	–15	Norm. Inferred HAE	–0.64	40
Max Storm Core Z_{HH}	–0.48	40	Max Storm Core Z_{HH}	–0.37	–15
Z_{DR} Arc Area	0.28	–5	Z_{DR} Arc Area	0.38	10
Norm. Z_{DR} Arc Area	0.34	0	Norm. Z_{DR} Arc Area	0.43	–10
Mean Z_{DR} Arc Value	0.41	0	Mean Z_{DR} Arc Value	0.33	40
Mean Z_{DR} Arc Width	0.23	45	Mean Z_{DR} Arc Width	–0.53	–45

tend to lead or lag an increase in inferred HAE with a peak median correlation value at the zero offset (R~0.41). Comparatively, an increase in the Z_{DR} column depth preceded an increase in the normalized inferred HAE by 15 minutes (R~0.37). For the max Z_{HH} metric comparison, a negative peak median correlation value (R~ –0.48) was observed at 40 minutes of positive lag, indicating that an increase in the magnitude of Z_{DR} column depth lagged a decrease in the max Z_{HH} value.

The Z_{DR} arc-based metric comparisons revealed similar results in their respective correlograms against the Z_{DR} column depth. All four metric comparisons revealed a positive peak median correlation value, where the Z_{DR} arc area metric comparison was maximized at 5 minutes of negative lag (R~0.28), indicating an increase in Z_{DR} column depth tended to precede an increase in the Z_{DR} arc area. For the normalized Z_{DR} arc area and mean Z_{DR} arc value metric comparisons, positive peak median correlation values of R~0.34 and 0.41, respectively, were observed at the zero offset, indicating that changes in the magnitude of Z_{DR} column depth did not tend to lead or lag variability in the

magnitudes of normalized Z_{DR} arc area and mean Z_{DR} arc value. Lastly, the mean Z_{DR} arc width metric comparison produced a positive peak median correlation value (R~0.23) after 45 minutes of positive lag, indicating that an increase in the Z_{DR} column depth tended to follow an increase in the mean Z_{DR} arc width by 45 minutes.

Among the nontornadic storm metric comparisons utilizing the Z_{DR} column depth, four comparisons yielded a peak median correlation value less than zero, including all three low-level inferred hail fallout metric comparisons, indicating an inverse relationship. Both the inferred HAE (R~ –0.47) and normalized inferred HAE (R~ –0.64) metric comparisons were found to be maximized at positive lags of 35 and 40 minutes respectively, representing an increase in the Z_{DR} column depth tending to follow a decrease in these two inferred hail fallout metrics by 35 to 40 minutes. The max Z_{HH} metric comparison exhibited a peak median correlation value (R~ –0.37) at 15 minutes of negative lag, indicating that an increase in Z_{DR} column depth tended to precede a decrease in the max storm core Z_{HH} value.

For the comparisons involving the Z_{DR} arc-based metrics in nontornadic storms, results which differed greatly were observed among the four comparisons. The Z_{DR} arc area and normalized Z_{DR} arc area metric comparisons yielded positive peak median correlation values at lags of 10 minutes, and –10 minutes, respectively. This suggests an increase in the Z_{DR} column depth tended to follow an increase in the Z_{DR} arc area by 10 minutes, and precede an increase in the normalized Z_{DR} arc area metric by 10 minutes. The mean Z_{DR} arc value metric comparison yielded a positive peak median correlation value (R~0.33) after 40 minutes of positive lag, indicating an increase in the Z_{DR} column depth tended to follow an increase in the mean Z_{DR} arc value. Lastly, the mean Z_{DR} arc

width comparison yielded a negative peak median correlation value (R~ –0.53) at 45 minutes of negative lag, indicating that an increase in the Z_{DR} column depth tended to precede a decrease in the mean Z_{DR} arc width by 45 minutes.

The results from the individual storm correlation testing are presented as observations for comparison against the bootstrapping method. Due to the small sample size within this applied method, e.g., between four to nine storms, inferences and conclusions from the results should not be used for determining potential skill in an operational setting. Despite this caveat, patterns may still be identifiable for exploration in future work where sample sizes are more significantly sized.

Among the tornadic samples, some consistency was noted in the Z_{DR} column area metric comparisons against Z_{DR} arc area, normalized Z_{DR} arc area, and mean Z_{DR} arc width where increases in the Z_{DR} column area tended to precede increases in the magnitude of these corresponding metrics by 25 – 35 minutes. A greater variability in correlogram trends was observed in the inferred hail fallout metrics among tornadic storms, however two of three metrics (inferred HAE and normalized inferred HAE) did exhibit positive peak median correlation values at negative lags, indicating an increase in the Z_{DR} column area tended to precede an increase in the hail fallout metrics.

Within nontornadic samples, there was not a strong signal indicative of variability in the Z_{DR} column area serving as a precursor to variability in the low-level inferred hail fallout metrics. However, the Z_{DR} arc-based metric comparisons did tend to exhibit a consistent pattern amongst each other, where an inverse relationship was observed, e.g.,

an increase in the magnitude of the Z_{DR} column area tended to precede a decrease in each of the Z_{DR} arc-based metrics by 25 to 40 minutes.

For comparisons utilizing the normalized Z_{DR} column area, considerable consistency was found among all three inferred hail fallout metric comparisons within tornadic samples. All three comparisons demonstrated positive peak median correlation values at 45 minutes of negative lag, indicating increases in the magnitude of the normalized Z_{DR} column area tended to serve as a strong precursor for inferred hail fallout later on. Similar consistency was observed in the Z_{DR} arc area and normalized arc area comparisons where increases in the normalized column area lead increases in the arc area metrics by 35 minutes.

Lastly, among the metric comparisons which utilized the Z_{DR} column depth, greater variability was observed among tornadic and nontornadic samples, with no consistent patterns in either the inferred hail fallout or Z_{DR} arc-based metric comparisons.

4d. Total Sample Lag-Correlation Testing and Bootstrapping

Correlation values based on total samples of tornadic and nontornadic scans were calculated to identify trends of polarimetric signature comparisons among both storm classifications. Due to the criteria for running a lagged correlation test (e.g., after the application of lag, at least six paired scans must remain within an individual storm sample), the total number of paired metric data decreased as the amount of lag increased, previously discussed and shown in Table 4.7. This caveat likely influenced the correlation values at larger lags among the metric comparisons, which warranted the usage of a bootstrapping method. Bootstrapping with replacement (previously discussed

Table 4.7: The total number of paired metric data points included in the total sample calculations for cross-correlations after a lag was applied for the Z_{DR} column area and norm. Z_{DR} column area (top) and Z_{DR} column depth metric comparisons. Tornadic paired metrics are listed first and the nontornadic total is in parentheses. Note that for negative lag, the sample sizes were equivalent to their corresponding negative lag value.

Z_{DR} Column Area & Norm. Z_{DR} Column Area

Lag (min)	T (NT)	Lag (min)	T (NT)
0	317 (217)	25	164 (85)
5	287 (177)	30	137 (50)
10	263 (150)	35	102 (40)
15	224 (130)	40	86 (36)
20	193 (101)	45	66 (32)

Z_{DR} Column Depth

Lag (min)	T (NT)	Lag (min)	T (NT)
0	351 (256)	25	185 (111)
5	319 (223)	30	156 (73)
10	293 (192)	35	114 (55)
15	262 (163)	40	97 (44)
20	222 (136)	45	81 (39)

in Section 3b) was applied to the total samples of tornadic and nontornadic paired metric values in order to create non-parametric distributions of correlation values, from which median values could be obtained, and utilized in comparisons against the observed values.

i. Z_{DR} Column Area Metric Comparisons

The results of the observed data correlograms for total samples of tornadic and nontornadic scans among comparisons using the Z_{DR} column area metric for the updraft proxy are shown in Fig. 4.15 and 4.16. The resulting correlograms featuring the bootstrapped median values and 90th percentile are shown in Fig. 4.17 and 4.18. Apparent differences do not exist in the correlograms between the observed dataset and the

bootstrapped results, which was to be expected from utilizing the bootstrapped median value, thus the summary of the observed data correlograms in Table 4.8 may be applied to the bootstrapped median values as well. This inference will also be applicable for the remaining comparisons utilizing the normalized Z_{DR} column area and Z_{DR} column depth as the updraft proxy.

Within the sample of tornadic scans (Fig. 4.15 and 4.17), the comparison between the Z_{DR} column area and the inferred HAE exhibited some skill in anticipating an increase in inferred HAE. An increase in the magnitude of the Z_{DR} column area were shown to precede an increase in the inferred HAE by 40 min (R~0.46, $p < 0.05$). The remaining two inferred low-level hail fallout metrics were not consistent with this finding, where the normalized inferred HAE metric comparison demonstrated an inverse relationship with an increase in the Z_{DR} column area following a decrease in the normalized inferred HAE by 45 minutes (R~ –0.54, $p < 0.05$). No meaningful results were observed from the max Z_{HH} value metric comparison when compared against the Z_{DR} column area.

Among the four remaining comparisons against Z_{DR} arc-based metrics, Z_{DR} arc area and mean Z_{DR} arc value were shown to be negatively lagged relative to variability of the Z_{DR} column area, while normalized Z_{DR} arc area and mean Z_{DR} arc width were found to be positively lagged, all with statistical significance ($p < 0.05$) at their peak correlation values (*in magnitude)*. Regarding the negatively lagged metrics, this can be interpreted as an increase in the Z_{DR} column area preceding an increase in the magnitude of the Z_{DR} arc area by 35 minutes (R~0.46) and the mean Z_{DR} arc value by 35 minutes (R~0.43). The remaining two metric comparisons revealed one inverse and one direct relationship with

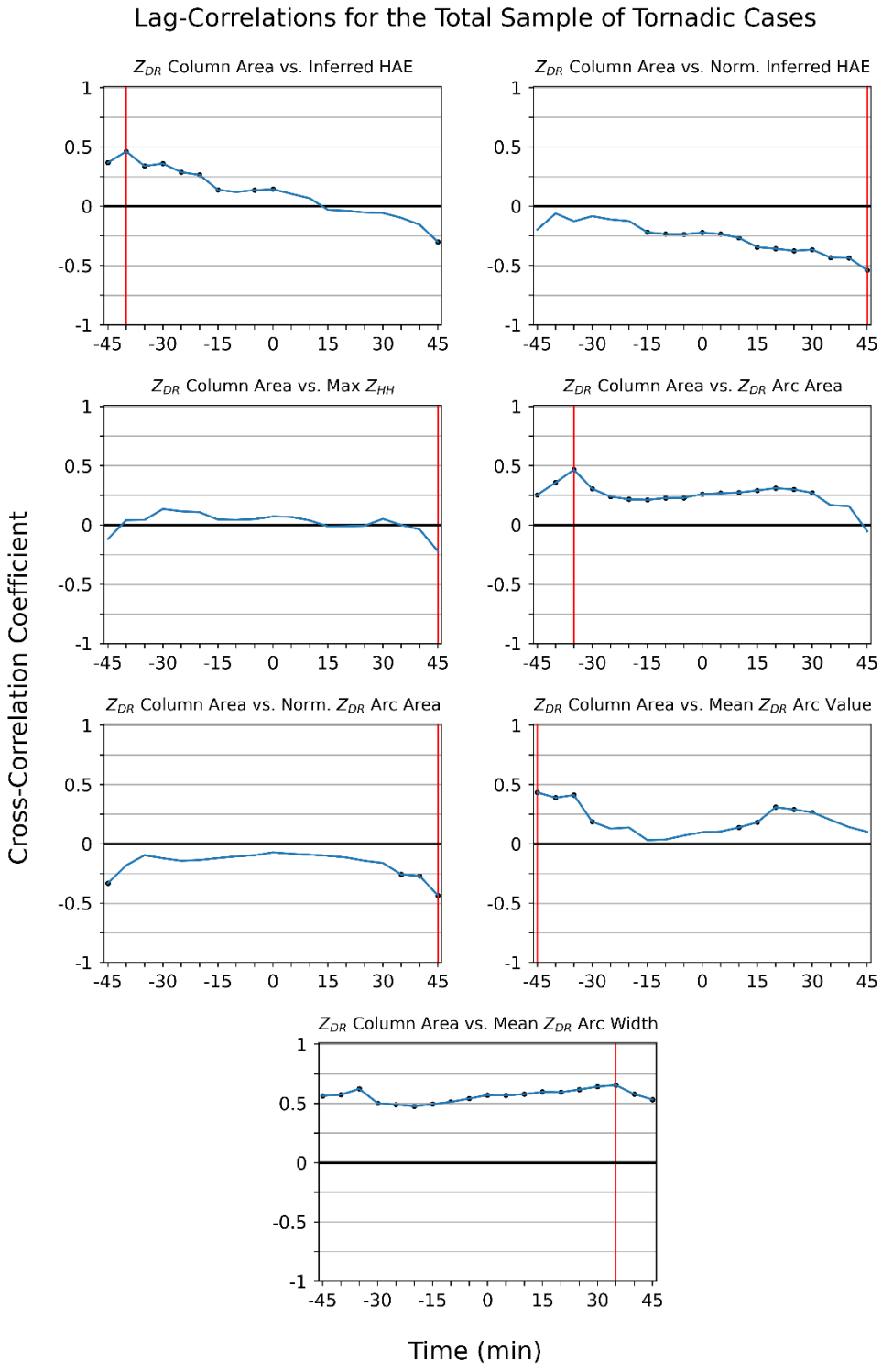

Figure 4.15: Correlograms for the Z_{DR} column area metric comparisons of all available sample scans from tornadic storms. Correlation values determined to be statistically significant ($p < 0.05$) are denoted by a black dot and the red vertical line is the time at which the maximum correlation value (*in magnitude*) is achieved.

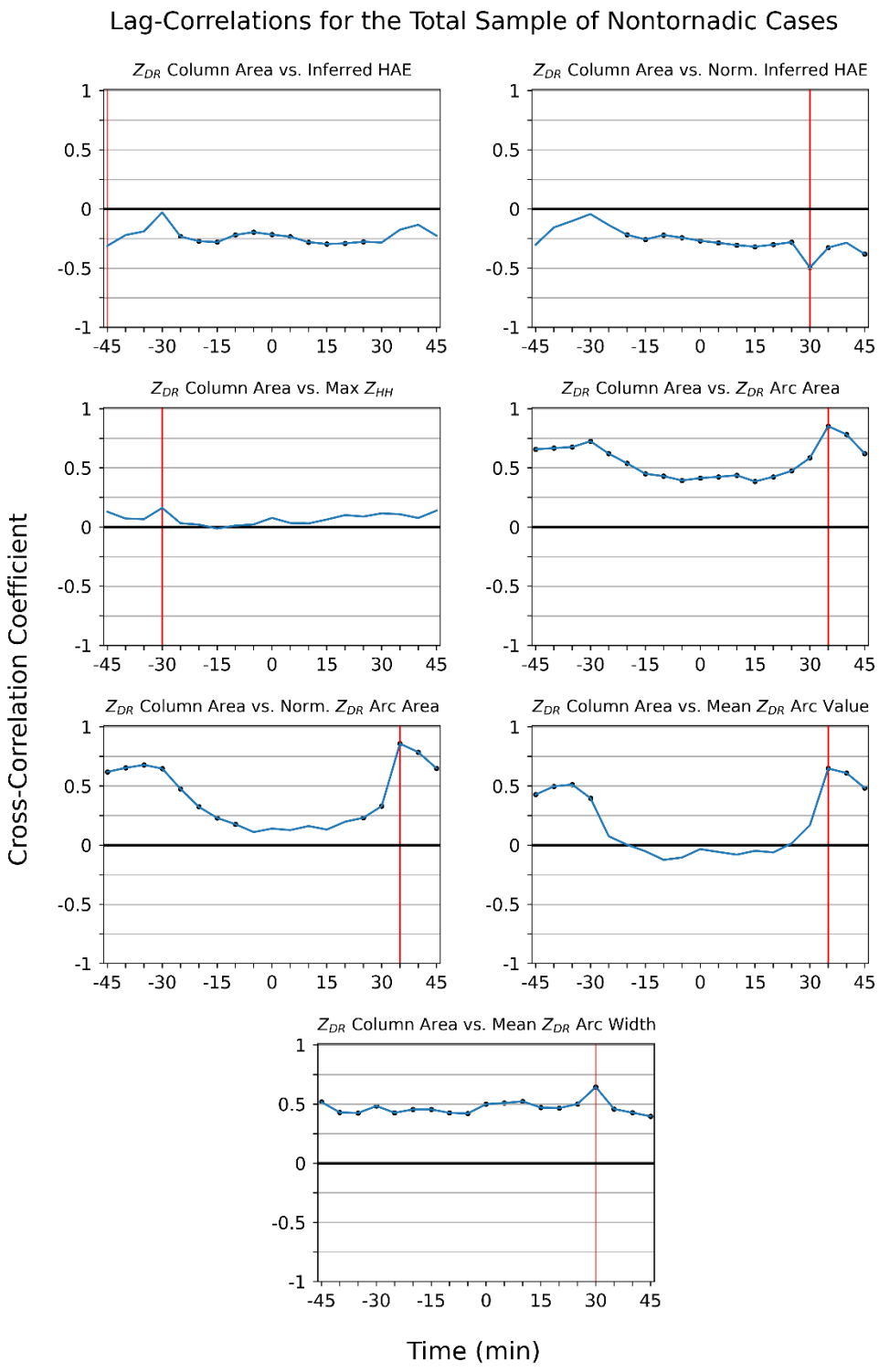

Figure 4.16: As in Fig. 4.15 for all available sample scans from nontornadic storms.

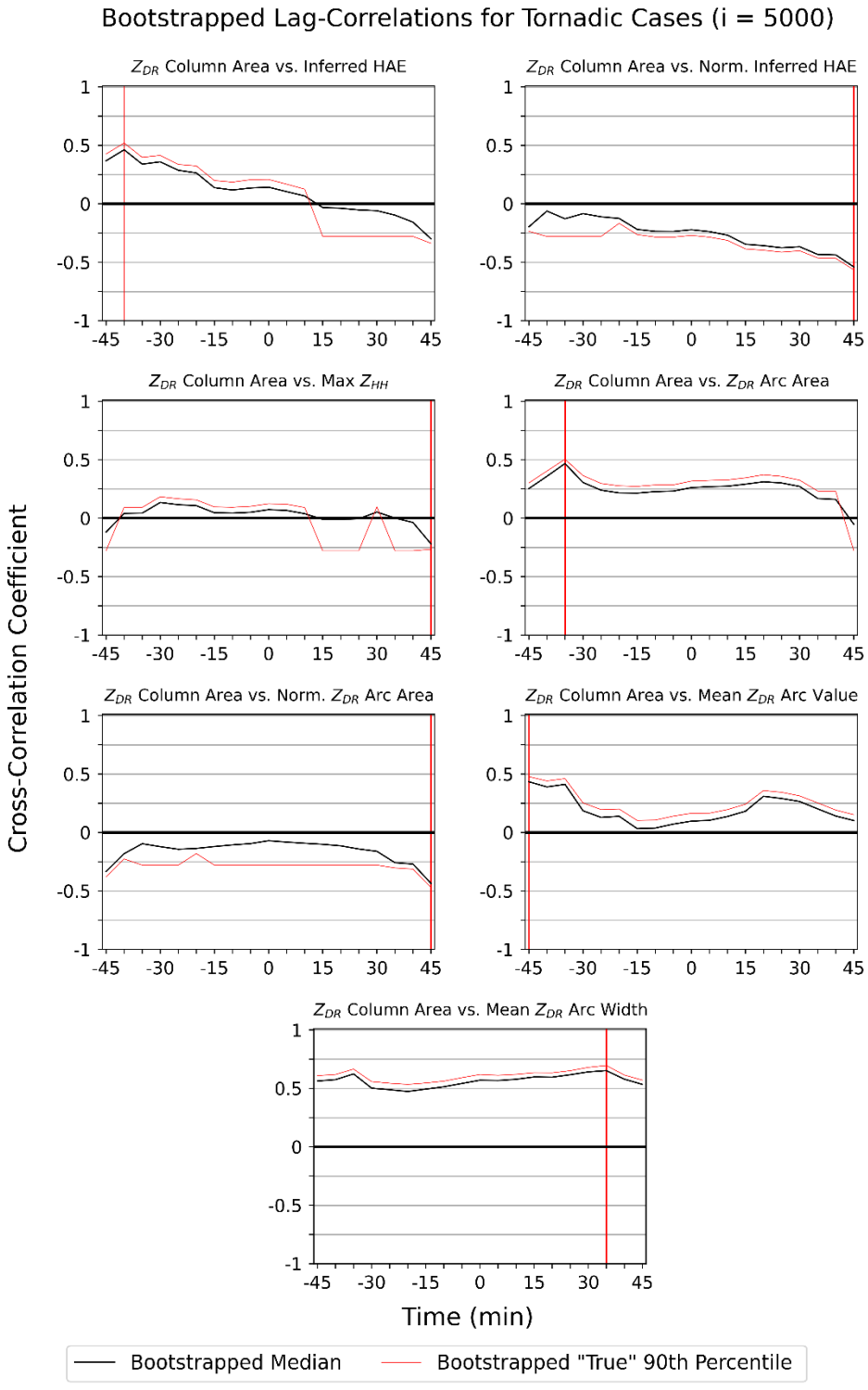

Figure 4.17: Correlograms of the bootstrapped median values (black line) and "true" 90th percentile (faint red line) for the tornadic sample of metric comparisons utilizing the Z_{DR} column area metric. The lag at which the bootstrapped median correlation value is greatest (*in magnitude*) is denoted by a vertical red line.

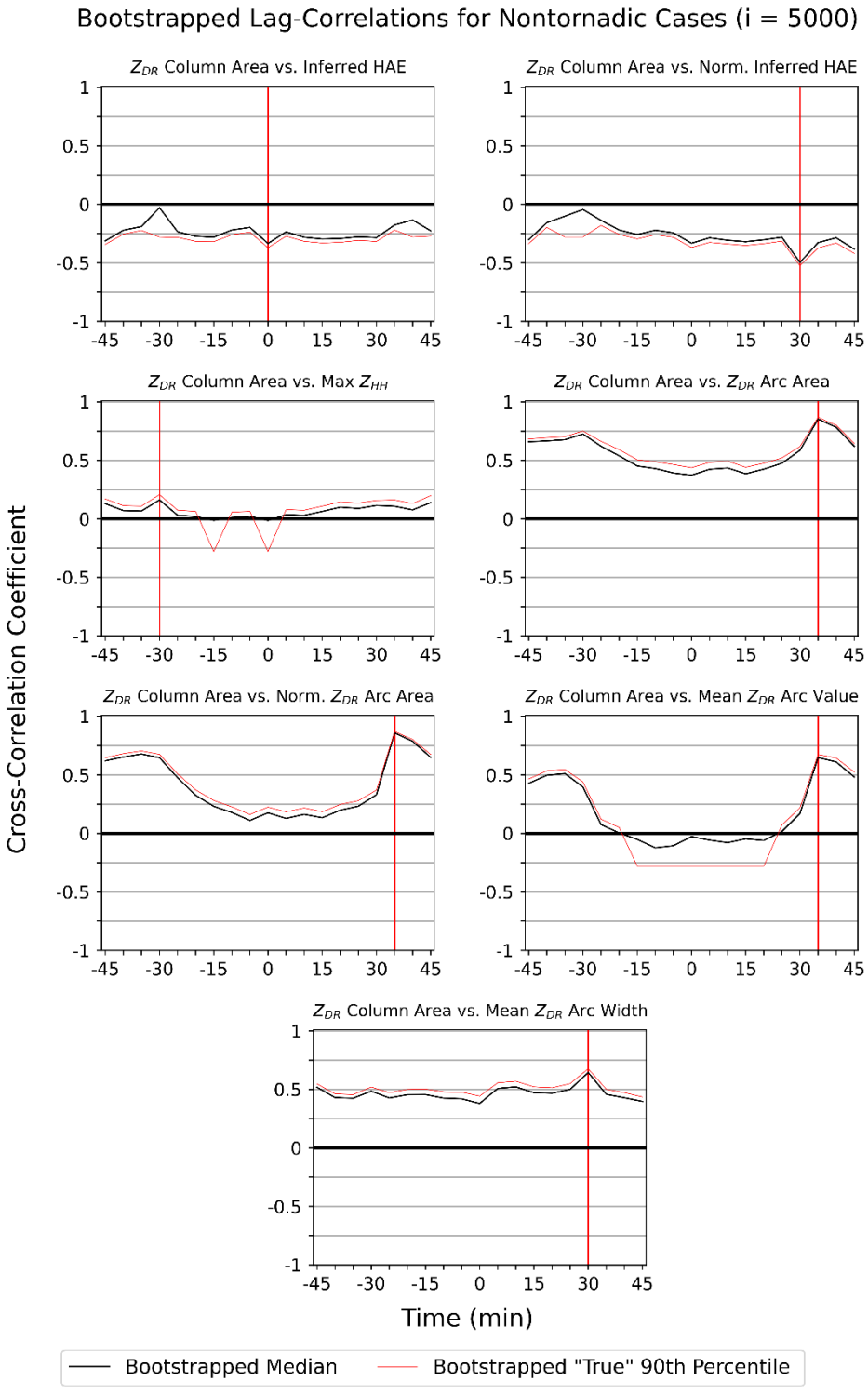

Figure 4.18: As in Fig. 4.17 for the nontornadic sample bootstrapping results utilizing the Z_{DR} column area metric.

Table 4.8: A summary of Fig. 4.15 and 4.16 displaying the maximum cross-correlation values (*in magnitude*) for the Z_{DR} column area metric comparisons from all available sample cases, with the corresponding lag at which it occurred. Maximum correlation values determined to be statistically significant (p-value < 0.05) are denoted by *.

Z_{DR} Column Area

Tornadic			Nontornadic		
Metric Comparison	Max R-Value	Corresponding Lag (min)	Metric Comparison	Max R-Value	Corresponding Lag (min)
Inferred HAE	0.46*	–40	Inferred HAE	–0.31	0
Norm. Inferred HAE	–0.54*	45	Norm. Inferred HAE	–0.50*	30
Max Storm Core Z_{HH}	–0.22	45	Max Storm Core Z_{HH}	0.16	–30
Z_{DR} Arc Area	0.46*	–35	Z_{DR} Arc Area	0.85*	35
Norm. Z_{DR} Arc Area	–0.44*	45	Norm. Z_{DR} Arc Area	0.86*	35
Mean Z_{DR} Arc Value	0.43*	–45	Mean Z_{DR} Arc Value	0.65*	35
Mean Z_{DR} Arc Width	0.65*	35	Mean Z_{DR} Arc Width	0.65*	30

maximum correlation values at a positive lag. The normalized Z_{DR} arc area metric comparison was maximized at a lag of 45 minutes (R~ –0.44), indicative of an increase in the Z_{DR} column area following a decrease in the normalized Z_{DR} arc area, nearly the opposite of the results of raw Z_{DR} arc area metric comparison. The metric comparison between the Z_{DR} column area and mean Z_{DR} arc width exhibited a positive peak correlation value after a positive lag of 35 minutes (R~0.65), indicating that an increase in the magnitude of the Z_{DR} column area tended to follow an increase in the mean Z_{DR} arc width.

Among the nontornadic sample scans (Fig. 4.16 and 4.18), all three inferred low-level hail fallout metrics did not exhibit a consistent pattern amongst each other. The inferred HAE metric comparison exhibited a peak correlation value at a negative lag of 45 minutes (R~ –0.31, $p > 0.05$), indicating an increase in the magnitude of the Z_{DR} column area tended to precede a decrease in the inferred HAE by 45 minutes.

Conversely, the normalized inferred HAE was maximized at 30 minutes of positive lag (R~ –0.50, $p < 0.05$), indicating that an increase in Z_{DR} column area tended to follow a decrease in normalized inferred HAE. Lastly, the max storm core Z_{HH} metric comparison exhibited a peak correlation value at 30 minutes of negative lag (R~0.16, $p > 0.05$), indicating an increase in the Z_{DR} column area tended to precede an increase in the max storm core Z_{HH} value by 30 minutes.

Regarding the Z_{DR} arc-based metrics, consistency was observed among each of the metric comparisons where peak correlation values were observed between 30 to 35 minutes of positive lag. The Z_{DR} arc area (R~0.85, $p < 0.05$), normalized Z_{DR} arc area (R~0.86, $p < 0.05$), and mean Z_{DR} arc value (R~0.65, $p < 0.05$) metric comparisons were all maximized at positive lag values of 35 minutes. This indicated an increase in the Z_{DR} column area tended to follow an increase in the magnitude of these three metrics by 35 minutes. The mean Z_{DR} arc width metric comparison was maximized at a positive lag of 30 minutes (R~ –0.65, $p < 0.05$), suggesting that an increase the magnitude of the Z_{DR} column area also tended to follow an increase in the magnitude of the mean Z_{DR} arc width by 30 minutes.

ii. Normalized Z_{DR} Column Area Metric Comparisons

The results of the observed data correlograms for total samples of tornadic and nontornadic scans among comparisons using the normalized Z_{DR} column area metric for the updraft proxy are shown in Fig. 4.19 and 4.20. The resulting correlograms featuring the bootstrapped median values and 90th percentile are shown in Fig. 4.21 and 4.22. Additionally, a summary of the correlograms featured above are presented in Table 4.9.

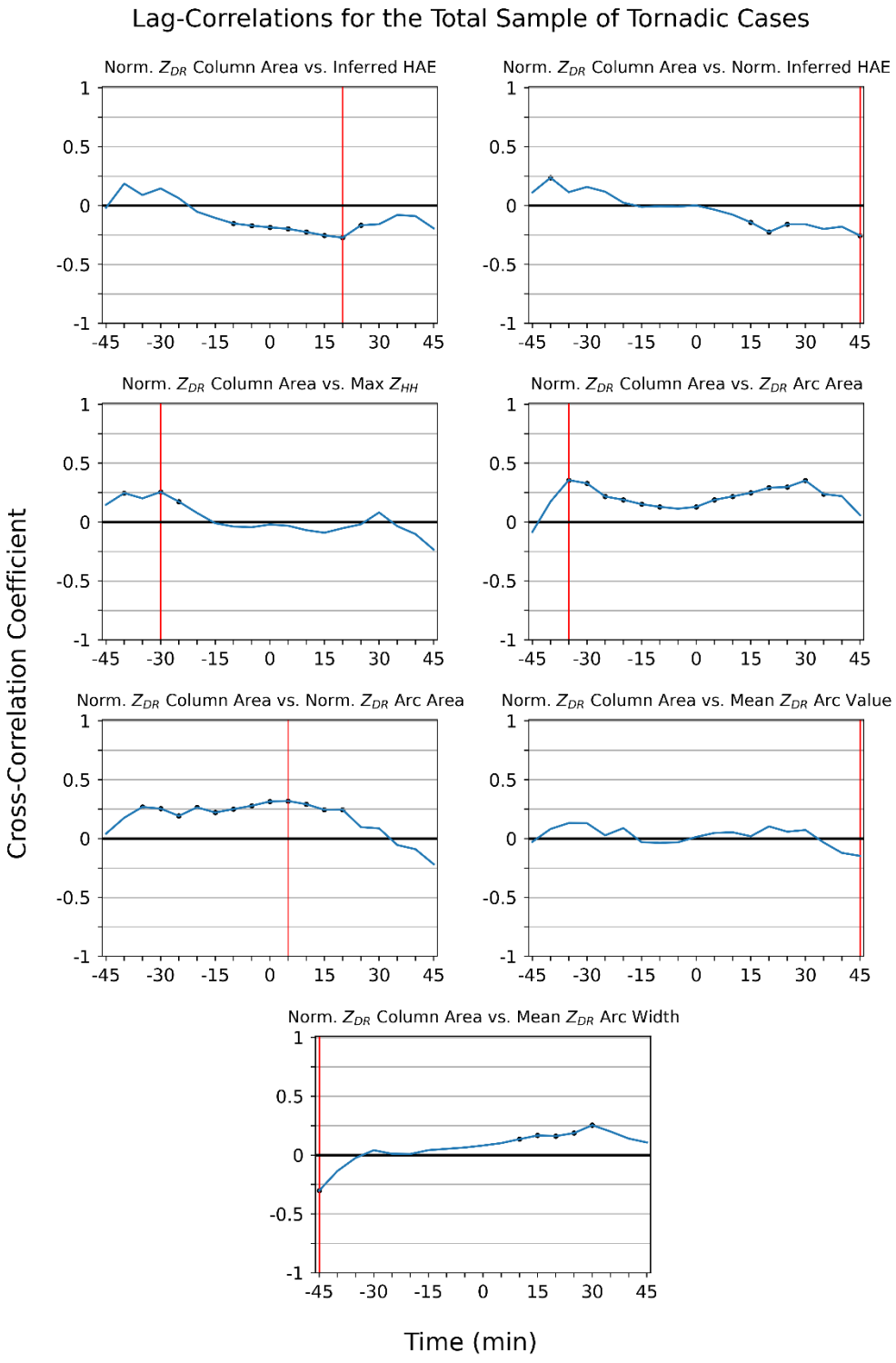

Fig 4.19: Correlograms for the normalized Z_{DR} column area metric comparisons of all available sample scans from tornadic storms. Correlation values determined to be statistically significant ($p < 0.05$) are denoted by a black dot and the red vertical line is the time at which the maximum correlation value (*in magnitude*) is achieved.

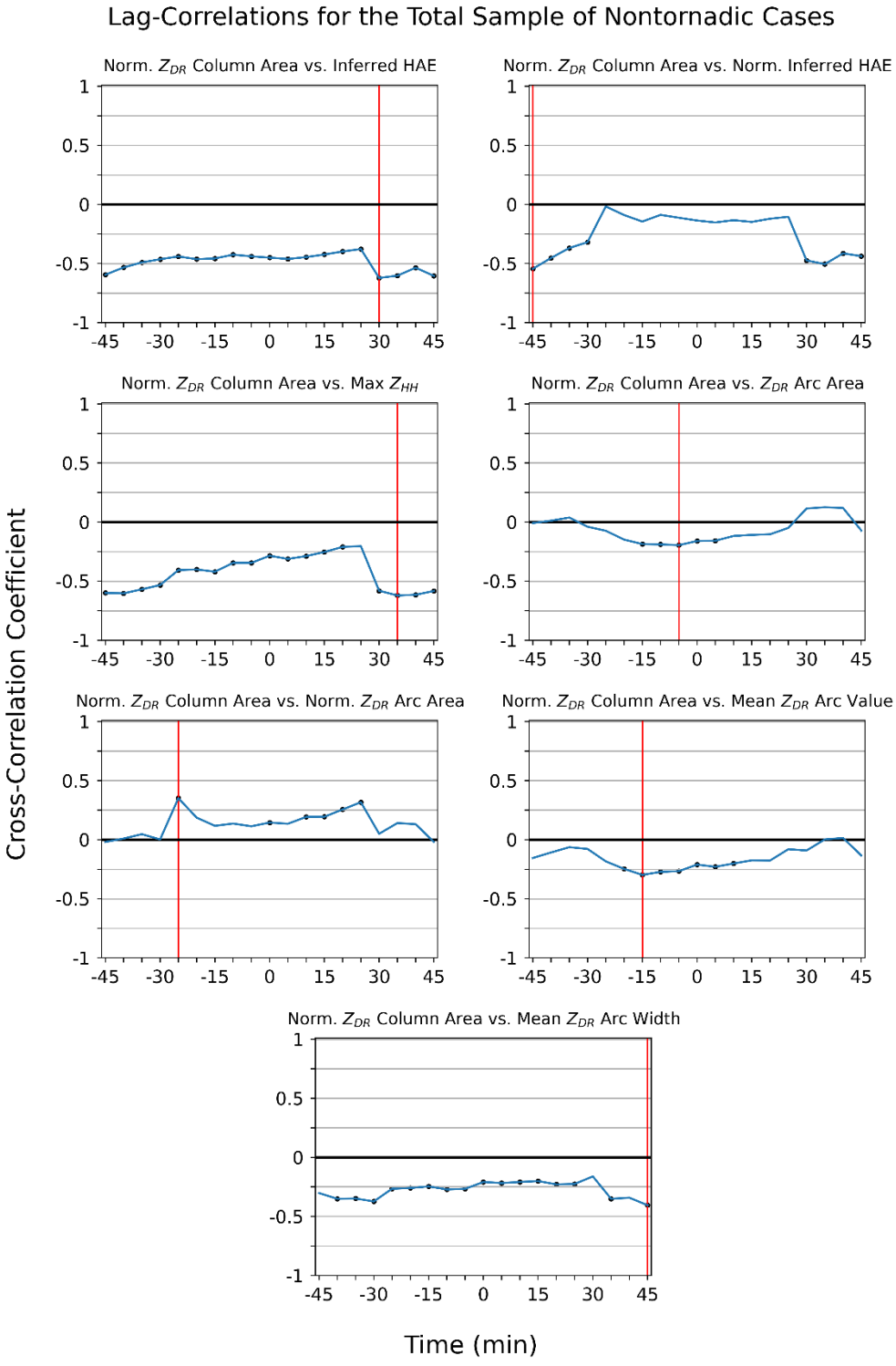

Figure 4.20: As in Fig. 4.19 for all available sample scans from nontornadic storms.

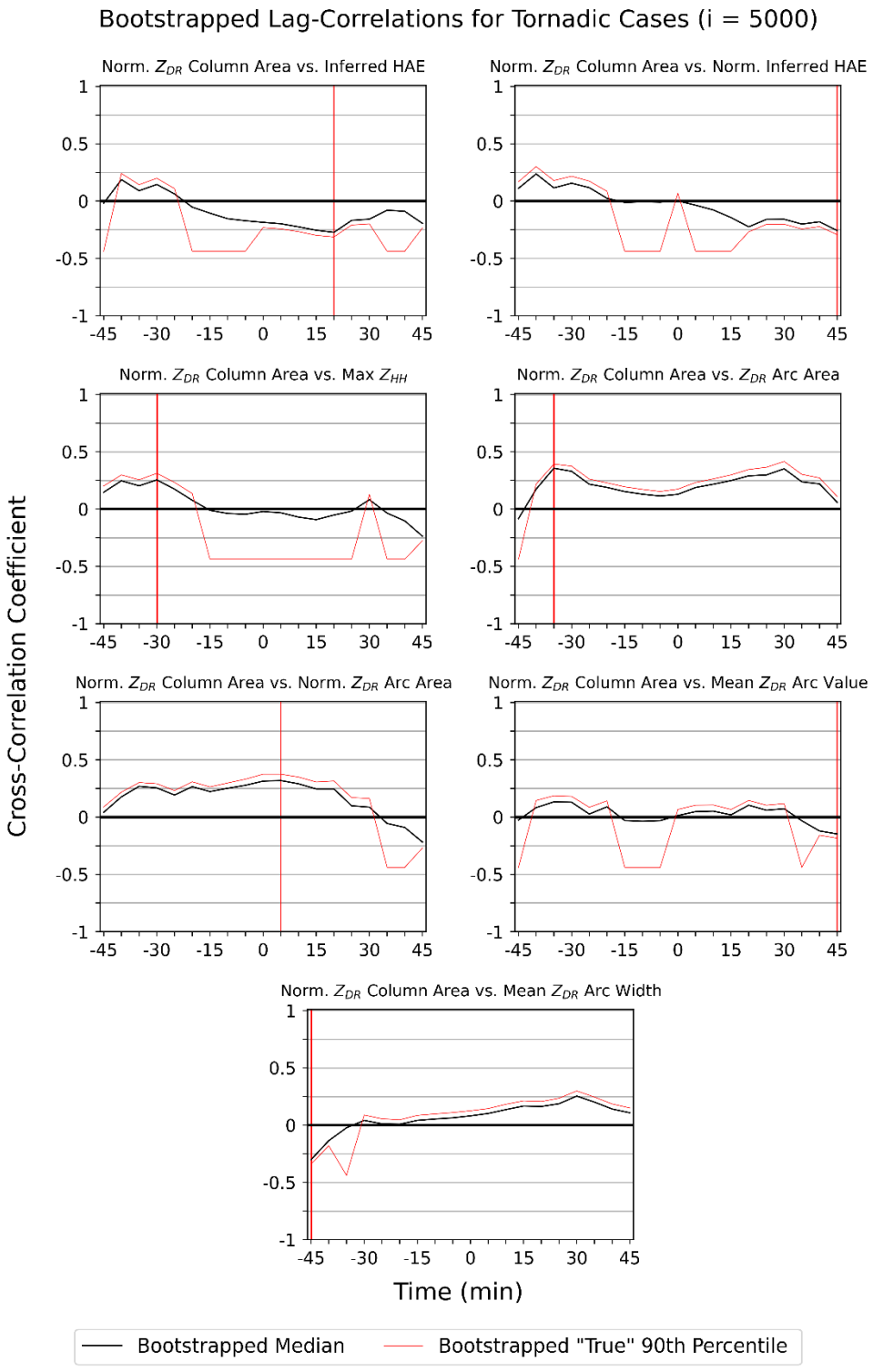

Figure 4.21: Correlograms of the bootstrapped median values (black line) and "true" 90th percentile (faint red line) for the tornadic sample of metric comparisons utilizing the normalized Z_{DR} column area metric. The lag at which the bootstrapped median correlation value is greatest (*in magnitude*) is denoted by a vertical red line.

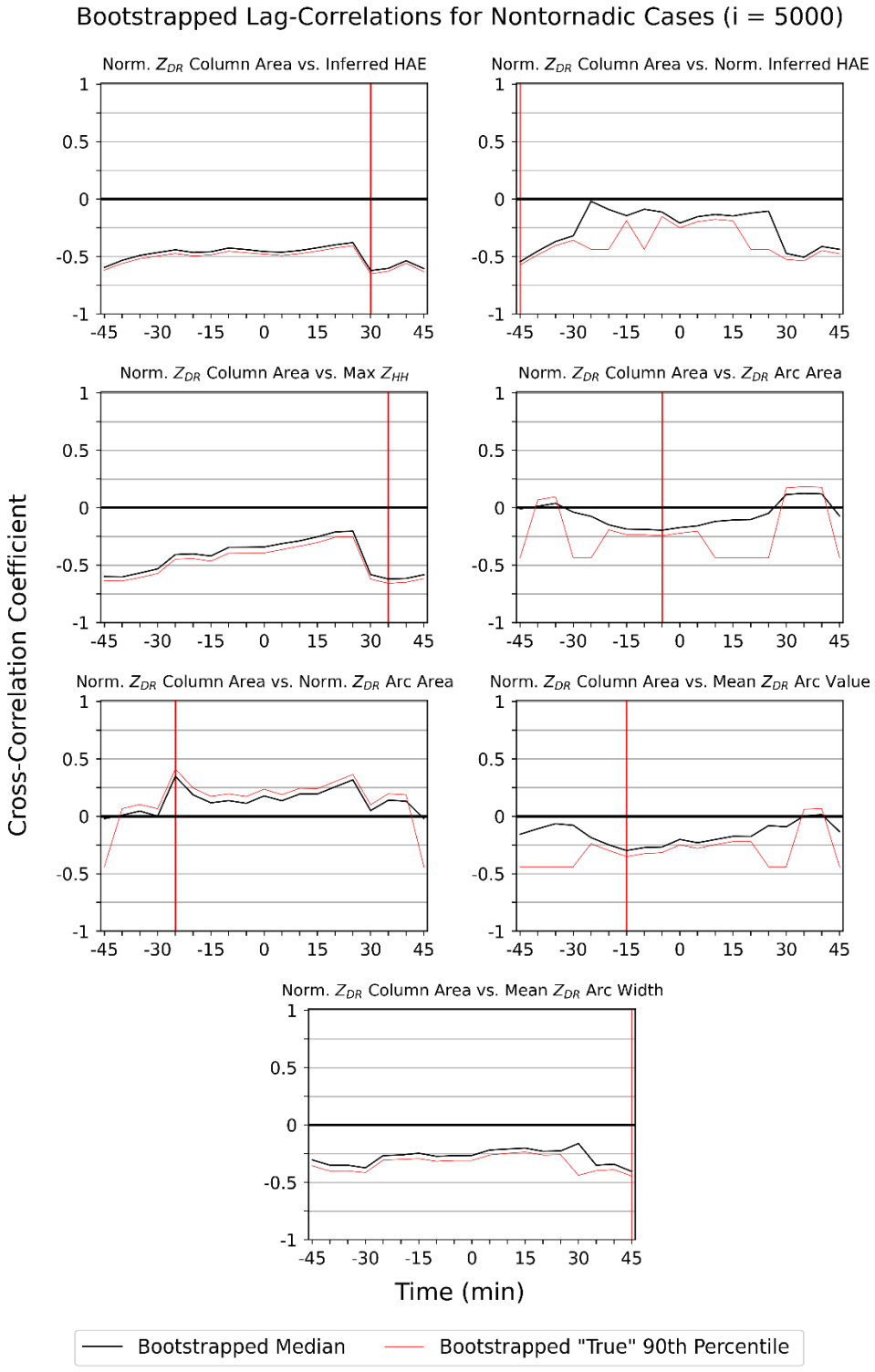

Figure 4.22: As in Fig. 4.21 for the nontornadic sample bootstrapping results utilizing the normalized Z_{DR} column area metric.

Table 4.9: A summary of Fig. 4.19 and 4.20 displaying the maximum cross-correlation values (*in magnitude*) for the normalized Z_{DR} column area metric comparisons from all available sample cases, with the corresponding lag at which it occurred. Maximum correlation values determined to be statistically significant (p-value < 0.05) are denoted by *.

Norm Z_{DR} Column Area

Tornadic			Nontornadic		
Metric Comparison	Max R-Value	Corresponding Lag (min)	Metric Comparison	Max R-Value	Corresponding Lag (min)
Inferred HAE	–0.27*	20	Inferred HAE	–0.62*	30
Norm. Inferred HAE	–0.26*	45	Norm. Inferred HAE	–0.55*	–45
Max Storm Core Z_{HH}	0.26*	–30	Max Storm Core Z_{HH}	–0.62*	35
Z_{DR} Arc Area	0.36*	–35	Z_{DR} Arc Area	–0.20*	–5
Norm. Z_{DR} Arc Area	0.32*	5	Norm. Z_{DR} Arc Area	0.35*	–25
Mean Z_{DR} Arc Value	–0.15	45	Mean Z_{DR} Arc Value	–0.30*	–15
Mean Z_{DR} Arc Width	–0.30*	–45	Mean Z_{DR} Arc Width	–0.41*	45

Within the sample of tornadic scans (Fig. 4.19 and 4.21), the low-level inferred hail fallout metric comparisons exhibited similar correlograms, with varying results. The inferred HAE metric comparison exhibited a peak negative correlation value at a positive lag of 20 minutes (R~ –0.27, $p < 0.05$), indicating an increase in the normalized Z_{DR} column area tended to follow a decrease in the magnitude of the inferred HAE. Similarly, the normalized inferred HAE metric comparison was maximized at a positive lag of 45 minutes (R~ –0.26, $p < 0.05$), and similar to the inferred HAE metric comparison, an increase in the normalized Z_{DR} column area tended to follow a decrease in the normalized inferred HAE by 45 minutes. Lastly, the max storm core Z_{HH} value metric comparison revealed results opposite to the inferred HAE metric comparisons. The correlogram exhibited a peak correlation value at 30 minutes of negative lag (R~0.26, $p < 0.05$), suggesting an increase in the normalized Z_{DR} column area tended to precede an increase in the max storm core Z_{HH} value by 30 minutes.

Regarding the Z_{DR} arc-based metric comparisons, varying results were noted among the four metric comparisons. The Z_{DR} arc area and mean Z_{DR} arc width metric comparisons were found to be maximized at negative lags of 35 minutes and 45 minutes, respectively, where increases in the normalized Z_{DR} column area tended to precede an increase in the Z_{DR} arc area (R~0.36, $p < 0.05$), and follow a decrease in the magnitude of the mean Z_{DR} arc width (R~ –0.26, $p < 0.05$). The normalized Z_{DR} arc area and mean Z_{DR} arc value metric comparisons were found to be maximized at positive lags, where an increase in the normalized Z_{DR} column area tended to follow an increase in the normalized Z_{DR} arc area (R~0.32, $p < 0.05$) after 5 minutes of lag, and also followed a decrease in the mean Z_{DR} arc value (R~ –0.15, $p > 0.05$) after 45 minutes of lag.

The results of the nontornadic sample scan metric comparisons are shown in Fig. 4.20 and 4.22. Across the low-level inferred hail fallout metrics, two of three metric comparisons (inferred HAE and max Z_{HH}) exhibited a peak correlation value at a positive lag value, indicating that increases in the magnitude of the normalized Z_{DR} column area tend to follow decreases in the inferred HAE (R~ –0.62, $p < 0.05$) and max storm core Z_{HH} (R~ –0.62, $p < 0.05$). Conversely, the normalized inferred HAE comparison exhibited a peak correlation value at a negative lag of 45 minutes (R~ –0.55, $p < 0.05$), indicating an increase in the magnitude of the normalized Z_{DR} column area tended to precede a decrease in the normalized inferred HAE by 45 minutes.

Among the four Z_{DR} arc-based metrics, three of four metrics exhibited a peak correlation value at a negative lag, including the Z_{DR} arc area, normalized Z_{DR} arc area, and mean Z_{DR} arc value metrics. Both Z_{DR} arc area (R~ –0.20, $p < 0.05$) and mean Z_{DR} arc value (R~ –0.30, $p < 0.05$) metric comparisons indicated that increases in the normalized

Z_{DR} column area metric tended to precede decreases in these metrics by 5 minutes and 15 minutes, respectively. Conversely to the Z_{DR} arc area metric comparison, the magnitude of the normalized Z_{DR} arc area tended to increase following an increase in the normalized Z_{DR} column area (R~0.35, $p < 0.05$) by 25 minutes. Lastly, the metric comparison against the mean Z_{DR} arc width exhibited a peak correlation value at a positive lag of 45 minutes (R~ –0.41, $p < 0.05$), indicating that an increase in the normalized Z_{DR} column area tended to follow a decrease in the mean Z_{DR} arc width.

iii. Z_{DR} Column Depth Metric Comparisons

The results of the observed data correlograms for total samples of tornadic and nontornadic scans among comparisons which used the Z_{DR} column depth metric as an updraft proxy are shown in Fig. 4.23 and 4.24. The resulting correlograms featuring the bootstrapped median values and 90th percentile are shown in Fig. 4.25 and 4.26. Additionally, a summary of the correlograms featured for this set of comparisons is presented in Table 4.10.

Within the sample of tornadic storms (Fig. 4.23 and 4.25), the three low-level inferred hail fallout metric comparisons did not exhibit consistency. The inferred HAE metric comparison produced a positive peak correlation value (R~0.27, $p < 0.05$) at a negative lag of 45 minutes. The normalized inferred HAE metric comparison produced an opposite result, exhibiting a negative peak correlation value (R~ –0.37, $p < 0.05$) at a positive lag of 45 minutes. It is worth noting the correlograms between these two comparisons were very similar, with varying magnitudes contributing to different peak correlation values. Based on the results, it was shown that an increase in Z_{DR} column

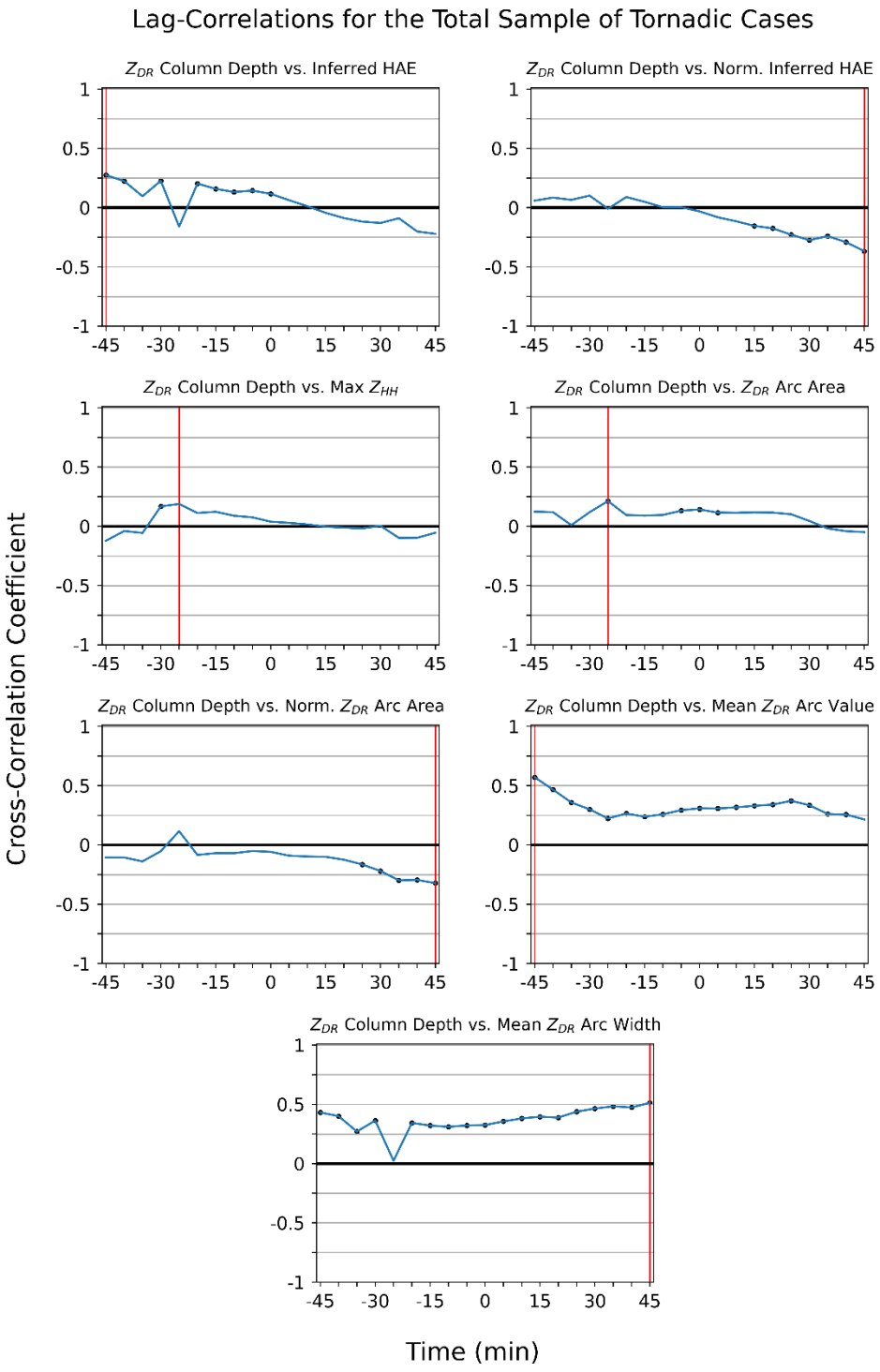

Figure 4.23: Correlograms for the Z_{DR} column depth metric comparisons of all available sample scans from tornadic storms. Correlation values determined to be statistically significant ($p < 0.05$) are denoted by a black dot and the red vertical line is the time at which the maximum correlation value (*in magnitude*) is achieved.

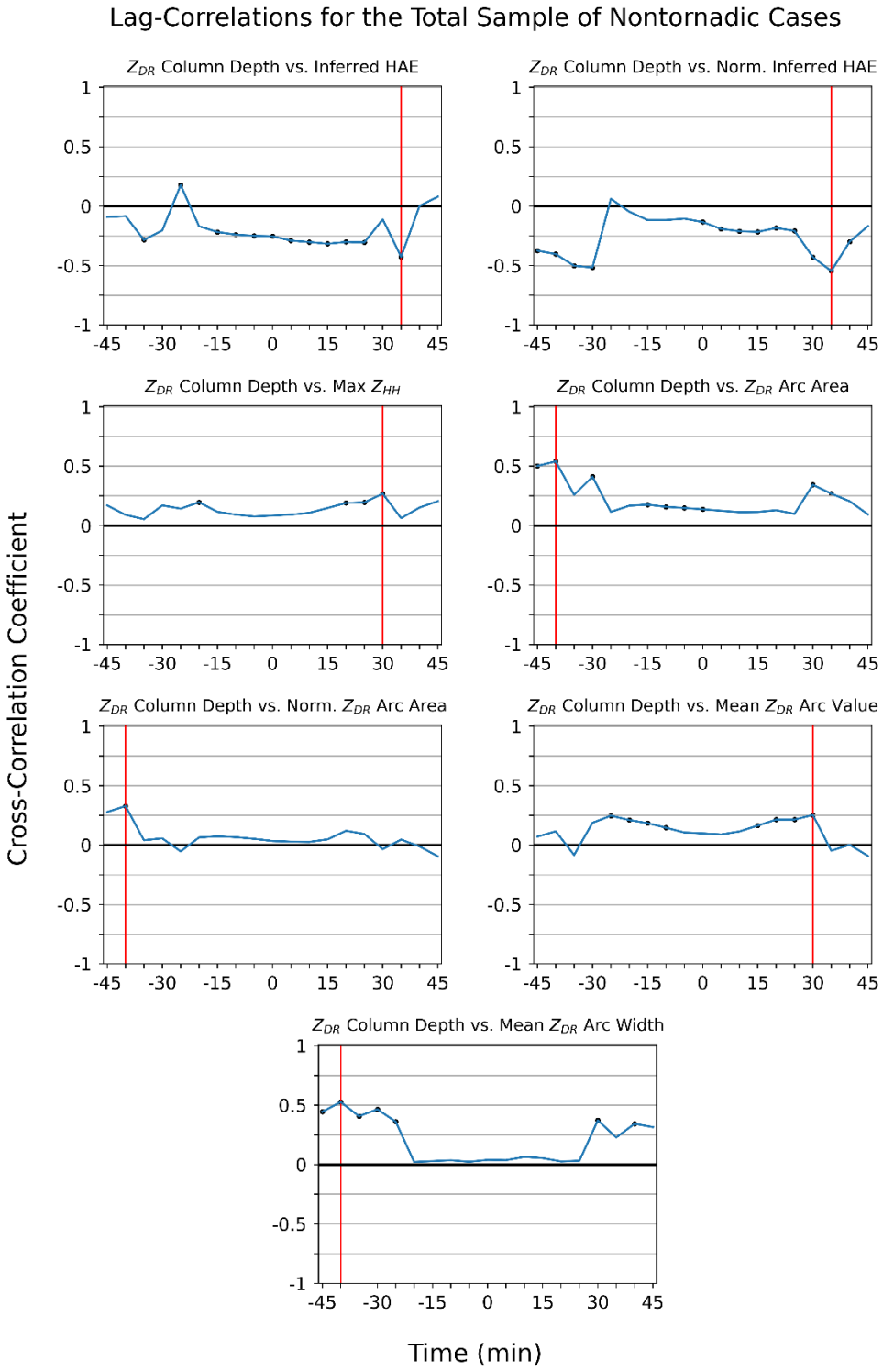

Figure 4.24: As in Fig. 4.23 for all available sample scans from nontornadic storms

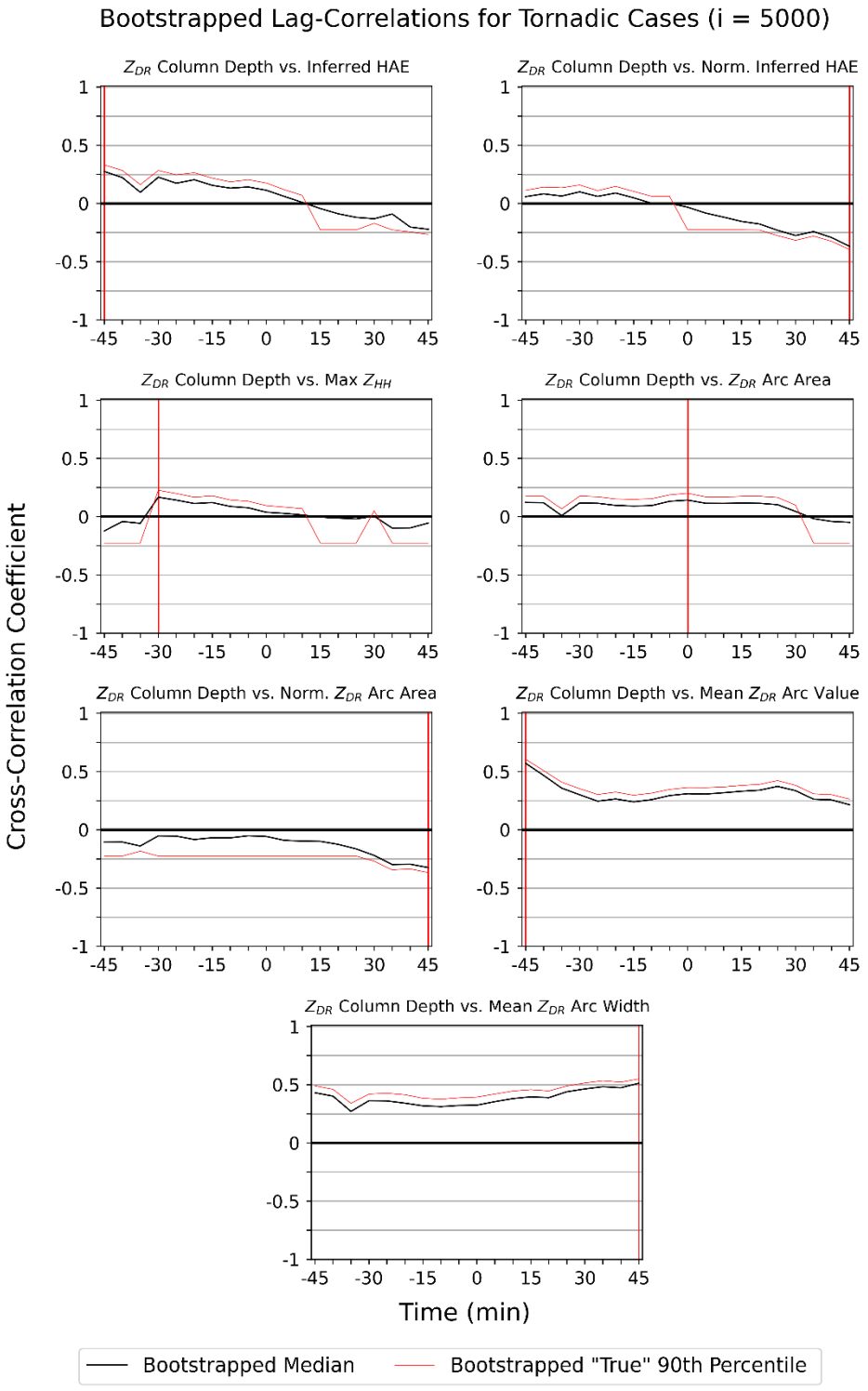

Figure 4.25: Correlograms of the bootstrapped median values (black line) and "true" 90th percentile (faint red line) for the tornadic sample of metric comparisons utilizing the Z_{DR} column depth metric. The lag at which the bootstrapped median correlation value is greatest (*in magnitude*) is denoted by a vertical red line.

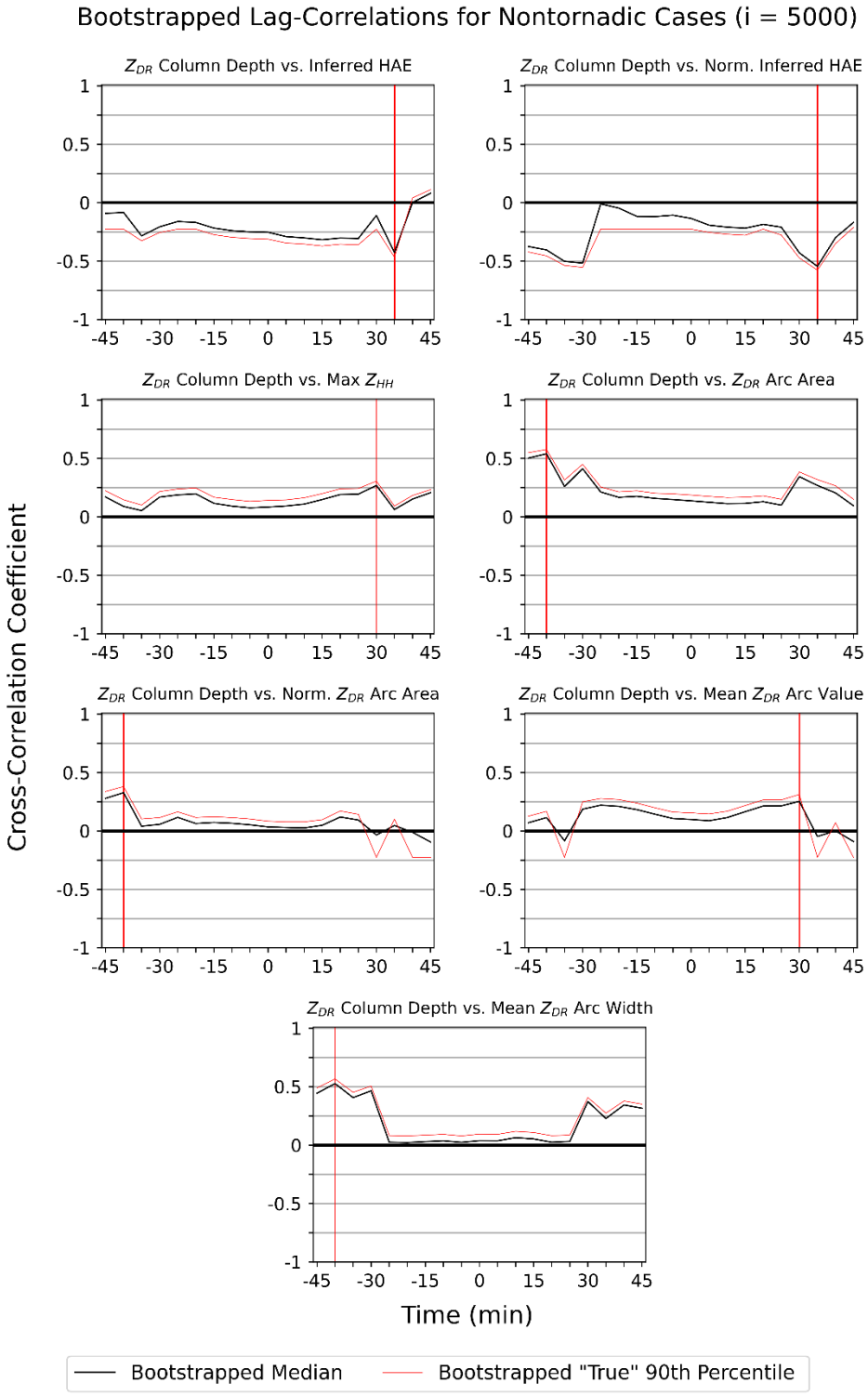

Figure 4.26: As in Fig. 4.25 for the nontornadic sample bootstrapping results utilizing the Z_{DR} column depth metric.

Table 4.10: A summary of Fig. 4.23 and 4.24 displaying the maximum cross-correlation values (*in magnitude*) for the Z_{DR} column depth metric comparisons from all available sample cases, with the corresponding lag at which it occurred. Maximum correlation values determined to be statistically significant (p-value < 0.05) are denoted by *.

Z_{DR} Column Depth

Tornadic			Nontornadic		
Metric Comparison	Max R-Value	Corresponding Lag (min)	Metric Comparison	Max R-Value	Corresponding Lag (min)
Inferred HAE	0.27*	–45	Inferred HAE	–0.43*	35
Norm. Inferred HAE	–0.37*	45	Norm. Inferred HAE	–0.55*	35
Max Storm Core Z_{HH}	0.19	–25	Max Storm Core Z_{HH}	0.27*	30
Z_{DR} Arc Area	0.21*	–25	Z_{DR} Arc Area	0.54*	–40
Norm. Z_{DR} Arc Area	–0.32*	45	Norm. Z_{DR} Arc Area	0.33*	–40
Mean Z_{DR} Arc Value	0.57*	–45	Mean Z_{DR} Arc Value	0.25*	30
Mean Z_{DR} Arc Width	0.51*	45	Mean Z_{DR} Arc Width	0.53*	–40

depth tended to precede an increase in the inferred HAE by 45 minutes, whereas increases in Z_{DR} column depth tended to follow a decrease in the normalized inferred HAE by 45 minutes. Regarding the max Z_{HH} value metric comparison, a peak correlation value (R~0.19, $p > 0.05$) was observed at a negative lag of 25 minutes. Despite not exhibiting statistical significance, this indicated that an increase in the Z_{DR} column depth tended to precede an increase in the max Z_{HH} value by 25 minutes.

The Z_{DR} arc-based metric comparisons produced varying results as well. The Z_{DR} arc area comparison exhibited a peak positive correlation value at a negative lag of 25 minutes (R~0.21, $p < 0.05$). The mean Z_{DR} arc value metric comparison exhibited a peak correlation value (R~0.57, $p < 0.05$) at a negative lag of 45 minutes. This indicated increases in the Z_{DR} column depth tended to precede increases in the Z_{DR} arc area and mean arc value by 25 minutes and 45 minutes, respectively. Comparatively, the normalized Z_{DR} arc area (R~ –0.32, $p < 0.05$) and mean Z_{DR} arc width (R~0.51, $p < 0.05$)

metric comparisons were both maximized at a positive lag of 45 minutes. This would indicate that an increase in Z_{DR} column depth tended to follow a decrease in the normalized Z_{DR} arc area, and an increase in the mean Z_{DR} arc width by 45 minutes.

Within the sample of nontornadic scans (Fig. 4.24 and 4.26), strong consistency was observed among the low-level inferred hail fallout metrics. Both the inferred HAE (R~ –0.43, $p < 0.05$) and normalized inferred HAE (R~ –0.55, $p < 0.05$) exhibited similar correlograms, with peak correlation values at a positive lag of 35 minutes. The max Z_{HH} metric comparison exhibited a positive peak correlation value (R~0.27, $p < 0.05$) at a positive lag of 30 minutes. Across the three metric comparisons, it was shown that an increase in Z_{DR} column depth generally followed a decrease in both the inferred HAE and normalized inferred HAE by 35 minutes, and preceded an increase in the max storm core Z_{HH} value by 30 minutes.

The Z_{DR} arc-based metric comparisons exhibited consistency amongst each other, where the Z_{DR} arc area (R~0.54, $p < 0.05$), normalized Z_{DR} arc area (R~0.33, $p < 0.05$), and mean Z_{DR} arc width (R~0.53, $p < 0.05$) metric comparisons were shown to be maximized at a negative lag of 40 minutes. This indicated increases in the Z_{DR} column depth tended to precede an increase in the magnitude of all three of the metrics by 40 minutes. Lastly, the mean Z_{DR} arc value metric comparison exhibited a peak correlation value at a positive lag of 30 minutes (R~0.25, $p < 0.05$), indicating a decrease in the mean Z_{DR} arc value tended to precede an increase in the Z_{DR} column depth by 30 minutes.

4e. Metric Comparison Discussions

Correlation values were calculated for the metric comparisons listed throughout

Section 4d among both tornadic and nontornadic samples, with a bootstrapping method applied to the data to create a more statistically meaningful sample size from which conclusions about each of the comparisons could be inferred. A subsection for each polarimetric signature comparison previously outlined and a discussion on the associations of the metric comparisons to storm-scale processes will follow.

i. Polarimetrically Inferred Hail Areal Extent and Maximum Storm Core Reflectivity

This section will encompass the results of the inferred HAE, normalized inferred HAE, and maximum storm core reflectivity metric comparisons. Discussions will include a brief recap of the correlograms for each metric comparison along with further analysis into potential associations and similarities to known conceptual models and observations. The discussions have also been grouped into tornadic and nontornadic sections, as each sample tended to exhibit unique patterns and results.

a. Tornadic Sample Discussion

Among the inferred HAE metric comparisons, two of three updraft proxy comparisons (Z_{DR} column area and column depth) yielded significant positive peak correlation values at negative lags of 45 and 40 minutes, respectively, where the Z_{DR} column area metric comparison yielded the largest magnitude correlation value (R~0.46). The normalized Z_{DR} column area metric comparison was found to be opposite to the other two updraft proxies, with a negative peak correlation value at a positive lag of 20 minutes. The majority pattern for the inferred HAE metric comparison suggests

substantial lead time of 40 to 45 minutes between an increase in the magnitude of either the Z_{DR} column area or Z_{DR} column depth, and the latter increase in magnitude of the inferred HAE metric, where an increase in the magnitude of the inferred HAE metric is interpreted as increasing hail fallout.

For the normalized inferred HAE metric comparison among tornadic sample scans, a consistent pattern was observed across all three polarimetric updraft proxy metric comparisons. An inverse relationship was determined with significant peak negative correlation values at a positive lag of 45 minutes, where the Z_{DR} column area comparison produced the greatest magnitude correlation value (R~ –0.54). This is indicative of a decrease in the normalized inferred HAE tending to follow an increase in magnitude of the Z_{DR} column metrics by 45 minutes, and is in contrast to the tornadic sample of the inferred HAE metric comparisons. However, all three updraft proxy comparisons produced a similar result, and may be indicative of a leniency towards an association between the polarimetrically inferred updraft proxy metrics and the normalized inferred HAE metric. This is possibly owing to the inclusion of storm area in the normalized inferred HAE metric, which is intended to create a more uniform comparison between samples.

Lastly, for the max storm core reflectivity metric comparisons, two of three updraft proxy comparisons yielded a positive peak median correlation value at negative lags of 25 to 30 minutes, e.g., the normalized Z_{DR} column area ($p < 0.05$) and Z_{DR} column depth ($p > 0.05$) comparisons. Conversely, the Z_{DR} column area metric comparison yielded a negative peak median correlation value at a positive lag value. The results presented for this metric comparison are also consistent with the results from the inferred

HAE metric comparisons, where an increase in the magnitude of a Z_{DR} column-based metric (e.g., the normalized Z_{DR} column area or column depth for the max storm core reflectivity comparison) tended to precede an increase in the magnitude of the base-scan maximum storm core reflectivity value.

The results presented are supportive of tornadic supercell cyclic processes, particularly for the relationships demonstrated between the inferred HAE and max storm core reflectivity. Observations within this study remain consistent with prior studies (e.g., Picca et al. 2010; Kumjian et al. 2014; Kuster et al. 2019, 2020), where both the work of Kuster and the results presented can be assimilated into current conceptual models. It is noted that the results of the normalized inferred HAE metric comparisons were opposite of the other two hail fallout metrics, and likely needs further investigation regarding its utility. From Kuster et al. (2019) and (2020), Z_{DR} columns were shown to increase in areal extent and/or depth around five to nine minutes prior to the development and/or increase in the size of a –20˚C reflectivity core. This is consistent with the updraft-relative timeline, where following the initial increase in magnitude of a Z_{DR} column metric, the base-scan max reflectivity value tended to increase 25 to 30 minutes later, and inferred HAE tended to increase 40 to 45 minutes later. This pattern is suggested to be representative of cyclic tornadic mesocyclones and the associated periodic increases in the inferred hail area.

It is not lost on the author that max storm core reflectivity is not a true polarimetric variable since reflectivity (Z_{HH} or Z_{VV}) only requires a single polarization of transmitted energy. However, the consistency that has been observed within the tornadic sample among inferred hail fallout metrics is a promising signal, and suggests that

variability of inferred HAE and max storm core reflectivity value could be used in conjunction with radar interrogation of Z_{DR} columns, particularly since lower number concentrations of larger hail falling under or along the periphery of an updraft may be associated with only modest Z_{HH} values (Snyder et al. 2015).

It is also noted that an important differentiating factor among prior work and the results within this study remains the temporal and spatial resolution of data. Rapid-update radar data and numerical simulations were shown to provide a stronger signal in this presumed association between polarimetrically inferred updraft intensity and hail area (e.g., Kuster et al. 2019, 2020), while the use of operational WSR-88D volumetric data likely hindered the ability to capture sufficient evolution of the polarimetric signatures. Despite this caveat, the results presented are still consistent with prior work and furthers the argument for continuous investigation of this polarimetric relationship via the use of operational volumetric radar data.

b. Nontornadic Sample Discussion

The inferred HAE metric comparisons against the normalized Z_{DR} column area and Z_{DR} column depth produced consistent results relative to each other, yielding significant negative peak correlation values at positive lags of 20 and 35 minutes, respectively. This suggests contrasting processes and associations compared to tornadic sample scans with regard to the inferred HAE metric. The results presented suggest that an increase in the magnitude of either the normalized Z_{DR} column area or Z_{DR} column depth tended to follow a decrease in the magnitude of the inferred HAE metric by 20 to

35 minutes, respectively, where the normalized Z_{DR} column area comparison produced the largest magnitude correlation value (R~ –0.62).

For the normalized inferred HAE metric comparisons, observations remained consistent with the results from the raw inferred HAE metric comparison, with all three comparisons yielding a significant peak median correlation value less than zero. Two of three comparisons produced a peak median correlation value at a positive lag, including the Z_{DR} column area (R~ –0.50 at 30 minutes) and Z_{DR} column depth (R~ –0.55 at 35 minutes) metric comparisons. However, the normalized Z_{DR} column area metric comparison had a peak median correlation value (R~ –0.55) at 45 minutes of negative lag. The observed pattern among two of three updraft proxy comparisons suggests an inverse relationship where an increase in the magnitude of either the Z_{DR} column area or column depth tended to follow a decrease in the magnitude of the normalized inferred HAE by 30 to 35 minutes. This is also consistent with the results of the nontornadic sample for the inferred HAE metric comparisons, with a difference of up to 10 additional minutes of lag in the normalized inferred HAE metric comparisons.

Lastly, among the max storm core reflectivity value, inconsistent results were observed across the three updraft proxy metric comparisons. The normalized Z_{DR} column area and Z_{DR} column depth metric comparisons both exhibited significant peak median correlation values at 30 to 35 minutes of positive lag, but with opposite signs of the peak correlation value, where the normalized Z_{DR} column area metric comparison exhibited the strongest magnitude correlation value (R~ –0.62). Despite the inconsistent results within this metric comparison, the trend associated with the strongest magnitude correlation value was consistent with the results of both the inferred HAE and normalized inferred

HAE metric comparisons, e.g., a peak median correlation value less than zero at a positive lag of 30 to 35 minutes, suggesting that an increase in the magnitude of the normalized Z_{DR} column area tended to follow a decrease in magnitude of the max storm core reflectivity value after 35 minutes.

The results presented may be representative of cyclical processes within the nontornadic sample. Cyclicity of polarimetric signatures was previously noted by KR08, and within this study where nontornadic samples tended to exhibit a greater variability in the magnitude of inferred HAE signatures. When the magnitude of the inferred HAE metric and the max storm core reflectivity value decrease prior to an increase in the magnitude of a Z_{DR} column metric, this may suggest that initially following the descent of a reflectivity or inferred hail core (and subsequent decrease in the base-scan inferred hail area metrics), a weakening of the updraft may occur at first, possibly in conjunction with the occlusion of the low-level mesocyclone (pending full volumetric radar interrogation). However, with inferred increased hail and/or precipitation, baroclinically generated near-surface horizontal vorticity may be enhanced along the inflow side of the FFD, and this process is suggested to be stronger within nontornadic supercells given more enhanced regions of inferred HAE. Following tilting and stretching processes of horizontal vorticity common near and within supercell updraft/downdraft regions, a re-strengthening updraft (as inferred through trends of Z_{DR} column metrics) is likely to be observed, e.g., Snyder et al. (2015) found an increase in magnitude of characteristics of the Z_{DR} column initially precedes a strengthening of the updraft speed w. The observed consistency within the nontornadic sample inferred hail area metric comparisons is supportive of the proposed associations, suggesting that among nontornadic (and

tornadic) samples, polarimetrically inferred HAE metrics and max storm-core reflectivity value should be utilized together in conjunction with radar interrogation of Z_{DR} columns.

ii. Z_{DR} Arc Area, Mean Z_{DR} Arc Value, and Mean Z_{DR} Arc Width

This section will encompass the results of the Z_{DR} arc area, mean Z_{DR} arc value, and mean Z_{DR} arc width metric comparisons. Discussions will include a brief recap of the correlograms for each metric comparison along with further analysis into potential associations and similarities to known conceptual models and observations. The discussions have also been grouped into tornadic and nontornadic sections, as each sample tended to exhibit unique patterns and results.

a. Tornadic Sample Discussion

The Z_{DR} arc area metric comparison exhibited consistent results, with all three updraft proxy comparisons yielding a significant peak median correlation value greater than zero at negative lag times of 25 to 35 minutes, with the Z_{DR} column area comparison exhibiting the greatest magnitude correlation value (R~0.46). Based on the results from the raw Z_{DR} arc area metric comparisons, a direct positive relationship is noted, where an increase in the magnitude of any three Z_{DR} column metrics tended to precede an increase in the Z_{DR} arc area with a lead time of 25 to 35 minutes.

Comparatively, the results of the normalized Z_{DR} arc area metric comparisons exhibited an opposite result, with two of three metric comparisons (Z_{DR} column area and Z_{DR} column depth) producing a peak median correlation value less than zero at 45 minutes of positive lag. This is representative of an indirect relationship where an

increase in the magnitude of either the Z_{DR} column area or column depth tended to follow a decrease in the magnitude of the normalized Z_{DR} arc area by 45 minutes.

For the mean Z_{DR} arc value metric comparison, two of three updraft proxy comparisons (Z_{DR} column area and Z_{DR} column depth) yielded a significant peak median correlation value greater than zero (R~0.43 & 0.57, respectively) at 45 minutes of negative lag. The normalized Z_{DR} column area metric comparison was maximized at 45 minutes of positive lag (R~ –0.15) and not found to be significant, thus the prevailing trend was observed as an increase in the magnitude of either the Z_{DR} column area or Z_{DR} column depth tending to precede an increase in the mean Z_{DR} arc value by 45 minutes.

Lastly for the mean Z_{DR} arc width metric comparison, two of three updraft proxy comparisons (Z_{DR} column area and Z_{DR} column depth) exhibited a significant peak median correlation value greater than zero at 35 and 45 minutes of positive lag, respectively, where the Z_{DR} column area metric comparison produced the greatest magnitude correlation value (R~0.65). The normalized Z_{DR} column area metric comparison produced a result opposite of the other two updraft proxy comparisons, with a negative peak median correlation value at 45 minutes of negative lag. The majority observed pattern suggests a positive direct relationship, where an increase in the magnitude of the Z_{DR} column area or Z_{DR} column depth tended to follow an increase in the mean Z_{DR} arc width by 35 – 45 minutes.

The observations within this sample are consistent with prior work and suggest polarimetric signature associations that may be unique to pretornadic or tornadic supercells, however it should be noted that time of tornadogenesis and tornado dissipation were not available for use in this study. Palmer et al. (2011) and Crowe et al.

(2012) observed disruptions in the Z_{DR} arc within the low-level updraft region due to the ingestion of smaller raindrops (inferred through polarimetric radar observations). The presence of smaller raindrops near supercell low-level updraft regions is also noted in Kumjian (2011) and French et al. (2015) via WSR-88D and rapid-scan polarimetric radar observations. As the disruption of the arc region progressed, the arc tended to contract in length, parallel to the inflow side of the FFD gradient, and surge forward along the FFD gradient, often becoming larger than before the disruption. This process yielded the occlusion of the low-level mesocyclone, and the demise of ongoing tornadoes. A few examples among tornadic storms also observed a rapid enhancement in the magnitude of Z_{DR} values within the arc region as early as five minutes after the initial disruption of the Z_{DR} arc. Prior studies have only incorporated a select number of cases, and a minor discrepancy between their observations and those presented in this study can be expected, however the results presented are still in reasonable agreement with the conceptual timeframe.

In sequential order, an increase in the magnitude of the mean Z_{DR} arc width tended to precede an increase in magnitude of either the Z_{DR} column depth or area by 35 to 45 minutes, suggesting an increase in the magnitude of low-level storm-relative inflow and size sorting processes. Then, after an increase in magnitude of any of the Z_{DR} column metrics, an increase in magnitude of the Z_{DR} arc area tended to follow 25 to 35 minutes later, and is suggested to be indicative of the observed disruption of the arc area, which often precedes low-level mesocyclone occlusion. Lastly, an increase in magnitude of the mean Z_{DR} arc value tended to occur as little as 10 to 20 minutes after the initial arc disruption, or 45 minutes after an increase in magnitude of either the Z_{DR} column depth or

area. It is worth noting that secondary peaks in median correlation values which were greater than zero were observed at 35 to 45 minutes of negative lag for the mean Z_{DR} arc width metric comparisons when compared against Z_{DR} column area and column depth, respectively. This coincides with the occurrence of increasing magnitude of mean Z_{DR} arc value, and is likely representative of both the contracting nature of the arc following its disruption, and increasing low-level storm-relative inflow preceding the development of a new low-level mesocyclone, typical in cyclic tornadic supercells. The results presented are reasonably consistent with prior observations, and align with the conceptual timeframe.

It is suggested that environmental factors including an increase in magnitude of low-level storm-relative inflow and storm-relative helicity (SRH) may contribute to the variability of both the Z_{DR} arc and Z_{DR} column, and how they change in relation to the variability of each other. This pattern is most prominent within the timeframe of an ongoing tornado, where increases in these factors tends to increase size sorting processes, resulting in a wider arc and a strengthening updraft as inferred through Z_{DR} column tendencies, and eventually the disruption of the arc and occlusion of the low-level mesocyclone, leading to the demise of an ongoing tornado.

Van Den Broeke (2017) examined Z_{DR} arc behavior across tornado life cycles and found Z_{DR} arcs tended to grow larger and wider from tornadogenesis through tornado dissipation. Near-storm environmental factors such as low-level storm-relative inflow have been theorized to be stronger during tornadic times than in the absence of a tornado, contributing to stronger size sorting and a larger and more intense Z_{DR} arc (e.g., Palmer et al. 2011; Crowe et al. 2012; Van Den Broeke 2017). Additionally, the magnitude of

effective storm-relative helicity (ESRH; Thompson et al. 2007), in the storm environment is suggested to contribute to the evolution of the Z_{DR} column in relation to the Z_{DR} arc. Kumjian and Ryzhkov (2009) observed a positive correlation between SRH and the mean Z_{DR} arc value within an arc signature, and inherently, the magnitude of hydrometeor size sorting. Davies-Jones (1984) defines the environmental SRH as a measure of the streamwise component of vorticity within the environmental flow within the reference frame of a storm, and is quantified by Davies-Jones et al. (1990):

$$SRH = \int_0^h (\boldsymbol{V} - \boldsymbol{C}) \cdot \boldsymbol{\omega}\, dz \tag{4.1}$$

Quantitatively, SRH is defined as an integral from the surface to a defined vertical height (h), often the top of a calculated storm inflow layer, or an effective inflow layer (Thompson et al. 2007). The integrand consists of the storm relative wind defined as the storm motion vector (**C**) subtracted from the mean environmental wind vector (**V**), and the horizontal vorticity vector (**ω**).

The magnitude of ESRH may still play a role in low-level polarimetric signature evolution, however Dawson et al. (2015) demonstrated a more fundamental hydrometeor size sorting relationship. In the case of off-hodograph storm motions (e.g., supercell storm modes), these processes were found to occur solely in the presence of a non-zero mean storm-relative wind vector, and in the absence of any SRH. VDB16 also observed a moderately strong correlation between the 0-2 km storm-relative wind magnitude and the mean Z_{DR} arc width (R~0.42). A strong correlation was also shown between the maximum vertical extent of the 1-dB Z_{DR} column (terminology used within VDB16, but is interpreted as Z_{DR} column depth in the context of this study) and ESRH (R~0.67),

suggesting ESRH may be a more useful environmental proxy for updraft related polarimetric signatures.

In the case of near-storm environments for tornadic supercells, the low-level storm-relative wind is understood to veer vertically with more magnitude and is generally more streamwise relative to the low-level horizontal vorticity vector (e.g., Parker 2014; Coffer et al. 2017; Wade et al. 2018) yielding a greater magnitude of SRH. Greater amounts of streamwise vorticity (and inherently SRH) can yield stronger and more resilient updrafts as storm-scale perturbation pressure forces ensue. It is also important to consider storm-induced modifications of the near-storm environment around maturing supercells which are often subtle, but still significant (Parker 2014). Thus, for the tornadic sample utilized during this study, stronger low-level vertical wind shear was likely present, elongating the low-level hodograph and increasing the magnitudes of the ESRH and the mean low-level storm-relative wind.

b. Nontornadic Sample Discussion

The nontornadic sample of metric comparisons involving Z_{DR} arc-based metrics exhibited poor consistency across the three updraft proxies. However, the comparisons involving the Z_{DR} column area were shown to be consistent temporally with each other, and may be indicative of a prominent pattern involving the change in magnitude of Z_{DR} column area relative to characteristics of the Z_{DR} arc.

Among the Z_{DR} arc area metric comparisons, similar patterns were noted within two of the three individual updraft proxy metric comparisons (Z_{DR} column area and Z_{DR} column depth) for both Z_{DR} arc area, and normalized Z_{DR} arc area. This trend was

strongest in the Z_{DR} column area metric comparison, where significant peak median correlation values of R~0.85 & 0.86 were observed at 35 minutes of positive lag (Z_{DR} arc area and normalized Z_{DR} arc area, respectively). A strong direct relationship is inferred to exist between the Z_{DR} column area and the Z_{DR} arc area (raw and normalized), where an increase in the magnitude of the Z_{DR} column area tended to follow an increase in the magnitude of the Z_{DR} arc area by 35 minutes. For the Z_{DR} column depth metric comparisons, significant peak median correlation values of R~0.54 & 0.33 were observed at 40 minutes of negative lag for both the Z_{DR} arc area and normalized arc area comparisons, respectively. This is indicative of a direct relationship between the Z_{DR} column depth and arc area attributes, where an increase in the Z_{DR} column depth tended to precede increases in the Z_{DR} arc area and normalized arc area by 40 minutes.

For the mean Z_{DR} arc value metric comparisons, two of three updraft proxy comparisons (Z_{DR} column area and Z_{DR} column depth) yielded significant peak median correlation values greater than zero at 30 to 35 minutes of positive lag, respectively. The Z_{DR} column area metric comparison exhibited the greatest magnitude peak median correlation value (R~0.65). Comparatively, the normalized Z_{DR} column area metric comparison exhibited a significant and negative peak correlation value (R~ –0.30) at 15 minutes of negative lag. However, the majority trend suggests an increase in the magnitude of the Z_{DR} column area or Z_{DR} column depth tended to follow an increase in the mean Z_{DR} arc value by 30 to 35 minutes.

Among the mean Z_{DR} arc width metric comparisons, a wider array of results was shown, with two of three updraft proxy comparisons (Z_{DR} column area and Z_{DR} column depth) yielding significant positive peak correlation values of R~0.65 & 0.53,

respectively. However, these results were observed at 30 minutes of positive lag and 40 minutes of negative lag, respectively. Whereas the normalized Z_{DR} column area comparison exhibited a significant negative correlation value at 45 minutes of positive lag. Among the three updraft proxies used in this metric comparison, no clear pattern is evident, however based on the magnitude of observed correlation values, the strongest relationship exists with the Z_{DR} column area comparison (R~0.65, $p < 0.05$ at 30 minutes of positive lag), where an increase in the magnitude of the Z_{DR} column area tended to follow an increase in the mean arc width by 30 minutes. This is also consistent with the results of the prior Z_{DR} arc metric comparisons utilizing the Z_{DR} column area.

A strong relationship is suggested to exist between the characteristics of the Z_{DR} arc relative to changes in the Z_{DR} column area, within the nontornadic sample. Overall, an increase in magnitude of the Z_{DR} column area was shown to follow an increase in any of the Z_{DR} arc-based metrics by 30 to 35 minutes. Given the consistent nature of the metric comparisons in the nontornadic sample, near-storm environmental characteristics including the magnitude of the low-level storm-relative wind are suggested to play a role in enhancing the low-level Z_{DR} arc features for similar reasons as described in the tornadic sample, e.g., increasing low-level wind shear enhancing size sorting processes (Dawson et al. 2015), skewing drop-size distributions towards larger number concentrations of larger droplets, and further enhancing the magnitudes of the low-level Z_{DR} arc metrics. Additionally, microphysical differences owing to greater extent of polarimetrically inferred hail area and greater droplet shedding may further enhance Z_{DR} arc metrics, and the skewing of the drop-size distributions within the Z_{DR} arc could also enhance the generation of baroclinic horizontal vorticity along the FFD gradient. In turn,

an increase of streamwise vorticity into the low-level updraft may be observed after a lag time of 30 to 35 minutes via the increase in the magnitude of the Z_{DR} column metrics (particularly Z_{DR} column area for the nontornadic sample).

A distinction was observed between the tornadic and nontornadic samples for the association of the Z_{DR} column and characteristics of the Z_{DR} arc comparison, e.g., positively correlated and negatively lagged (tornadic sample), positively correlated and positively lagged (nontornadic sample). The difference may be attributable to microphysical differences in addition to the proposed dynamical processes. Supercells are well known to be responsible for extreme rainfall events (e.g., Moller et al. 1994; Smith et al. 2001; Hitchens and Brooks 2013; Schumacher 2015; Nielsen and Schumacher 2018, 2020), and a subset of supercells, known as high precipitation (HP) supercells (e.g., Moller et al. 1994), are known to produce more precipitation than other supercells (e.g., Smith et al. 2001; Beatty et al. 2008). HP supercells are still capable of producing tornadoes, but their microphysical characteristics such as larger number concentrations of hydrometeors near the updraft-downdraft interface intrinsic to supercells, are more likely to hinder tornadogenesis. This is generally due to cooler and more negatively buoyant air parcels in the RFD, relative to observations in tornadic storms (e.g. Markowski 2002; Markowski et al. 2002).

It is noted that the samples in this study were not classified by precipitation intensity (e.g., high precipitation and low precipitation). However, the results presented from the tornadic and nontornadic typical radar metric values are supportive of the inference that the nontornadic sample likely exhibited HP supercell characteristics more frequently, e.g., larger number concentrations of hydrometeors within and near the low-

level updraft region. Supercells which exhibit larger regions of inferred HAE, shown to be nontornadic supercells on average within this study, are suggested to generate a greater amount of droplet shedding from melting hail. Dawson et al. (2014) found that droplet shedding from melting hail plays a dominant role on Z_{DR} within the arc region, even with the absence of size sorting from rain drops. Thus, it is suggested that greater droplet shedding from a larger areal extent of melting hail contributes to a drop-size distribution skewed towards larger drop diameters, as well as the enhanced mean Z_{DR} arc values observed within the nontornadic sample.

Chapter 5: Conclusions

A dataset of metrics derived from polarimetric radar signatures in tornadic and nontornadic supercells observed by the WSR-88D network between 2012 and 2014 been analyzed and associations between polarimetric signatures have been hypothesized or further supported based on prior work. First, similarity tests, including KS and MWU tests were applied to test for significant differences in the distributions of all available tornadic and nontornadic sample scans for each radar metric. Statistical differences were observed in both tests applied for all the metrics outlined previously, excluding the 35-dBZ storm area, and the mean Z_{DR} arc width. Despite the overwhelming positive outcome, the operational practicality of the results is questionable upon review of the sample scan distributions. However, the inferred HAE, normalized inferred HAE, and all three Z_{DR} column sample scan distributions were shown to provide consistent and unique differences indicative of future operational value. Generally, among the tornadic sample scan distributions, both types of the inferred HAE metric were smaller and less variable, and the Z_{DR} column metrics were skewed towards larger magnitude values, consistent with findings shown in VDB20, which involved analysis of tornadic supercells during their pretornadic times.

To further test sample differences in metric values, a comparison method following Kuster et al. (2019) was introduced. T-NT metric differences were calculated for both observed sample metric statistics and non-parametric sample distributions created from a bootstrapping method, and the T-NT difference in sample distribution median values were compared against each other. Additionally, KS and MWU tests were applied to tornadic and nontornadic distributions of observed sample statistics, where a

sample statistic was calculated over a storm observation period, and included into that statistic distribution (e.g., a distribution of tornadic storm-median values for a given metric). A T-NT metric difference was determined to be significant if the observed difference value was greater in magnitude than the corresponding bootstrapping analysis difference, following Kuster et al. (2019), or if the results from either a KS or MWU test yielded a *p*-value less than 0.05, indicating the two sample distributions differed significantly at the 95% confidence level.

The results of this comparison method demonstrated consistent findings for median and mean metric value differences, while the maximum metric value differences yielded significance for the remaining metrics ousted from the median and mean results. Within the median and mean metric value difference comparisons, significance was shown for inferred HAE, normalized inferred HAE, max storm-core reflectivity value, mean Z_{DR} arc value, Z_{DR} column area, and normalized Z_{DR} column area. Like the first testing method, inferred HAE and Z_{DR} column metrics exhibited similar trends, e.g., smaller regions of inferred HAE and larger or broader Z_{DR} columns within the tornadic sample. The mean Z_{DR} arc value was also shown to be weaker in magnitude within the tornadic sample. The maximum metric value differences included significance for the Z_{DR} arc area, mean Z_{DR} arc width, normalized Z_{DR} column area, and Z_{DR} column depth, where the magnitudes of Z_{DR} arc area, normalized Z_{DR} column area, and Z_{DR} column depth were shown to be larger in magnitude within the tornadic sample, further supporting the notion of deeper and broader Z_{DR} columns within tornadic storms (VDB20). The mean Z_{DR} arc width produced differing results (a smaller arc width within the observed sample, and a larger arc width from the bootstrapped sample), however

from the median value differences, a smaller mean Z_{DR} arc width may be inferred for the tornadic sample. The consistency noted between the two comparison methods does further the arguments and trends noted among the tornadic and nontornadic samples of radar metrics, however future work may opt for new analytical methods and the inclusion of more storm cases for a greater diversity of supercell microphysical characteristics and near-storm environments.

Based on the sample distributions of typical metric values and the results of the comparison methods, microphysical and environmental characteristics between the two samples may also be inferred. For the nontornadic sample, low-level regions of inferred HAE were greater in magnitude, suggesting a greater hail mass, and likely more droplet shedding from melting hail. This factor may have also contributed to the larger storm core reflectivity and mean Z_{DR} arc values in the nontornadic sample as well. Within the tornadic sample, broader and deeper updrafts were inferred via Z_{DR} column depths and cross-sectional areas greater in magnitude than the nontornadic sample. Additionally, larger magnitude values of Z_{DR} arc area and mean Z_{DR} arc width shown within the tornadic sample may be indicative of stronger environmental size sorting via stronger low-level wind shear distributing larger raindrops farther into the storm FFD (poleward from the inflow side in right moving supercells).

Finally, cross-correlation coefficient values were calculated for numerous radar metric comparisons, with the Z_{DR} column cross-sectional area, normalized Z_{DR} column cross-sectional area, and Z_{DR} column depth metrics serving as an updraft proxy, or the independent variable. Two types of correlation testing were conducted, including storm-based and total sample correlation testing. Due to the small sample of individual storms

that had enough sample scans available for the duration of lag introduced, which was 45 minutes of positive and negative lag, the results of the storm-based correlation testing were included for completeness, however meaningful conclusions are likely not obtainable from the results. Future work may consider moving forward with an individual storm analysis method as testing each storm case individually is likely to reduce any biases that may be introduced from combining all available data into collective samples. Correlation testing which included comparing distributions of all available sample scans provided more meaningful sample sizes to compare. Additionally, a bootstrapping method (i = 5000) was introduced to the total sample correlation testing to generate median correlation values for comparison against the observed values.

The results presented from correlation testing support the original hypotheses and indicate potential associations between polarimetric supercell signatures which have also speculated to be associated with near-storm environmental parameters. This has been shown through moderately strong cross-correlation coefficient values that are maximized with significance after as much as 25 to 45 minutes, or as little as 5 to 10 minutes of positive or negative lag, depending on the metric comparison for both the tornadic and nontornadic sample. From the results, conceptual and physical models can be theorized and/or further supported from prior work on the associations of supercell polarimetric signature metrics:

1) Within the tornadic sample, the polarimetric hail signature metric comparisons yielded results consistent with prior work (e.g., Picca et al. 2010; Kumjian et al. 2014; Kuster et al. 2019, 2020) and supercell conceptual models. Z_{DR} column area

and depth were shown to increase in magnitude 25 to 30 minutes prior to an increase in the max storm-core reflectivity value, and 40 to 45 minutes prior to an increase in the inferred HAE. This pattern is suggested to be representative of processes within cyclic tornadic supercells where mesocyclogenesis and occluding mesocyclones may be observed multiple times. As mesocyclones develop and dissipate, multiple periods of intensifying low-level updrafts and lofted hail and ice mass may be observed, often interpreted operationally through the size of –20˚C reflectivity cores, where Kuster et al. (2019) and (2020) observed Z_{DR} column area and/or depth increasing five to nine minutes prior to the development or increase in size of a –20˚C reflectivity core.

2) The results of metric comparisons from the tornadic sample involving Z_{DR} arc characteristics were indicative of polarimetric associations unique to pretornadic and tornadic supercells. Patterns evident in metric comparison correlograms were also shown to be consistent with that of prior work (e.g., Palmer et al. 2011; Kumjian 2011; Crowe et al. 2012), and have been suggested to be dependent on the magnitude of near-storm low-level wind shear (Dawson et al. 2015). Chronologically, a widening of the Z_{DR} arc tended to precede an increase in magnitude of the Z_{DR} column depth or area by 35 to 45 minutes, and is suggested to represent a few processes including: 1) An increase in magnitude of low-level wind shear in the near-storm environment allowing for updraft intensification via greater low-level streamwise vorticity and 2) Greater magnitude of size sorting processes within the Z_{DR} arc region. Next, following the increase in magnitude of

the Z_{DR} column metrics, the Z_{DR} arc area tended to increase 25 to 35 minutes later, and is suggested to be indicative of observed disruptions and contractions of the Z_{DR} arc region due to ingestion of smaller raindrops near the low-level updraft region. Lastly, an increase in magnitude of the mean Z_{DR} arc value, tended to occur 10 to 20 minutes after an increase in the Z_{DR} arc area (suggested to be the disruption of the Z_{DR} arc), or 35 to 45 minutes after an increase in magnitude of either the Z_{DR} column depth or area.

3) Among the nontornadic sample, the results of inferred hail metric comparisons are also suggested to be representative of cyclical supercell processes, however, opposite to those of the tornadic sample. Generally, inferred hail metrics were shown to decrease in magnitude 20 to 35 minutes prior to an increase in magnitude of the Z_{DR} column area or depth. This pattern is suggested to be indicative of descending reflectivity and/or hail cores contributing an initial suppression of updraft intensity and subsequent re-intensification due to an increase in baroclinically generated near-surface horizontal vorticity. This process is also suggested to be more prevalent and potentially stronger within the nontornadic sample given larger observed regions of inferred HAE. Reasonable consistency was noted amongst the inferred hail metric comparisons for both tornadic and nontornadic samples, and suggests that polarimetrically inferred HAE metrics and max storm-core reflectivity value should be utilized together in conjunction with radar interrogation of Z_{DR} columns.

4) Lastly, the results of metric comparisons from the nontornadic sample involving Z_{DR} arc characteristics exhibited a consistent pattern, however, also opposite to that of the tornadic sample. Generally, an increase in magnitude of the Z_{DR} column area was shown to follow an increase in magnitude of any of the Z_{DR} arc-based metrics by 30 to 35 minutes. Near-storm environmental characteristics such as the magnitude of low-level wind shear are suggested to play a role in enhancing the low-level Z_{DR} arc features and the Z_{DR} column for similar reasons as described in the tornadic sample. Additionally, microphysical differences are suggested to exist owing to greater extents of polarimetrically inferred HAE within the nontornadic sample and subsequent greater droplet shedding contributing to enhancing Z_{DR} arc metrics (Dawson et al. 2014) via the skewing of drop-size distributions towards larger number concentrations of larger hydrometeors within the Z_{DR} arc.

Future work is needed to further test and verify these associations and may benefit from several additions. Kuster et al. (2019) and (2020) demonstrated that the evolution of polarimetric signatures such as the Z_{DR} column are better resolved at faster volume scan rates (~ 2 minutes), and can be used to accurately forecast the severity of ongoing convective storms. An evaluation of the metric comparisons outlined for this study with rapid-scan radar data may better conclude the hypotheses presented with better resolution of rapidly evolving polarimetric signatures.

Future studies may also consider recalculating the metrics via an objective analysis, such as the algorithm introduced by Wilson and Van Den Broeke (2021), for

comparison against the subjectively obtained metric values, as well as the inclusion of more storm cases, since the current dataset does not extend past 2014. Lastly, a more thorough thermodynamic and kinematic analysis of near-storm environments for cases which exhibit clear and consistent time-correlation patterns may increase confidence in regarding associations of radar metrics and the near-storm environment. The results presented pose an advantage over prior single-storm observational studies due to the diversity of storm sample geography. A greater geographic diversity of samples can prove useful in an operational warning decision situation (based on a better understanding of physical relationships between polarimetric signatures) as it does not limit the application of radar metric associations to one specific region, e.g., the Great Plains.

References

Austin, P. M., 1987: Relation between measured radar reflectivity and surface rainfall. *Mon. Wea. Rev.*, **115**, 1053-1070, https://doi.org/10.1175/1520-0493(1987)115%3C1053:RBMRRA%3E2.0.CO;2.

Balakrishnan, N., and D. S. Zrnić, 1990: Estimation of rain and hail rates in mixed-phase precipitation. *J. Atmos. Sci*., **47**, 565–583, https://doi.org/10.1175/1520-0469(1990)047%3C0565:EORAHR%3E2.0.CO;2.

Beatty, K., E. Rasmussen, and J. Straka, 2008: The supercell spectrum. Part I: A review of research related to supercell precipitation morphology. *Electron. J. Severe Storms Meteor*., **3 (4)**, http://www.ejssm.org/ojs/index.php/ejssm/article/viewArticle/44.

Bluestein, H. B., M. M. French, R. L. Tanamachi, S. Frasier, K. Hardwick, F. Junyent, and A. L. Pazmany, 2007: Close-Range Observations of Tornadoes in Supercells Made with a Dual-Polarization, X-Band, Mobile Doppler Radar. *Mon. Wea. Rev.*, **135**, 1522–1543, https://doi.org/10.1175/MWR3349.1.

Brandes, E. A., J. Vivekanandan, J. D. Tuttle, and C. J. Kessinger, 1995: A study of thunderstorm microphysics with multiparameter radar and aircraft observations. *Mon. Wea. Rev.*, **123**, 3129–3143, https://doi.org/10.1175/1520-0493(1995)123%3C3129:ASOTMW%3E2.0.CO;2.

Bringi, V. N., D. A. Burrows, and S. M. Menon, 1991: Multiparameter radar and aircraft study of raindrop spectral evolution in warm-based clouds. *J. Appl. Meteor*., **30**, 853–880, https://doi.org/10.1175/1520-0450(1991)030%3C0853:MRAASO%3E2.0.CO;2.

Bringi, V. N., L. Liu, P. C. Kennedy, V. Chandrasekar, and S. A. Rutledge, 1996: Dual multiparameter radar observations of intense convective storms: The 24 June 1992 case study. *Meteor. Atmos. Phys.*, **59**, 3–31, https://doi.org/10.1007/BF01031999.

Bringi, V. N., K. Knupp, A. Detwiler, L. Liu, I. J. Caylor, and R. A. Black, 1997: Evolution of a Florida thunderstorm during the Convection and Precipitation/Electrification Experiment: The case of 9 August 1991. *Mon. Wea. Rev.*, **125**, 2131–2160, https://doi.org/10.1175/1520-0493(1997)125%3C2131:EOAFTD%3E2.0.CO;2.

Brooks, H. E., C. A. Doswell III, and M. P. Kay, 2003: Climatological estimates of local daily tornado probability for the United States. *Wea. Forecasting*, **18**, 626–640, https://doi.org/10.1175/1520-0434(2003)018%3C0626:CEOLDT%3E2.0.CO;2.

Burke, P., D. Brown, D. Roth, and V. Vincente, 2017: WPC Rainfall Guidance for Tropical Cyclones. MetEd, COMET Program, UCAR, https://www.meted.ucar.edu/tropical/rainfall_guidance/index.htm.

Browning, K. A., 1965: Some inferences about the updraft within a severe local storm. *J. Atmos. Sci.*, **22**, 669–678, https://doi.org/10.1175/1520-0469(1965)022%3C0669:SIATUW%3E2.0.CO;2.

Chrisman, J. N., 2009: Automated Volume Scan Evaluation and Termination (AVSET)—A simple technique to achieve faster volume scan updates. Preprints, *34th Conf. on Radar Meteorology*, Williamsburg, VA, Amer. Meteor. Soc., P4.4. [Available online at https://ams.confex.com/ams/pdfpapers/155324.pdf].

Chrisman, J. N., 2013: Dynamic Scanning. *Radar Operations Center NEXRAD Now*, **22**, 1-3. [Available online at http://www.roc.noaa.gov/WSR88D/PublicDocs/NNOW/NNow22c.pdf].

Chrisman, J. N., 2014: Multiple Elevation Scan Option for SAILS (MESO-SAILS): The Next Step in Dynamic Scanning for the WSR-88D. National Oceanic and Atmospheric Administration. [Available online at https://www.roc.noaa.gov/WSR88D/PublicDocs/NewTechnology/MESO-SAILS_Description_Briefing_Jan_2014.pdf].

Chrisman, J. N., 2016: Mid-volume Rescan of Low-level Elevations (MRLE): A New Approach to Enhance Sampling of Quasi-Linear Convective Systems (QLCSs). National Oceanic and Atmospheric Administration. [Available online at https://www.roc.noaa.gov/WSR88D/PublicDocs/NewTechnology/DQ_QLCS_MRLE_June_2016.pdf].

Coffer, B. E., and M. D. Parker, 2016: Simulated supercells in nontornadic and tornadic VORTEX2 environments. *Mon. Wea. Rev*., **145**, 149–180, https://doi.org/10.1175/MWR-D-16-0226.1.

Coffer, B. E., M. D. Parker, J. M. L. Dahl, L. J. Wicker, and A. J. Clark, 2017: Volatility of tornadogenesis: An ensemble of simulated nontornadic and tornadic supercells in VORTEX2 environments. *Mon. Wea. Rev*., **145**, 4605–2625, https://doi.org/10.1175/MWR-D-17-0152.1.

Coffer, B. E., and M. D. Parker, 2018: Is There a “Tipping Point” between Simulated Nontornadic and Tornadic Supercells in VORTEX2 Environments? *Mon. Wea. Rev*., **146**, 2667–2693, https://doi.org/10.1175/MWR-D-18- 0050.s1.

Conway, J. W., and D. S. Zrnić, 1993: A study of embryo production and hail growth using dual-Doppler and multiparameter radars. *Mon. Wea. Rev.,* **121,** 2511–2528, https://doi.org/10.1175/1520-0493(1993)121%3C2511:ASOEPA%3E2.0.CO;2.

Crowe, C. C., C. J. Schultz, M. Kumjian, L. D. Carey, and W. A. Petersen, 2012: Use of dual-polarization signatures in diagnosing tornadic potential. *Electron. J. Oper. Meteor.*, **13**, 57–78.

Cotton, W. R., and R. A. Anthes, 1989: *Storm and Cloud Dynamics*. Academic Press, 883 pp.

Davies-Jones, R., 1984: Streamwise vorticity: The origin of updraft rotation in supercell storms. *J. Atmos. Sci.,* **41,** 2991–3006, https://doi.org/10.1175/1520-0469(1984)041%3C2991:SVTOOU%3E2.0.CO;2.

Davies-Jones, R., D. W. Burgess, and M. Foster, 1990: Test of helicity as a forecast parameter. Preprints, *16th Conf. on Severe Local Storms*, Kananaskis Park, AB, Canada, Amer. Meteor. Soc., 588–592.

Dawson, D. T., E. R. Mansell, Y. Jung, L. J. Wicker, M. R. Kumjian, and M. Xue, 2014: Low-level Z_{DR} signatures in supercell forward flanks: The role of size sorting and melting of hail. *J. Atmos. Sci.*, **71**, 276–299, https://doi.org/10.1175/JAS-D-13-0118.1.

Dawson, D. T., Mansell, E. R., and Kumjian, M. R., 2015: Does wind shear cause hydrometeor size sorting? *J. Atmos. Sci.*, **72**, 340-348, https://doi.org/10.1175/JAS-D-14-0084.1.

Doswell, C. A., 1994: Flash-flood-producing convective storms: Current understanding and research. *Proc. U.S.–Spain Workshop on Natural Hazards,* Barcelona, Spain, National Science Foundation, 97–107.

Doswell, C. A., 2001: Severe convective storms—An overview. *Severe Convective Storms, Meteor. Mongr.*, No. 50, Amer. Meteor. Soc., 1–26.

Doviak, R. J., and D. S. Zrnić, 1993: *Doppler Radar and Weather Observations*. Dover Publications, 562 pp.

French, M. M., D. W. Burgess, E. R. Mansell, and L. J. Wicker, 2015: Bulk Hook Echo Raindrop Sizes Retrieved Using Mobile, Polarimetric Doppler Radar Observations. *J. Appl. Meteor. Climatol.*, **54**, 423–450, https://doi.org/10.1175/JAMC-D-14-0171.1.

Ganson, S. M., and M. R. Kumjian, 2015: Quantifying the relationship between the Z_{DR} arc signature and low-level vertical wind shear. *37th Conf. on Radar Meteorology,* Norman, OK, Amer. Meteor. Soc., 13B.6. [Available online at https://ams.confex.com/ams/37RADAR/webprogram/Paper275479.html.]

Griffin, C. B., C. C. Weiss, A. E. Reinhart, J. C. Snyder, H. B. Bluestein, J. Wurman, and K. A. Kosiba, 2018: In Situ and Radar Observations of the Low Reflectivity Ribbon in Supercells during VORTEX2. *Mon. Wea. Rev.*, **146**, 307–327, https://doi.org/10.1175/MWR-D-17-0201.1.

Goodman, L. A., 1954: Kolmogorov-smirnov tests for psychological research. *Psychological Bulletin*, **51**, 160–168, https://doi.org/10.1037/h0060275.

Hall, M. P. M., J. W. F. Goddard, and S. M. Cherry, 1984: Identification of hydrometeors and other targets by dual-polarization radar. *Radio Sci.*, **19**, 132–140, https://doi.org/10.1029/RS019i001p00132.

Herzegh, P. H., and A. R. Jameson, 1992: Observing precipitation through dual-polarization radar measurements. *Bull. Amer. Meteor. Soc.*, **73**, 1365–1374, https://doi.org/10.1175/1520-0477(1992)073%3C1365:OPTDPR%3E2.0.CO;2.

Hitchens, N. M., and H. E. Brooks, 2013: Preliminary investigation of the contribution of supercell thunderstorms to the climatology of heavy and extreme precipitation in the United States. *Atmos. Res.*, **123**, 206–210, https://doi.org/10.1016/j.atmosres.2012.06.023.

Homeyer, C. R., and M. R. Kumjian, 2015: Microphysical characteristics of overshooting convection from polarimetric radar observations. *J. Atmos. Sci.*, **72**, 870–891, https://doi.org/10.1175/JAS-D-13-0388.1.

Hubbert, J., V. N. Bringi, L. D. Carey, and S. Bolen, 1998: CSU-CHILL polarimetric measurements from a severe hailstorm in eastern Colorado. *J. Appl. Meteor.*, **37,** 749–755, https://doi.org/10.1175/1520-0450(1998)037%3C0749:CCPRMF%3E2.0.CO;2.

Illingworth, A. J., J. W. F. Goddard, and S. M. Cherry, 1987: Polarization radar studies of precipitation development in convective storms. *Quart. J. Roy. Meteor. Soc.*, **113**, 469–489, https://doi.org/10.1002/qj.49711347604.

Johnson, D. E., P. K. Wang, and J. M. Straka, 1993: Numerical simulation of the 2 August 1981 CCOPE supercell storm with and without ice microphysics. *J. Appl. Meteor.*, **32**, 745–759, https://doi.org/10.1175/1520-0450(1993)032%3C0745:NSOTAC%3E2.0.CO;2.

Jung, Y., M. Xue, and G. Zhang, 2010: Simulations of polarimetric radar signatures of a supercell storm using a two-moment bulk microphysics scheme. *J. Appl. Meteor. Climatol.*, **49**, 146–163, https://doi.org/10.1175/2009JAMC2178.1.

Khain, A., and B. Lynn, 2009: Simulation of a supercell storm in clean and dirty atmosphere using weather research and forecast model with spectral bin microphysics. *J. Geophys. Res*., **114**, D19209. http://dx.doi.org/10.1029/2009JD011827.

Klemp, J. B., and R. B. Wilhelmson, 1978: Simulations of right- and left-moving storms produced through storm splitting. *J. Atmos. Sci.,* **35,** 1097–1110, https://doi.org/10.1175/1520-0469(1978)035%3C1097:SORALM%3E2.0.CO;2.

Kumjian, M. R., 2013a: Principles and applications of dual-polarization weather radar. Part I: Description of the Polarimetric Radar Variables. *J. Operational Meteor*., **1** (20), 226–242, http://dx.doi.org/10.15191/nwajom.2013.0119.

Kumjian, M. R., 2013b: Principles and applications of dual-polarization weather radar. Part II: Warm- and cold-season applications. *J. Operational Meteor*., **1** (20), 243–264, http://dx.doi.org/10.15191/nwajom.2013.0120.

Kumjian, M. R., 2013c: Principles and applications of dual-polarization weather radar. Part III: Artifacts. *J. Operational Meteor*., **1** (21), 265–274.

Kumjian, M. R. and Ryzhkov, A. V., 2008: Polarimetric signatures in supercell thunderstorms. *J. Appl. Meteor. Climatol.*, **47**, 1940-1961. https://doi.org/10.1175/2007JAMC1874.1.

Kumjian, M. R. and Ryzhkov, A. V., 2009: Storm-relative helicity revealed from polarimetric radar measurements. *J. Atmos. Sci*., **66**, 667–685, https://doi.org/10.1175/2008JAS2815.1.

Kumjian, M. R., 2011: Precipitation properties of supercell hook echoes. *Electron. J. Severe Storms Meteor.*, **6** (5). [Available online at http://ejssm.org/ojs/index.php/ejssm/article/viewArticle/93.]

Kumjian, M. R. and A. V. Ryzhkov, 2012: The impact of size sorting on the polarimetric radar variables. *J. Atmos. Sci*., **69**, 2042– 2060, https://doi.org/10.1175/JAS-D-11-0125.1.

Kumjian, M. R., A. V. Ryzhkov, V. M. Melnikov, T. J. Schuur, 2010: Rapid-scan super-resolution observations of a cyclic supercell with a dual-polarization WSR-88D. *Mon. Wea. Rev.*, **138**, 3762–3786, https://doi.org/10.1175/2010MWR3322.1.

Kumjian, M. R., S. M. Ganson, and A. V. Ryzhkov, 2012: Freezing of raindrops in deep convective updrafts: A microphysical and polarimetric model. *J. Atmos. Sci.*, **69**, 3471–3490, https://doi.org/10.1175/JAS-D-12-067.1.

Kumjian, M. R., A. P. Khain, N. Benmoshe, E. Ilotoviz, A. V. Ryzhkov, and V. T. J. Phillips, 2014: The anatomy and physics of Z_{DR} columns: Investigating a polarimetric radar signature with a spectral bin microphysical model. *J. Appl. Meteor. Climatol.*, **53**, 1820–1843, https://doi.org/10.1175/JAMC-D-13-0354.1.

Kuster, C M., J. C. Snyder, T. J. Schuur, T. T. Lindley, P. L. Heinselman, J. C. Furtado, J. W. Brogden, and R. Toomey, 2019: Rapid-update radar observations of Z_{DR} column depth and its use in the warning decision process. *Wea. Forecasting*, **34**, 1173–1188, https://doi.org/10.1175/WAF-D-19-0024.1.

Kuster, C M., T. J. Schuur, T. T. Lindley, and J. C. Snyder, 2020: Using Z_{DR} columns in forecaster conceptual models and warning decision-making. *Wea. Forecasting*, **35**, 2507–2522, https://doi.org/10.1175/WAF-D-20-0083.1.

Lesins, G. B., and R. List, 1986: Sponginess and drop shedding of gyrating hailstones in a pressure-controlled icing wind tunnel. *J. Atmos. Sci.*, **43,** 2813–2825, https://doi.org/10.1175/1520-0469(1986)043%3C2813:SADSOG%3E2.0.CO;2.

Lim, K.-S. S., S.-Y. Hong, S. S. Yum, J. Dudhia, J. B. Klemp, 2011: Aerosol effects on the development of a supercell storm in a double-moment bulk-cloud microphysics scheme. *J. Geophys. Res.*, **116**, D02204, http://dx.doi.org/10.1029/2010JD014128.

Loney, M. L., D. S. Zrnić, J. M. Straka, and A. V. Ryzhkov, 2002: Enhanced polarimetric radar signatures above the melting level in a supercell storm. *J. Appl. Meteor.*, **41**, 1179–1194, https://doi.org/10.1175/1520-0450(2002)041%3C1179:EPRSAT%3E2.0.CO;2.

Markowski, P. M., 2002: Hook echoes and rear-flank downdrafts: A review. *Mon. Wea. Rev.*, **130,** 852–876, https://doi.org/10.1175/1520-0493(2002)130%3C0852:HEARFD%3E2.0.CO;2.

Markowski, P. M., J. M. Straka, and E. N. Rasmussen, 2002: Direct surface thermodynamic observations within the rear-flank downdrafts of nontornadic and

tornadic supercells. *Mon. Wea. Rev*., **130**, 1692–1721, https://doi.org/10.1175/1520-0493(2002)130%3C1692:DSTOWT%3E2.0.CO;2.

Meischner, P. F., V. N. Bringi, D. Heimann, and H. Höller, 1991: A squall line in southern Germany: Kinematics and precipitation formation as deduced by advanced polarimetric and Doppler radar measurements. *Mon. Wea. Rev.*, **119**, 678–701, https://doi.org/10.1175/1520-0493(1991)119%3C0678:ASLISG%3E2.0.CO;2.

Moller, A. R., C. A. Doswell III, M. P. Foster, and G. R. Woodall, 1994: The operational recognition of supercell thunderstorm environments and storm structures. *Wea. Forecasting*, **9**, 327–347, https://doi.org/10.1175/1520-0434(1994)009%3C0327:TOROST%3E2.0.CO;2.

Morrison, H., and J. Milbrandt, 2011: Comparison of two-moment bulk microphysics schemes in idealized supercell thunderstorm simulations. *Mon. Wea. Rev*., **139**, 1103–1130, https://doi.org/10.1175/MWR-D-15-0233.1.

National Hurricane Center, 2020: NHC Tropical Cyclone Graphical Product Descriptions. Accessed 30 June 2020, https://www.nhc.noaa.gov/aboutnhcgraphics.shtml.

Nielsen, E. R., and R. S. Schumacher, 2018: Dynamical insights into extreme short-term precipitation associated with supercells and mesovortices. *J. Atmos. Sci*., **75**, 2983–3009, https://doi.org/10.1175/JAS-D-17-0385.1.

Nielsen, E. R., and R. S. Schumacher, 2020: Observations of extreme short-term precipitation associated with supercells and mesovortices. *Mon. Wea. Rev.*, **148**, 159–182, https://doi.org/10.1175/MWR-D-19-0146.1.

Nelson, S. P., 1983: The influence of storm flow structure on hail growth. *J. Atmos. Sci*., **40**, 1965–1983, https://doi.org/10.1175/1520-0469(1983)040%3C1965:TIOSFS%3E2.0.CO;2.

Palmer, R. D., and Coauthors, 2011: Observations of the 10 May 2010 tornado outbreak using OU-PRIME: Potential for new science with high-resolution polarimetric radar. *Bull. Amer. Meteor. Soc*., **92**, 871–891, https://doi.org/10.1175/2011BAMS3125.1.

Parker, M. D., 2014: Composite VORTEX2 Supercell Environments from Near-Storm Soundings. *Mon. Wea. Rev.*, **142**, 508–529, https://doi.org/10.1175/MWR-D-13-00167.1.

Pazmany, A. L., J. B. Mead, H. B. Bluestein, J. C. Snyder, and J. B. Houser, 2013: A Mobile Rapid-Scanning X-band Polarimetric (RaXPol) Doppler Radar System. *J. Atmos. Oceanic Technol.*, **30**, 1398–1413, https://doi.org/10.1175/JTECH-D-12-00166.1.

Picca, J. C., M. R. Kumjian, and A. V. Ryzhkov, 2010: Z_{DR} columns as a predictive tool for hail growth and storm evolution. 25th Conf. on Severe Local Storms, Denver, CO, Amer. Meteor. Soc., 11.3. [Available online at https://ams.confex.com/ams/25SLS/techprogram/paper_175750.htm.]

Picca, J. C., and A. V. Ryzhkov, 2012: A dual-wavelength polarimetric analysis of the 16 May 2010 Oklahoma City extreme hailstorm. *Mon. Wea. Rev*., **140**, 1385–1403, https://doi.org/10.1175/MWR-D-11-00112.1.

Picca, J. C., J. C. Snyder, and A. V. Ryzhkov, 2015: An observational analysis of Z_{DR} column trends in tornadic supercells. *37th Conf. on Radar Meteorology*, Norman, OK, Amer. Meteor. Soc., 5A.5, [Available online at https://ams.confex.com/ams/37RADAR/webprogram/Paper275416.html.]

Raghavan, R., and V. Chandrasekar, 1994: Multiparameter radar study of rainfall: Potential application to area-time integral studies. *J. Appl. Meteor.*, **33**, 1636–1645, https://doi.org/10.1175/1520-0450(1994)033<1636:MRSORP>2.0.CO;2.

Rinehart, R. E., 2004: Radar for Meteorologists. Rinehart, 482 pp.

Romine, G. S., D. W. Burgess, and R. B. Wilhelmson, 2008: A dual-polarization-radar-based assessment of the 8 May 2003 Oklahoma City area tornadic supercell. *Mon. Wea. Rev.*, **136**, 2849–2870, https://doi.org/10.1175/2008MWR2330.1.

Rosner, B., and D. Grove, 1999: Use of the mann-whitney u-test for clustered data. *Statistics in medicine*, **18**, 1387–1400.

Rotunno, R., and J. Klemp, 1982: The influence of the shear induced pressure gradient on thunderstorm motion. *Mon. Wea. Rev.*, **110,** 136–151, https://doi.org/10.1175/1520-0493(1982)110%3C0136:TIOTSI%3E2.0.CO;2.

Rotunno, R., and J. Klemp, 1985: On the rotation and propagation of simulated supercell thunderstorms. *J. Atmos. Sci.*, **42,** 271–292, https://doi.org/10.1175/1520-0469(1985)042%3C0271:OTRAPO%3E2.0.CO;2.

Ryzhkov, A. V., V. B. Zhuravlyov, and N. A. Rybakova, 1994: Preliminary results of X-band polarization radar studies of clouds and precipitation. *J. Atmos. Oceanic Technol.*, **11**, 132–139, https://doi.org/10.1175/1520-0426(1994)011%3C0132:PROXBP%3E2.0.CO;2.

Ryzhkov, A. V., T. J. Schuur, D. W. Burgess, and D. S. Zrnić, 2005: Polarimetric tornado detection. *J. Appl. Meteor.*, **44**, 557–570, https://doi.org/10.1175/JAM2235.1.

Scharfenberg, K. A., and Coauthors, 2005: The Joint Polarization Experiment: Polarimetric radar in forecasting and warning decision making. *Wea. Forecasting*, **20**, 775–788, https://doi.org/10.1175/WAF881.1.

Schumacher, R. S., 2015: Resolution dependence of initiation and upscale growth of deep convection in convection-allowing forecasts of the 31 May–1 June 2013 supercell and MCS. *Mon. Wea. Rev.*, **143**, 4331–4354, https://doi.org/10.1175/MWR-D-15-0179.1.

Seliga, T. A., and V. N. Bringi, 1976: Potential use of radar differential reflectivity measurements at orthogonal polarizations for measuring precipitation. *J. Appl. Meteor.*, **15**, 69–76.

Shabbott, C. J., and P. M. Markowski, 2006: Surface in situ observations within the outflow of forward-flank downdrafts of supercell thunderstorms. *Mon. Wea. Rev.*, **134,** 1422–1441, https://doi.org/10.1175/MWR3131.1.

Shapiro, S. S., and M. B. Wilk, 1965: An analysis of variance test for normality (complete samples), *Biometrika*, **52**, 591–611.

Shupyatsky, A. B., L. A. Dinevitch, I. P. Kapitalchuk, and D. K. Shtivelman, 1990: Use of polarization measurements in Cb for the analysis of their stage of development. *Meteor. Hydrol.*, **12**, 57–66.

Skinner, P. S., Weiss, C. C., M. M. French, H. B. Bluestein, P. M. Markowski, and Y. P. Richardson, 2014: VORTEX2 observations of a low-level mesocyclone with multiple internal rear-flank downdraft momentum surges in the 18 May 2010

Dumas, Texas, supercell. *Mon. Wea. Rev.*, **142**, 2935–2960, https://doi.org/10.1175/MWR-D-13-00240.1.

Skinner, P. S., C. C. Weiss, J. L. Schroeder, L. J. Wicker, and M. I. Biggerstaff, 2011: Observations of the surface boundary structure within the 23 May 2007 Perryton, Texas, supercell. *Mon. Wea. Rev*., **139**, 3730–3749, https://doi.org/10.1175/MWR-D-10-05078.1.

Smith, J. A., M. L. Baeck, Y. Zhang, and C. A. Doswell III, 2001: Extreme rainfall and flooding from supercell thunderstorms. *J. Hydrometeor.*, **2,** 469–489, https://doi.org/10.1175/1525-7541(2001)002%3C0469:ERAFFS%3E2.0.CO;2.

Snyder, J. C., 2013: Observations and simulations of polarimetric weather radar signatures in supercells. Ph.D. dissertation, University of Oklahoma, 213 pp.

Snyder, J. C., H. B. Bluestein, V. Venkatesh, and S. J. Frasier, 2013: Observations of Polarimetric Signatures in Supercells by an X-Band Mobile Doppler Radar. *Mon. Wea. Rev.*, **141**, 3–29, https://doi.org/10.1175/MWR-D-12-00068.1.

Snyder, J. C., A. V. Ryzhkov, M. R. Kumjian, A. P. Khain, and J. Picca, 2015: A Z_{DR} column detection algorithm to examine convective storm updrafts. *Wea. Forecasting*, **30**, 1819–1844, https://doi.org/10.1175/WAF-D-15-0068.1.

Tanamachi, R. L., H. B. Bluestein, J. B. Houser, S. J. Frasier, and K. M. Hardwick, 2012: Mobile, X-band, Polarimetric Doppler Radar Observations of the 4 May 2007 Greensburg, Kansas, Tornadic Supercell. *Mon. Wea. Rev.*, **140**, 2103–2125, https://doi.org/10.1175/MWR-D-11-00142.1.

Thompson, R. L., R. Edwards, J. A. Hart, K. L. Elmore, and P. Markowski, 2003: Close proximity soundings within supercell environments obtained from the Rapid

Update Cycle. *Wea. Forecasting*, **18,** 1243–1261, https://doi.org/10.1175/1520-0434(2003)018%3C1243:CPSWSE%3E2.0.CO;2.

Thompson, R. L., C. M. Mead, and R. Edwards, 2007: Effective storm-relative helicity and bulk shear in supercell thunderstorm environments. *Wea. Forecasting*, **22**, 102–115, https://doi.org/10.1175/WAF969.1.

Tuttle, J. D., V. N. Bringi, H. D. Orville, and F. J. Kopp, 1989: Multiparameter radar study of a microburst: Comparison with model results. *J. Atmos. Sci*., **46**, 601–620, https://doi.org/10.1175/1520-0469(1989)046%3C0601:MRSOAM%3E2.0.CO;2.

Van Den Broeke, M. S., J. M. Straka, and E. N. Rasmussen, 2008: Polarimetric radar observations at low levels during tornado life cycles in a small sample of classic Southern Plains supercells. *J. Appl. Meteor. Climatol*., **47**, 1232–1247, https://doi.org/10.1175/2007JAMC1714.1.

Van Den Broeke, M. S., 2016: Polarimetric variability of classic supercell storms as a function of environment. *J. Appl. Meteor. Climatol*., **55**, 1907–1925, https://doi.org/10.1175/JAMC-D-15-0346.1.

Van Den Broeke, M. S., 2017: Polarimetric radar metrics related to tornado life cycles and intensity in supercell storms. *Mon. Wea. Rev.*, **145**, 3671–3686, https://doi.org/10.1175/MWR-D-16-0453.1.

Van Den Broeke, M. S., 2020: A preliminary polarimetric radar comparison of pretornadic and nontornadic supercell storms. *Mon. Wea. Rev.*, **148**, 1567–1584, https://doi.org/10.1175/MWR-D-19-0296.1.

Vivekanandan, J., J. Turk, G. L. Stephens, and V. N. Bringi, 1990: Microwave radiative transfer studies using combined multiparameter radar and radiometer measurements during COHMEX. *J. Appl. Meteor*., **29**, 561–585, https://doi.org/10.1175/1520-0450(1990)029%3C0561:MRTSUC%3E2.0.CO;2.

Wade, A. R., M. C. Coniglio, and C. L. Ziegler, 2018: Comparison of near- and far-field supercell inflow environments using radiosonde observations. *Mon. Wea. Rev.*, **146**, 2403–2415, https://doi.org/10.1175/MWR-D-17-0276.1.

Wakimoto, R. M., and V. N. Bringi, 1988: Dual-polarization observations of microbursts associated with intense convection: The 20 July storm during the MIST project. *Mon. Wea. Rev*., **116**, 1521–1539, https://doi.org/10.1175/1520-0493(1988)116%3C1521:DPOOMA%3E2.0.CO;2.

Wakimoto, R. M., N. T. Atkins, K. M. Butler, H. B. Bluestein, K. Thiem, J. Snyder, and J. Houser, 2015: Photogrammetric Analysis of the 2013 El Reno Tornado Combined with Mobile X-Band Polarimetric Radar Data. *Mon. Wea. Rev.*, **143**, 2657–2683, https://doi.org/10.1175/MWR-D-15-0034.1.

Wakimoto, R. M., Z. Wienhoff, H. B. Bluestein, and D. Reif, 2018: The Dodge City Tornadoes on 24 May 2016: Damage Survey, Photogrammetric Analysis Combined with Mobile Polarimetric Radar Data. *Mon. Wea. Rev.*, **146**, 3735–3771, https://doi.org/10.1175/MWR-D-18-0125.1.

Wilson, M. B., and M. S. Van Den Broeke, 2021: An automated python algorithm to quantify Z_{DR} arc and K_{DP} - Z_{DR} separation signatures in supercells. *J. Atmos. Oceanic Technol.*, **38**, 371-386, https://doi.org/10.1175/JTECH-D-20-0056.1.

Youngsun, J., Xue, M., Zhang, G., 2010: Simulations of Polarimetric Radar Signatures of a Supercell Storm Using a Two-Moment Bulk Microphysics Scheme. *J. Appl. Meteor. Climatol.*, **49**, 146-163, https://doi.org/10.1175/2009JAMC2178.1.